MODELS OF BORDER ZONE ARRHYTHMIAS IN ACUTE CARDIAC ISCHEMIA

by

Bradford E. Peercy

A dissertation submitted to the faculty of
The University of Utah
in partial fulfillment of the requirements for the degree of

Doctor of Philosophy

Department of Mathematics

The University of Utah

December 2003

THE UNIVERSITY OF UTAH GRADUATE SCHOOL

SUPERVISORY COMMITTEE APPROVAL

of a dissertation submitted by

Bradford E. Peercy

This dissertation has been read by each member of the following supervisory committee and by majority vote has been found to be satisfactory.

	Chair: James P. Keener
	Paul C. Bressloff
	Paul C. Fife
	Aaron L. Fogelson
	Kenneth W. Spitzer

THE UNIVERSITY OF UTAH GRADUATE SCHOOL

FINAL READING APPROVAL

To the Graduate Council of the University of Utah:

I have read the dissertation of Bradford E. Peercy in its final form and have found that (1) its format, citations, and bibliographic style are consistent and acceptable; (2) its illustrative materials including figures, tables, and charts are in place; and (3) the final manuscript is satisfactory to the Supervisory Committee and is ready for submission to The Graduate School.

Date

James P. Keener
Chair, Supervisory Committee

Approved for the Major Department

Graeme W. Milton
Chair/Dean

Approved for the Graduate Council

David S. Chapman
Dean of The Graduate School

ABSTRACT

Coronary artery occlusion leading to ischemic cardiac tissue is the first step in a cascade of events leading of cardiac fibrillation and death. Coupled cell and strip of tissue experiments have been designed to understand the electrotonic effects of ischemic tissue on normal tissue across the border zone.

We use coupled ordinary differential equations to model an ischemic (depolarized) cell coupled to a normal cell for various coupling strengths, masses of the regions, and degrees and ischemia. For three model ionics, reduced Hodgkin-Huxley, Modified McKean, and Luo-Rudy I, we use bifurcation theory to find the boundary between oscillatory and nonoscillatory solutions in parameter space. For certain regions in parameter space each set of ionics yields oscillations in the coupled cell model. There are degrees of ischemia for which the ischemic cell is stable and inexcitable when uncoupled, but when coupled to a normal, excitable cell with certain strengths and cell sizes the cells oscillate. For the size of a normal cell sufficiently smaller than an ischemic cell, we state a general principle that relates the oscillation of a single cell under forcing to oscillations of the coupled system.

We model a strip of tissue, part of which is subjected to an ischemic solution, as a one-dimensional partial differential equation with the Modified McKean nonlinearity. The coupling coefficient and degree of ischemia are possibly discontinuous in space. We prove existence and uniqueness of the steady state solution using a phase plane argument and super and subsolution techniques. We perform linear stability analysis and find a Sturm-Liouville eigenvalue problem whose eigenvalues yield conditions on stability of the steady state solution. These conditions lead to regions in parameter space for which the model admits oscillatory solutions. Several qualitative features of experiments are reproduced.

To Megan and Paige.

CONTENTS

LIST OF FIGURES

ACKNOWLEDGMENTS

I would like to thank Dr. Keener for his guidance prior to and throughout this project and my committee members for helpful discussions and comments on this dissertation.

I would like to thank my fellow graduate students in the mathematical biology program, in general, and specifically those past and present members of the Keener group. Thanks to my officemates Eric C., Nick, and Young-Seon for sharing this journey. Thanks to Tom and Bob for keeping things light. Thanks to Eric M. and Tim for the introduction into the group.

I would like to thank my parents for their love and support throughout my life, my wife, Megan, for her love and encouragement, and our baby girl, Paige, through whom true joy is just a smile away.

CHAPTER 1

INTRODUCTION

1.1 Acute Ischemia in Cardiac Tissue

Cardiac tissue is maintained through a complex network of coronary arteries distributed across the surface of the heart. Occlusion or blockage of a branch within this arterial network causes blood flow down stream to cease. The deprivation of blood flow to a region of tissue causes loss of nutrients, such as glucose, loss of oxygen and the accumulation of waste products. This combination of effects is termed ischemia. With the loss of homeostasis due to ischemia, a cascade of biochemical processes occurs in the ischemic myocardium. Many of these processes negatively affect the electrical conduction system, which the heart uses to organize rhythmic pumping.

The size of the region of myocardium subjected to ischemic insult depends upon how distal the occlusion is in the branching network of coronary arteries from the origin of the coronary artery network. If the occlusion occurs proximal to the origin of the coronary artery network, prior to significant branching, a large portion of heart muscle is affected upon occlusion. On the other hand, if the blockage is much farther down the arterial tree, say near the capillary level, possibly only a few cells are affected.

The central area of an ischemic region is the most affected. Tissue in the periphery of an ischemic region receives some level of collateral blood flow from the surrounding normally perfused myocardium. This periphery between highly ischemic and normal tissue where a gradient of ischemia exists was first identified by Harris and Rojas [10] as the "Border Zone." The portion of the border zone on the surface of the heart is the epicardial border zone, but the border zone

extends endocardially into ventricular tissue through the midmyocardium and even the endocardium.

It is well established [12] [2] [3] that an important biochemical effect of ischemia is the increase of extracellular potassium (K_0^+). K_0^+ rises in a triphasic manner [3] (see Figure 1.1 (a)) and leads to elevated (less depolarized) transmembrane potentials. Additionally, coupling between cells via gap junctions begins to decrease with the rise of intercellular proteins [1] (see Figure 1.1 (b)) such as lysophosphatidylcholine [5] and long chain acylcarnitine [35] as well as with the increase of both intercellular and extracellular pH [4].

While the ischemic region is coupled to the normal tissue with normal resting membrane potential, there is a difference in transmembrane potentials across gap junctions. This difference induces an "injury current" across the border between ischemic and nonischemic tissue. The injury current exists throughout the border zone where there is a gradient of injury. Since cardiac tissue, as an excitable medium, can be forced by external currents, an injury current may be sufficient to create ectopic foci originating at the border zone.

1.2 Experiments on Coupled Cells Involving Ischemia

High extracellular potassium and uncoupling of gap junctions in a given mass of tissue are important manifestations of acute cardiac ischemia. Tan and Joyner [31] developed a technique that coupled a single cardiac cell with variable resistance to a computer model cell. This design allowed the administration of chemicals to the cardiac cell and/or the mathematical adjustment of the model cell. Variable resistance between the cardiac cell and the model cell was interpreted as intercellular gap junction communication strength. The following describes experiments designed in the framework mentioned above to study the effects of individual and combined aspects of ischemia on coupled cells.

Tan and Joyner [32] coupled a real ventricular cell (VC) to a passive model cell with a depolarized resting membrane potential (RMP) (-20mV, -10mV, 0mV).

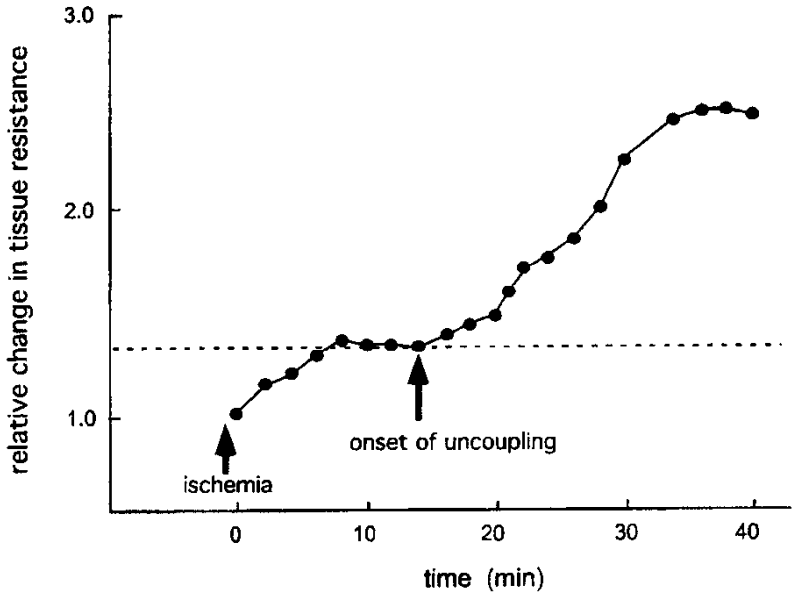

(a)

Figure 1.1: Time courses from experiments describing aspects of ischemia. (a) A time course of the relative change in tissue resistance in ischemic myocardium from Beardslee et al. [1]. (b) A time course of K_0^+ and pH in ischemic myocardium from Casio et al. [3].

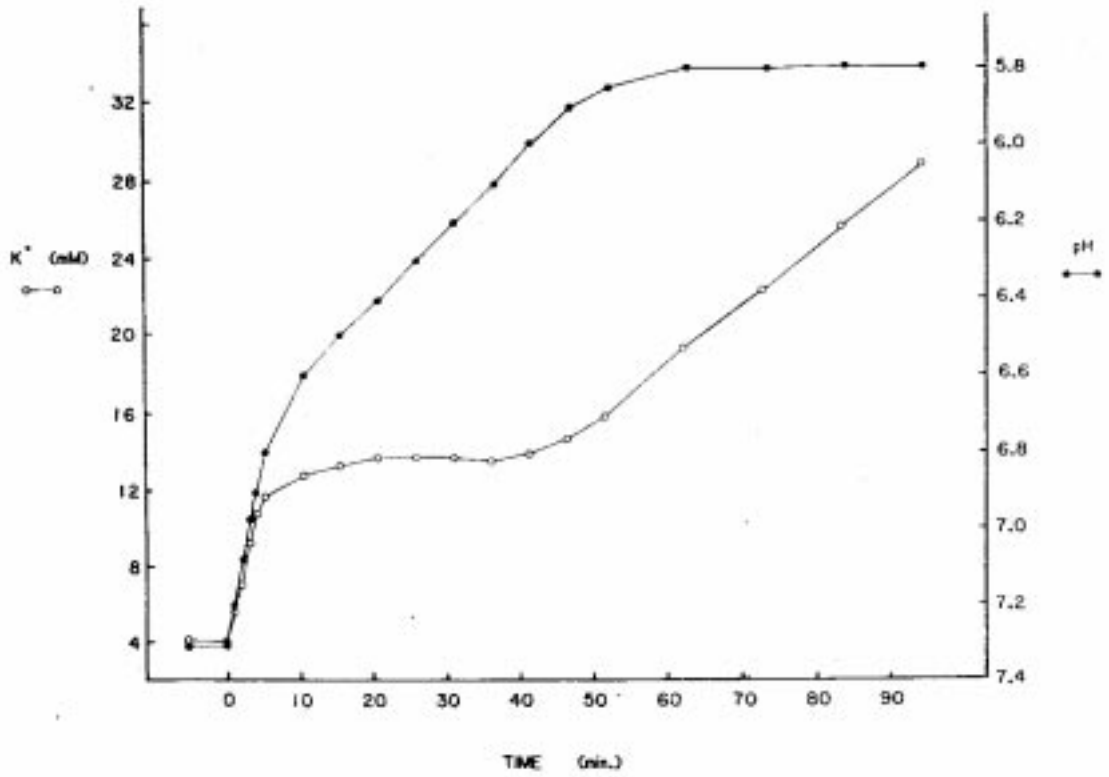

(b)

Figure 1.1 continued

The depolarized RMP mimicked the effect of increased extracellular potassium on a cardiac cell. The coupling conductance was varied (0nS, 3nS, 5nS). No spontaneous repetitive change in transmembrane potential (also termed automaticity) was observed. Kumar and Joyner [16] later reconfirmed this result with a depolarized model cell RMP of 0mV coupled to a VC, but noted that with the application of certain drugs, isoproterenol (synthetic catecholamine which acts to stimulate β_1 and β_2 adrenergic receptors), froskolin and 8-bromo-cyclic adenosine monophosphate (which act to raise cAMP levels), and Bay K 8644 (slow Ca^{2+} channel agonist) to the VC, early after depolarizations (EADs) were observed. EADs could be produced within the VC only in the presence of these drugs while also being connected to the depolarized model cell. The change of the VC with these drugs, which primarily affect the calcium handling, altered the dynamics to allow for automaticity induced by the injury current.

Wagner et al. [34], extending the work of Kumar et al. [17], coupled a model sinoatrial node (SAN) cell, which was self-oscillatory, to a real VC bathed in either a normal solution or an ischemic solution. Wagner et al. found that the SAN could not drive the VC under any conductance if the effective size of the SAN was not sufficiently large. For large enough SAN there were two critical conductances between which enough current was produced to force the VC into oscillations. Figure 1.2 shows the regions in the parameters conductance versus size of SAN in which the SAN paces but does not drive the VC (PND), the SAN paces and drives the VC (PD), and the SAN does not pace (NP). The ischemic solution applied to the VC increased each critical conductance by about 50%. The relative size of the ischemic region and gap junction conductance are important determinants of automaticity.

1.3 Experiments on Strips of Cardiac Tissue Involving Ischemia

In 1975 Katzung [13] performed a sucrose gap experiment on a strip of papillary muscle (4.5-5mm). The strip remained electrically coupled through two rubber

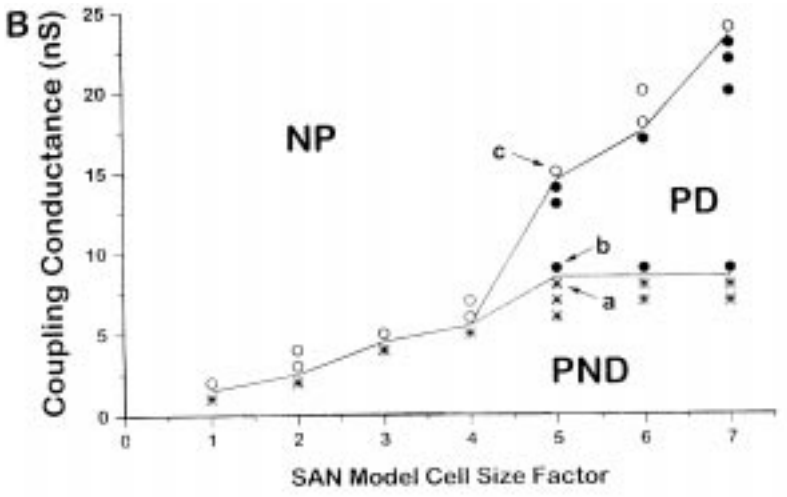

Figure 1.2: Regions of different dynamics of a coupled oscillatory model sinoatrial node (SAN) and rabbit ventricular cell (VC) in parameter space, conductance versus SAN size. The regions are where the SAN paces but does not drive the VC (PND), the SAN paces and drives the VC (PD), and the SAN does not pace (NP). This figure is from Wagner et al. [34].

membranes in the three chambers. High levels of extracellular potassium (145mM) were added to the first chamber and second chamber, while recordings where made in the third chamber perfused with a normal solution. Depolarization of the RMP was observed along with spontaneous action potentials in half of the preparations. Automaticity was enhanced by the addition of epinephrine in the third chamber.

Kupersmith, in 1994, [18] performed a two-chamber experiment on a sheep Purkinje fiber. Half of the fiber was treated with a Ethylenediame tetraacetic acid (EDTA) which had the effect of prolonging the action potentials in that region. The effect of the prolonged action potential was to allow a current to flow from the EDTA treated region to the normal region. Transmembrane potential levels were recorded in the EDTA treated region, 0.5mm from the membrane boundary in the normal region, and 3-4mm into the normal region. Elevated transmembrane potential from the plateau in the treated region caused automaticity in the normal region. Automaticity was observed to initiate at the border between treated and untreated regions 50% of the time, in the treated region 20% of the time, or simultaneously

at the border and the treated region 30% of the time.

Little has been done to model the border zone phenomenon, but Muller-Borer in 1995 [24] performed simulations of a string of coupled cells of varying and fixed lengths with a gradient of K_0^+, 8mM/cm, across approximately 10mm. She used Lou-Rudy I dynamics (see Appendix A or [20]) where K_0^+ was an explicit parameter. She also included resistive barriers in the form of high gap junctional resistance. She compared stimulated action potential propagation when encountering a resistive barrier while coming from a high K_0^+ region into a region of low K_0^+ or coming from a low K_0^+ region into a region of high K_0^+. Propagation was much more likely to fail when the action potential was moving into a region of low K_0^+.

More recently Picard and Rouet [26, 30] performed experiments on strips of guinea pig cardiac tissue extending Rouet's work from 1989 [29]. Their goal was to find pharmaceutical remedies for automaticity at the ischemic border zone by affecting the K_{ATP} channel. They used a two-chamber setup where one chamber was perfused with an ischemic Tyrode's solution containing high K_0^+, low pH, no glucose, and a decreased partial pressure of oxygen, pO_2. Their control experiments found spontaneous electrical behavior a fourth of the time. After perfusion of half of the tissue preparation with the ischemic solution for 30 minutes, that part of the tissue was reperfused with a normal solution. In the control, 92% of the preparations exhibited spontaneous activity upon reperfusion.

1.4 Modeling of the Ischemic Border Zone

These experiments attempt to understand the influence ischemic tissue exerts on normal tissue. The coupled cell experiments focus on the importance of depolarized resting transmembrane potential in ischemic tissue and the size of ischemic tissue in generating automaticity. The strip of tissue experiments also emphasize the importance of elevated ischemic transmembrane potential in generating oscillations when coupled to normal tissue. However, these experiments fall short of providing a ubiquitous mechanism for automaticity, and previous modeling does not reproduce automaticity observed in experiments.

The goal of this thesis is to understand how the depolarization of the ischemic myocardium in early ischemia while still coupled to normal myocardium generates spontaneous electrical activity independent of the normal automaticity of the heart. This is the generation of a so called "border zone arrhythmia." To this end, we develop and study a coupled cell/region model with three forms of ionics and a one-dimensional spatial model. These models are inspired by the above mentioned experiments.

In Chapter 2 we derive the model of coupled cells (or coupled isopotential regions). Coupling strength, relative sizes of ischemic and normal regions, and degree of ischemia are parameters in the model. Three forms of dynamics are considered. Bifurcation diagrams are used to identify regions of distinct dynamic behavior in parameter space. We state and prove a theorem that relates forcing of a single cell or region to behavior of the coupled system, and then relate the bifurcation results to experiments.

In Chapter 3 we develop a one-dimensional spatial model of an ischemic border zone. We consider a piecewise linear model of the cardiac ionics. We prove existence and uniqueness of the steady state for all parameter values and analytically determine regions in parameter space where a steady state of the spatial model is unstable yielding spontaneous oscillations. We use this model to make a qualitative comparison with the Picard and Rouet experiments.

CHAPTER 2

COUPLED CELL MODEL

2.1 Introduction

In this chapter we derive a model of coupled cells where "cell" may be interpreted as a single cell or a group or region of isopotential cells. The degree of ischemia is described by the parameter vector, $\mathbf{P}$. One cell, taken to be a normal cell, has no ischemia, $\mathbf{P} = \mathbf{p_0}$, whereas the other cell, taken to be the ischemic cell, has a variable degree of ischemia, $\mathbf{P} = \mathbf{p}$. The coupling parameter is associated with proteins, which span both cell membranes linking them together electrically, called gap junctions. This coupled system of ordinary differential equations is studied with three different models of transmembrane ionic current, a reduced Hodgkin-Huxley model, a modified McKean model, and a Luo-Rudy I model.

The reduced Hodgkin-Huxley (RHH) ionic model is a basic ionic model that incorporates sodium and potassium ion currents. This model is found as a reduction of the four variable Hodgkin-Huxley model by assuming the sodium gate activation is fast and the potassium gate activation and sodium gate inactivation are linearly related. The two variable RHH model allows for phase plane analysis while maintaining an ionic description and interpretation. We alter this reduced model to account for changes from ischemia by allowing for changes in K_0^+. In the phase plane, the nullcline of the transmembrane potential, V, undergoes a characteristic shift in response to the change in K_0^+. A modification, in line with this characteristic shift, to McKean's two variable piecewise linear model yields a model for which analytical calculations are done. Finally, an eight variable, more physiological ionic model, Luo-Rudy I, with explicit dependence on K_0^+ is examined.

From the analysis of spontaneous oscillations in these models, a general concept emerges. A theorem, relating this general concept, describes how internal changes

and external forcing of a single cell relates to oscillatory behavior of coupled cells in certain parameter ranges.

We conclude that two cells, which when uncoupled are each stable, one excitable and the other inexcitable with elevated resting potential, can exhibit oscillations when coupled together . Finally, we compare the results to the coupled cell experiments [31, 32, 16, 34, 17] and give an explanation of why oscillations are not observed in some experiments [32, 16].

2.2 Derivation of the ODE Model

The models of the cardiac cell ionics described here are based on the Hodgkin-Huxley formalism. The membrane of a cardiac cell is a bilipid layer that acts as a capacitor. Through this layer, penetrating proteins act as ion specific conductors. The Nernst potential for a specific ion comes from balancing the difference in concentrations across a membrane with its potential difference. The combination of the specific Nernst potentials may be loosely interpreted as a single battery. Figure 2.1 provides a schematic representation of two excitable cells coupled through an intercellular resistance.

The total transmembrane current consisting of the ionic currents and the induced capacitive current must balance the current through the intercellular resistor, I_{coup}. The membrane current density is

$$I_m = C_m \frac{dV_1}{dt} + I_{ion}$$

where $V_1 = V_{1_i} - V_{1_e}$, C_m is capacitance per unit area, and I_{ion} is the ionic current density. Using Ohm's law the intercellular current density is written in terms of the difference in intercellular potentials and the conductance per area, d, between them,

$$I_{coup} = d(V_{1_i} - V_{2_i})$$

where d is also the inverse intercellular resistivity, R_d. The conductance, d, is associated with the gap junctional conductance. For the currents induced from the flow of ions to balance, the surface areas across which the various currents flow

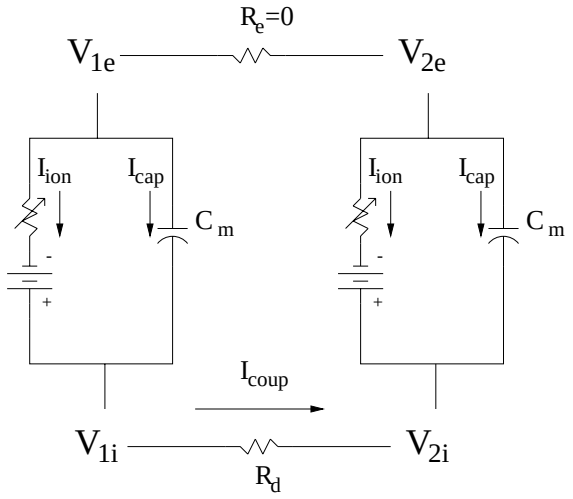

Figure 2.1: A schematic of two cells coupled intracellularly by the coupling current, $I_{\mathbf{coup}}$. The ionic current, $I_{\mathbf{ion}}$, and capacitative current, $I_{\mathbf{cap}}$ are balanced by the coupling current. R_d is the coupling resistivity. C_m is the membrane capacitance. V_{1_e} and V_{1_i} are the intracellular and extracellular potentials for region 1, respectively, as are V_{2_e} and V_{2_i} for region 2. The extracellular potentials are taken to be isopotential, $(V_{1_e} = V_{2_e})$.

must be taken into account. If M_1 represents the membrane surface area of cell 1 and A_i represents the gap junctional surface area between cell 1 and cell 2, then the balance of currents for cell 1 is

$$M_1(C_m\frac{dV_1}{dt} + I_{ion}) = A_i I_{coup} = A_i d(V_{1_i} - V_{2_i}),$$

and for cell 2 is

$$M_2(C_m\frac{dV_2}{dt} + I_{ion}) = -A_i I_{coup} = A_i d(V_{2_i} - V_{1_i}).$$

We assume that the extracellular potential is isopotential (i.e., $V_{1_e} = V_{2_e}$) so that the two coupled transmembrane potential equations become

$$\begin{aligned} M_1(C_m\frac{dV_1}{dt} + I_{ion}) &= A_i d(V_2 - V_1), \\ M_2(C_m\frac{dV_2}{dt} + I_{ion}) &= A_i d(V_1 - V_2). \end{aligned} \tag{2.1}$$

2.3 Scaling Parameters

It is useful to introduce scaled parameters in (2.1). Let M_0 be the total membrane surface area of the system (i.e., $M_1 + M_2 = M_0$), and let m be the relative surface area of cell 1, $m = \frac{M_1}{M_0}$, which is a nondimensional quantity. Notice then that $1 - m = \frac{M_2}{M_0}$. If the ratio of gap junctional surface area, A_i, to total surface membrane area, M_0, is χ, then (2.1) takes the form.

$$\begin{aligned} m(C_m \frac{dV_1}{dt} + I_{ion}) &= \chi d(V_2 - V_1), \\ (1-m)(C_m \frac{dV_2}{dt} + I_{ion}) &= \chi d(V_1 - V_2). \end{aligned} \tag{2.2}$$

The ionic current, I_{ion}, has many possible representations depending on which ions are found to flow across the membrane and on what physiological model is being considered. A discussion of several ionic models can be found in Keener and Sneyd [15]. In general, it is assumed that the ionic current has a functional nonlinear dependence on the transmembrane potential, on gating variables and other state variables, and on state dependent parameters. For example,

$$I_{ion} = -F(V, \mathbf{w}, \mathbf{P})/R_m$$

where R_m is the passive membrane resistivity, F has units of voltage, $\mathbf{w}$ represents the vector of gating variables and other state variables, and $\mathbf{P}$ represents a vector of parameters (i.e., K_0^+, pH, ATP, etc.) which undergo biochemical changes under ischemic conditions. Incorporating this into (2.2) yields

$$m\left(C_m R_m \frac{dV_1}{dt} - F(V, \mathbf{w}_1, \mathbf{P})\right) = \chi R_m d(V_2 - V_1),$$

$$(1-m)\left(C_m R_m \frac{dV_2}{dt} - F(V, \mathbf{w}_2, \mathbf{P})\right) = \chi R_m d(V_1 - V_2).$$

Notice that $C_m R_m$ has units of time and $R_m d$ is a nondimensional product of intercellular conductance per area and passive membrane resistivity, so that scaling time by $C_m R_m$ and letting $\delta = R_m d$ yields the model

$$m\left(\frac{dV_1}{dt} - F(V, \mathbf{w}_1, \mathbf{p})\right) = \chi\delta(V_2 - V_1),$$

$$(1-m)\left(\frac{dV_2}{dt} - F(V, \mathbf{w}_2, \mathbf{p})\right) = \chi\delta(V_1 - V_2).$$

The dynamics of gating variables for each of the cells are described by equations of the form

$$\begin{aligned} \frac{d\mathbf{w}_1}{dt} &= g(V_1, \mathbf{w}_1) \\ \frac{d\mathbf{w}_2}{dt} &= g(V_2, \mathbf{w}_2) \end{aligned}$$

To model the effect of ischemia on the electrical interaction between cells, the degree of ischemia parameters, $\mathbf{P}$, are modified in one of the cells. The ischemic cell, cell 2, parameters are denoted $\mathbf{P} = \mathbf{p}$, while the normal cell, cell 1, has system parameters $\mathbf{P} = \mathbf{p_0}$. For example, if $\mathbf{P} = P$, a scalar, represents K_0^+, we let p_0 be K_0^+ for a normal cell, while p is K_0^+ for an ischemic cell, $p > p_0$. The following system of coupled equations, including the equations for recovery dynamics, is the basis for the coupled cell study in the following sections.

$$\begin{aligned} m\left(\frac{dV_1}{dt} - F(V_1, \mathbf{w}_1, p_0)\right) &= \chi\delta(V_2 - V_1) \\ \frac{d\mathbf{w}_1}{dt} &= g(V_1, \mathbf{w}_1) \\ (1-m)\left(\frac{dV_2}{dt} - F(V_2, \mathbf{w}_2, p)\right) &= \chi\delta(V_1 - V_2) \\ \frac{d\mathbf{w}_2}{dt} &= g(V_2, \mathbf{w}_2) \end{aligned} \tag{2.3}$$

Our goal is to understand the behavior of the above system as it depends on the parameters m, p, and $\chi\delta$.

2.4 Reduced Hodgkin-Huxley Model Ionics

To understand how the ischemia parameter affects a cell, we consider a reduction from Hodgkin and Huxley's model for squid giant axon [11]. Extracellular potassium is an explicit component of the potassium Nernst potential in this ionic model and K_0^+ is a prominent factor in ischemia. In the reduced Hodgkin-Huxley (RHH) model, the recovery variable is $\vec{w} = n$, where n represents the fraction of potassium channel activation gates which are open. If we let $\mathbf{P} = P$ represent extracellular potassium, then

$$F(V,n,P) = -[\bar{g}_{Na} m_\infty^3 (0.85 - n)(V - V_{Na}) + \bar{g}_K n^4 (V - V_K(P)) + g_L(V - V_L)],$$

$$g(V,n) = \frac{n_\infty(V) - n}{\tau_n(V)},$$

where the parameters are defined in Table 2.1 and come from Keener and Sneyd [15]. The potassium Nernst potential, $V_K = 25.8 \ln(\frac{P}{K_i})$, depends explicitly on the parameter P.

2.4.1 Single Cell RHH Model

Consider the single cell with RHH dynamics,

$$\begin{aligned} \frac{dV}{dt} &= F(V,n,P) \\ \frac{dn}{dt} &= g(V,n) \end{aligned} \tag{2.4}$$

Since the RHH model is a two-state variable model, it is useful to examine the dynamics in the phase plane. In Figure 2.2 the V-nullcline, a cubic-like shape, and n-nullcline are plotted for a normal level of extracellular potassium, $P = p_0 = 20$. One stable steady state exists. At this parameter value the system is excitable, meaning that when the state of a cell is shifted quickly and sufficiently from its resting position, the state variables travel away from the steady state before returning to rest. The direction of flow is designated by the arrows in Figure 2.2.

The V-nullcline depends on P through the potassium Nernst potential in this model. The effect of increasing $P = p$ on the V-nullcline is shown in Figure 2.3 (a). As p increases, the lower knee of the V-nullcline raises, and with it, the steady state values of both V and n increase. The steady state transmembrane potential as a function of p, $V^*(p)$, is shown in Figure 2.3 (b). This steady state solution remains stable as p increases until it undergoes a change in stability, a bifurcation. At this bifurcation point, near $p \approx 27.5$, a pair of eigenvalues have zero real part and nonzero imaginary part. This bifurcation is a subcritical Hopf bifurcation. Beyond this point, the only stable solution to the system (2.4) is a large amplitude stable periodic orbit. As p continues to increase, following the smallest steady solution

Table 2.1: Table of values for the RHH model

Symbol	Function	Value (Units)
$\bar{g}_{Na}$	Max Sodium Channel Conductance	120 (mho)
$\bar{g}_K$	Max Potassium Channel Conductance	86 (mho)
g_L	Leak Channel Conductance	0.3 (mho)
V_{Na}	Sodium Nernst Potential	56 (mV)
V_L	Leak (Composite) Nernst Potential	-54.4 (mV)
V_K	Potassium Nernst Potential	$25.8 \ln(\frac{p}{K_i})$ (mV)
K_i	Intercellular Potassium Concentration	397 (mM)
$m_\infty(V)$	Steady State Open Probability for the Sodium Channel Activation Gate	$\frac{\alpha_m(V)}{\alpha_m(V)+\beta_m(V)}$
$\alpha_m(V)$	Rate of Sodium Channel Activation Gate Opening	0.1(V+40)/(1 - exp(-(V+40)/10))
$\beta_m(V)$	Rate of Sodium Channel Activation Gate Closing	4exp(-(V+65)/18)
$n_\infty(V)$	Steady State Open Probability for the Potassium Channel Activation Gate	$\frac{\alpha_n(V)}{\alpha_n(V)+\beta_n(V)}$
$\tau_n(V)$	Time Constant for the Potassium Channel Activation Gate Dynamics	$\frac{1}{\alpha_m(V)+\beta_m(V)}$
$\alpha_n(V)$	Rate of Potassium Channel Activation Gate Opening	0.01(V+55)/(1-exp(-(V+55)/10))
$\beta_n(V)$	Rate of Potassium Channel Activation Gate Closing	0.125exp(-(V+65)/80)

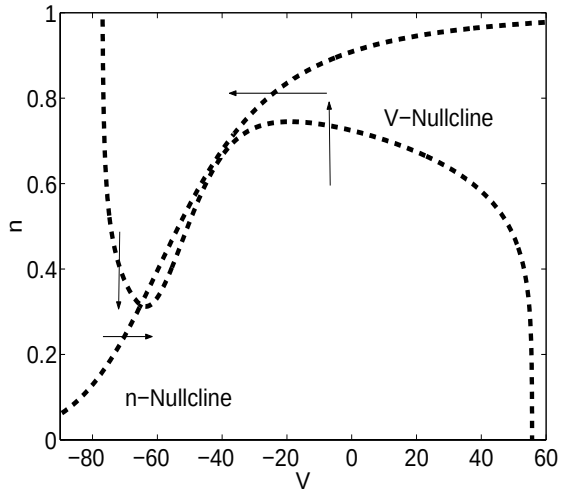

Figure 2.2: Phase plane diagram for the RHH model. The steady state is stable with extracellular potassium at a normal level, $P = p_0 = 20$.

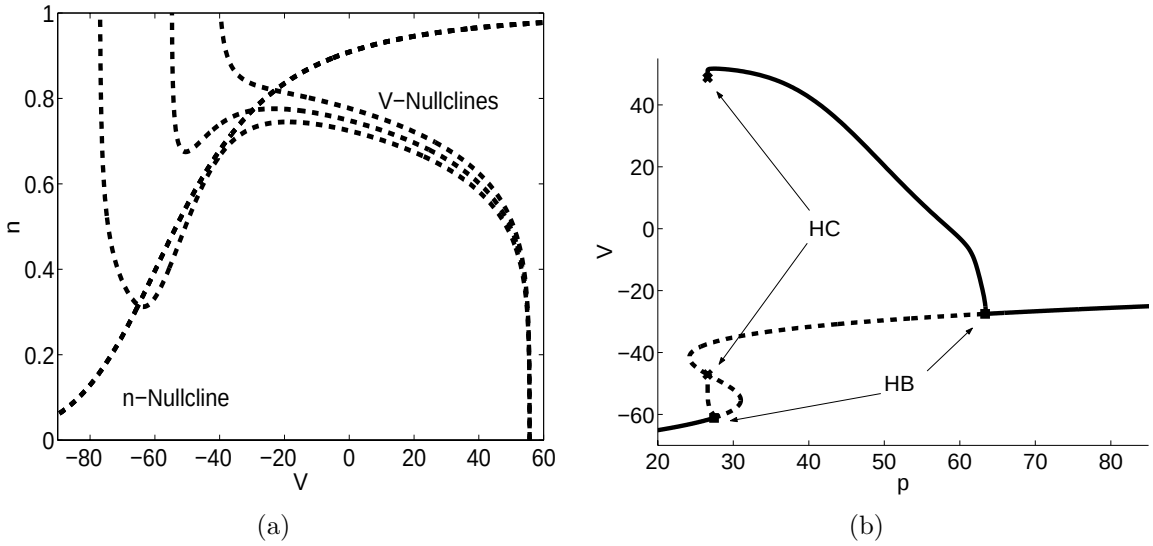

(a) (b)

Figure 2.3: Effects of increasing the degree of ischemia parameter on a single RHH model cell. (a) Shift in V-nullcline. This picture shows three different V nullclines corresponding to increases in extracellular potassium (p = 20 (normal), 45, and 90) for the RHH model. These show the depolarization of the transmembrane potential steady state as it depends upon p. (b) Steady state diagram. Increase of steady state transmembrane potential as it depends upon p in an S-shape manner for the RHH model. The squares indicate Hopf bifurcations (HB) ($p \approx 27.5$ and $p \approx 63.5$), where the steady state becomes unstable and then restabilizes, respectively. The two curves emanating from the lower HB and upper HB and ending at the Homoclinic points (HC) marked by X's are the amplitude of the unstable and stable period orbits, respectively. There is a small region of overlap between the stable periodic orbit and the stable steady state on the lower branch yielding bistability.

$V^*(p)$, we reach a knee of the steady state curve, which is the first of two limit point bifurcations ($p \approx 31$ and $p \approx 24$). Eventually for a sufficiently high p-value, the steady state regains its stability through a second, supercritical Hopf bifurcation at $p \approx 63.5$. The lower stable branch of the S-shaped steady state curve represents a stable, excitable state, and the upper stable branch beyond the second Hopf point represents a stable, inexcitable state. The periodic solution that exists for intermediate p-values is a self-oscillatory solution. The region between the p-value where the stable periodic solution ends in a homoclinic orbit (HC) ($p \approx 26.5$) and the p-value of the lower Hopf point is a region of bistability where the stable periodic and stable steady state coexist.

2.4.2 Coupled RHH Model Cells

Now that we understand how the RHH dynamics of the single cell change with variation in p, we would like to understand how the coupling strength and mass of the individual cells affect the coupled cell dynamics. We couple two cells, one normal and one ischemic, each with RHH model dynamics. It is clear that if p is elevated only slightly in the ischemic cell, regardless of the coupling strength or mass differential, both cells remain at resting states only slightly different from what would be their uncoupled resting states. This steady state is stable for the four state variable system.

Beyond this, however, the dynamics of the coupled system (2.3) are not immediately obvious. Evidence for interesting nontrivial behavior is shown in a time course plot for the coupled system with RHH ionics in Figure 2.4. Here, an ischemic cell of relative mass $1 - m = 0.9$ with $p = 80$ is uncoupled, Figure 2.4 (a), and then coupled, Figure 2.4 (b), by $\chi\delta = 0.15$ to a normal cell of relative mass $m = 0.1$ with $p_0 = 20$. When the two cells are uncoupled, both approach their respective stable steady states, but when coupled, the normal cell is forced by the current induced from the high resting potential of the ischemic cell, which is in its stable inexcitable state.

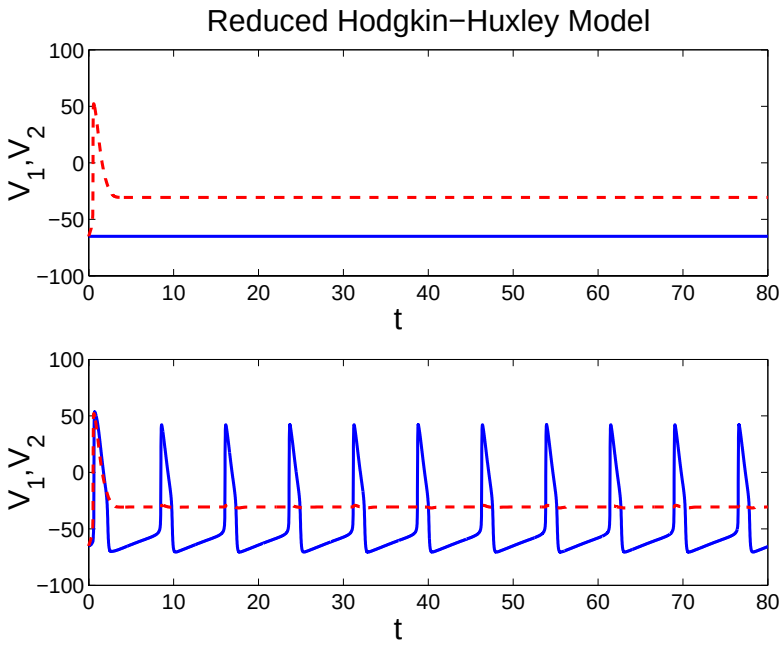

Figure 2.4: Reduced Hodgkin-Huxley model. The upper graph shows the steady states for the system if uncoupled (i.e., $\chi\delta = 0$) with $p = 80$ in the ischemic cell. The lower graph shows the system coupled with $\chi\delta = 0.15$, $p = 80$ and $m = 0.1$. The ischemic cell remains at its resting transmembrane potential, and it acts as a source of current to force the normal cell into oscillation. The dashed lines are the ischemic cell transmembrane potentials, while the solid line is the transmembrane potential for the normal cell.

The steady state behavior in Figure 2.4 is different in the top and the bottom subfigures, and the only change has been to the composite parameter, $\frac{\chi\delta}{m}$. We determine that the coupled system has gone through a Hopf bifurcation. We define a curve in parameter space along which at least two of the eigenvalues of the coupled system (2.3) have zero real part and nonzero imaginary part as a Hopf curve. Figure 2.5 shows Hopf curves in $\frac{\chi\delta}{m}$ vs. p parameter space for two size parameters, $m = 0.1, 0.5$.

The shaded region is the set of parameter values at which oscillations are guaranteed. The solid curves, HB_1 and HB_2, are Hopf curves. The dotted curves, LP_1 and LP_2, are limit point curves along which a real eigenvalue remains zero. The dashed curve is a secondary Hopf curve. The Hopf curves and limit point curves are calculated using Auto97 bifurcation software [6]. The star points, one of which is labeled HC, are the p-values for a given $\frac{\chi\delta}{m}$ at which the periodic solution emanating from HB_2 becomes homoclinic. Since HC is below HB_1 for a given $\frac{\chi\delta}{m}$, between HC and HB_1 in p is a region of bistability. Depending upon the initial conditions, the system either approaches the steady state solution or the periodic orbit. As m increases the upper Hopf curve, HB_2, shifts outward (outside of picture frame) increasing the upper bound on the oscillatory region. The lower Hopf curve, HB_1, and homoclinic points, HC, also shift upward with increasing m except for being pinned at the p-axis. This increases the lower bound on oscillations for each $\frac{\chi\delta}{m} > 0$.

Looking more closely in a neighborhood of the p-axis in Figure 2.6 we identify the interval in p which correlates with the uncoupled ischemic cell oscillation, $p \in [27.5, 63.5]$. For small m we expect that the normal cell to have little effect on the ischemic cell so that as the coupling increases we expect $p \in [27.5, 63.5]$ to remain an oscillatory region, which it indeed does in Figure 2.6 (a). However, for $p > 63.5$ and coupling sufficiently large, we find another instability region which extends to the HB_2 curve (see Figure 2.5 (a)). This region represents oscillatory dynamics from two coupled cells that if uncoupled would each approach its stable rest state. Figure 2.4 shows an example of cells in such a parameter region.

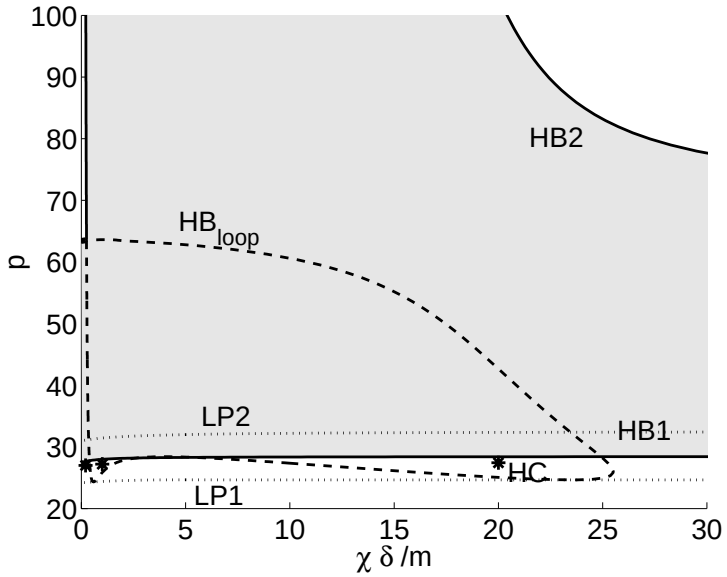

(a)

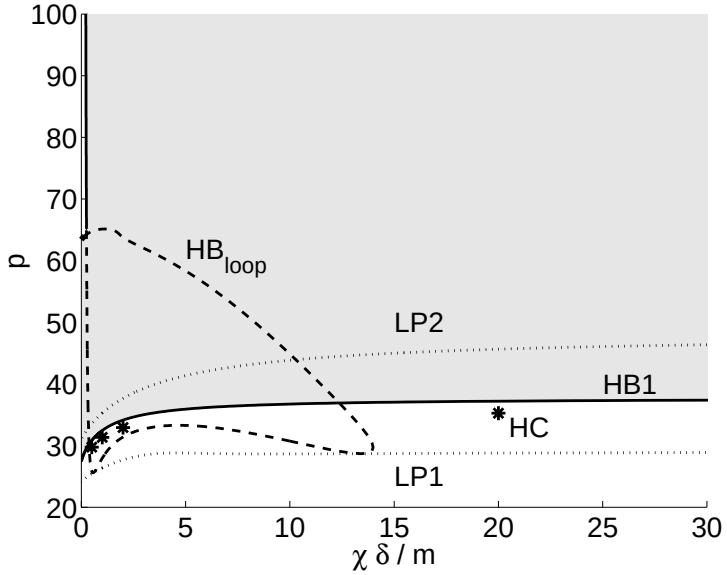

(b)

Figure 2.5: Unfolding diagrams for $\frac{\chi\delta}{m}$ vs. p at fixed m=0.1 and m=0.5. The shaded region is the set of parameter values at which oscillations are guaranteed. The solid curves, HB_1 and HB_2, are Hopf curves. The dotted curves, LP_1 and LP_2, are limit point curves. The dashed curve is a secondary Hopf curve. The star points, one of which is labeled HC, are the p-values for a given $\frac{\chi\delta}{m}$ at which the periodic solution emanating from HB_2 becomes homoclinic. Since HC is below HB_1, between HC and HB_1 in p is a region of bistability. The lower Hopf curve, HB_1, and homoclinic points, HC, also shift upward for increasing m except for being pinned at the p-axis.

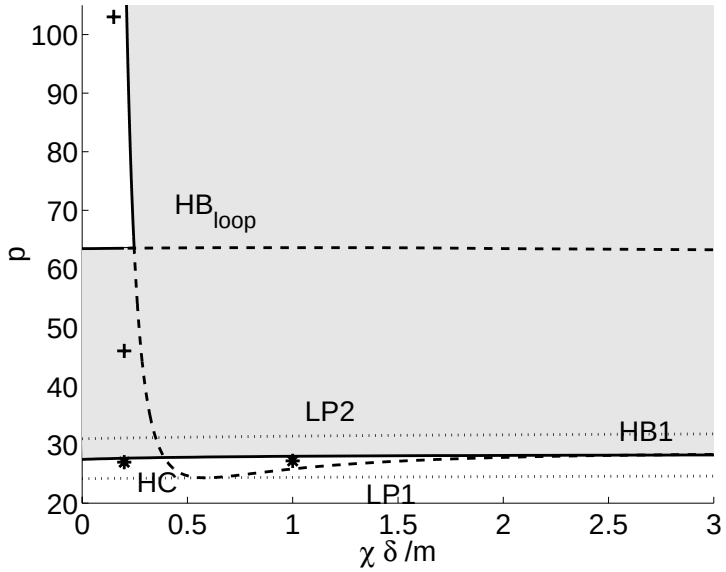

(a)

Figure 2.6: Unfolding diagrams for $\frac{\chi\delta}{m}$ vs. p at fixed m=0.1, m=0.5, m=0.9 zoomed into small $\frac{\chi\delta}{m}$. (a) and (b) focus on the region closer to the p-axis of Figure 2.5 (a) and (b), respectively. (c) For $m = 0.9$, the slope of the HB_1 curve has dramatically increased compared to the (a) and (b) and the curve ends in a Bogdonov-Takens, BT_1, bifurcation. With the loss of the HB_1 curve, the boundary for purely oscillatory solutions becomes the limit point curve, LP_1. Between the HC points and the LP_1 curve there exists a region of bistability.

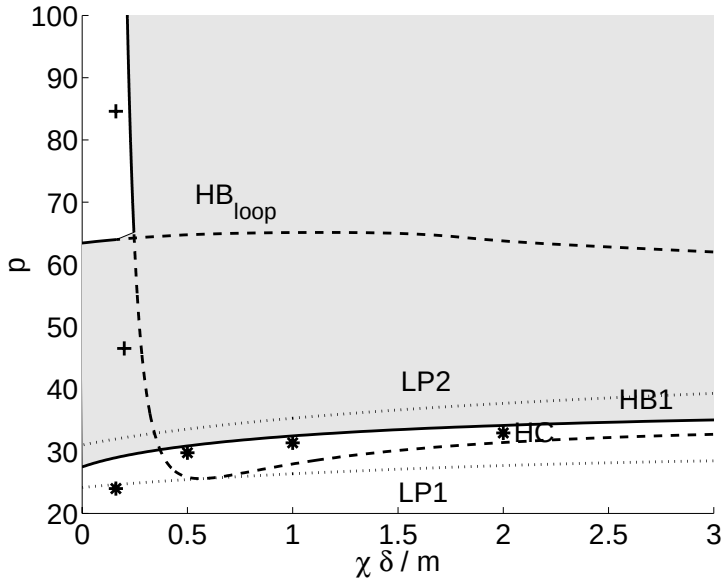

(b)

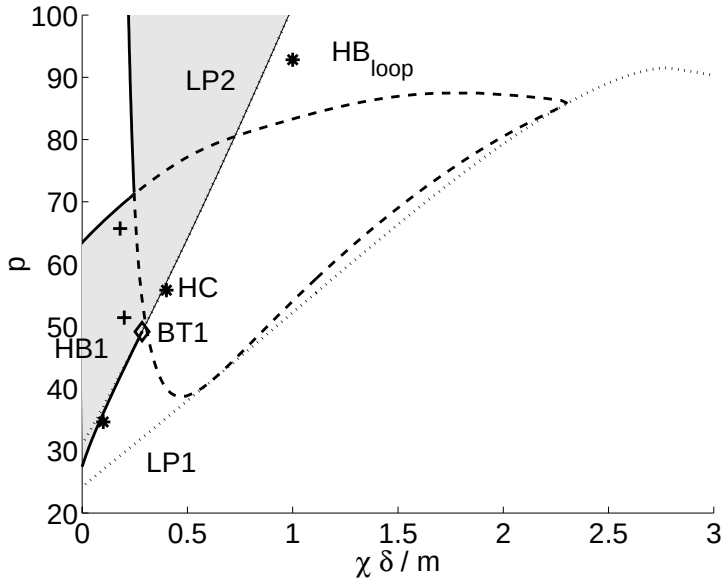

(c)

Figure 2.6 continued

As m increases the HB_1 curve rises away from $\frac{\chi\delta}{m} = 0$ indicating that the reduced ischemic cell needs higher p-values to begin oscillating. For m large enough the HB_1 curve coalesces with the LP_2 curve and disappears above $\frac{\chi\delta}{m}$ values denoted by the Bogdonov-Takens bifurcation point, BT_1. The boundary for the instability region is then the LP_2 curve for $\frac{\chi\delta}{m}$ above BT_1. (See Appendix B for further details.)

2.5 Modified McKean Model Ionics

We wish to determine if single cell oscillations are required in order for the coupled system to exhibit oscillations. To address this question we use a piecewise linear model for the ionics. From this we find analytical expressions for the bifurcation boundaries in terms of various system parameters including a parameter k which determines whether or not a single cell is oscillatory under increase in P.

The McKean model was first described in [21] and has FitzHugh-Nagumo like, triphasic dynamics but is piecewise linear with three branches. [1] We modify the McKean model by adding a constant shift in the left branch where the shift is linearly dependent on the degree of ischemia parameter, P, and by varying the threshold value of V by $\frac{P}{k}$ with other parameters chosen for continuity.

For the modified McKean (MM) model, we take

$$F(V,w,P) = \begin{cases} -V+P & V \le \frac{a}{2} + \frac{P}{k} \\ \sigma V + \eta & \frac{a}{2} + \frac{P}{k} \le V \le \frac{1+a}{2} \\ -V+1 & \frac{1+a}{2} \le V \end{cases} - w$$

where

$$\sigma = \frac{2Pk - 2P - k}{2P - k}$$

and

$$\eta = \frac{2P + ak - aPk - Pk}{2P - k}.$$

The recovery dynamics are described by $g(V,w) = \epsilon(V - \gamma w)$ for w a scalar. Throughout, we take $a = 0.02$ and $\gamma = 0.2$.

---

[1] The results that follow cannot be obtained with McKean's two branch piecewise linear model as also described in [21] The results here require that the slope of the middle branch be positive and bounded.

The parameter P is the degree of ischemia parameter with k modifying the trajectory of the lower knee under changes in P as in Figure 2.8. The MM model mimics several qualitative features of the transmembrane potential behavior in an ischemic cell. The resting membrane potential is raised with elevated P, and the action potential duration is shortened. For large enough values of P the V-nullcline becomes monotonic rendering the dynamics inexcitable.

2.5.1 Single Cell MM Model

We first examine the single cell with MM dynamics,

$$\begin{aligned} \frac{dV}{dt} &= F(V, w, P), \\ \frac{dw}{dt} &= g(V, w). \end{aligned} \tag{2.5}$$

Since the MM model is a two-state variable model, we again look at the dynamics in the phase plane. In Figure 2.7 the V-nullcline, a piecewise linear triphasic curve, and w-nullcline are plotted for a normal level of extracellular potassium, $P = p_0 = 0$. There is one steady state which is stable. At this parameter value the system is excitable. The direction of flow is designated by the arrows in Figure 2.7.

Figure 2.8 shows the changes to the V-nullcline with increases in p for two k-values. For k-values larger than k_c where $k_c = \frac{(1-a)(1+\gamma)}{\gamma - a(1+\gamma)} \approx 6.7$, the lower knee is above the w-nullcline leaving the steady state on the positive sloped middle branch of the V-nullcline and unstable. For $k < k_c$, the lower knee always remains below the w-nullcline and the steady state remains stable on the left branch of the V-nullcline. Figure 2.9 shows the steady state transmembrane potential and its stability for two choices of k as it depends upon p. For each k-value, the steady state transmembrane potential becomes less depolarized as p increases. The upper curve in Figure 2.9 is unstable for a range of p-values since $k > k_c$.

The curve of steady state V-values as a function of p, $V^*(p)$, is found analytically in the MM model to be

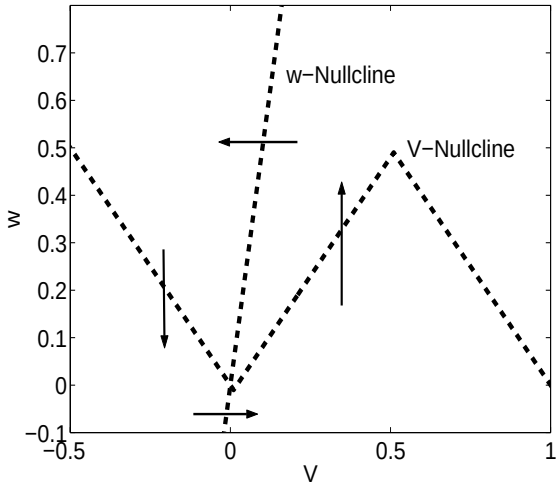

Figure 2.7: Phase plane diagram for the MM model. The steady state is stable with extracellular potassium at a normal level, $p_0 = 0$.

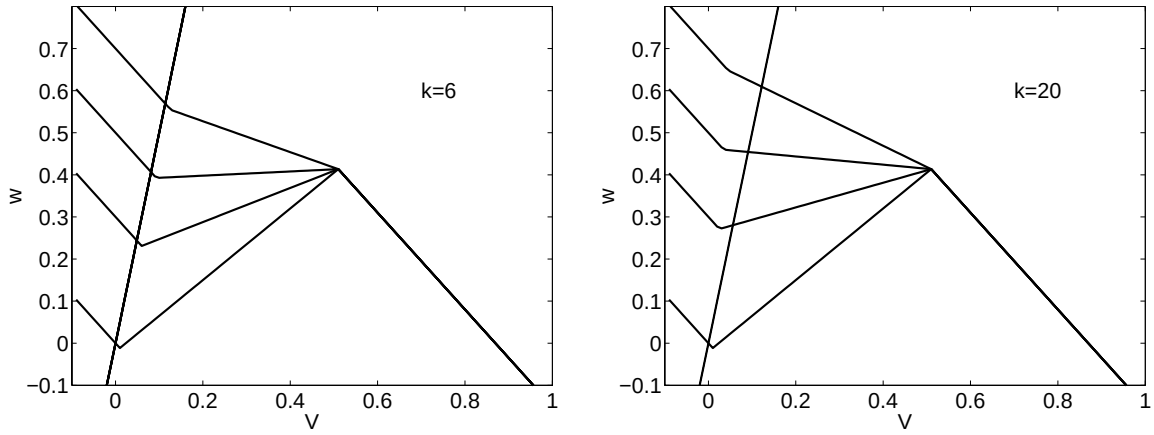

(a) (b)

Figure 2.8: Shift in V-nullcline. (a)Three different V nullclines corresponding to increases in extracellular potassium ($p = 0$ (normal), 0.3, 0.5, and 0.7) for the MM model with $k = 6$. (b) Three different V nullclines corresponding to increases in extracellular potassium ($p = 0$ (normal), 0.3, 0.5, and 0.7) for the MM model with $k = 20$.

$$V^* = \begin{cases} \frac{p}{1+\frac{1}{\gamma}} & 0 < p < \frac{\frac{a}{2}k(1+\frac{1}{\gamma})}{k-1-\frac{1}{\gamma}} \\ \frac{\eta}{-\sigma+\frac{1}{\gamma}} & \frac{\frac{a}{2}k(1+\frac{1}{\gamma})}{k-1-\frac{1}{\gamma}} < p < 1. \end{cases}$$

There is a loss of stability of the steady state solution if $k > k_c$ for $\frac{\frac{a}{2}k(1+\frac{1}{\gamma})}{k-1-\frac{1}{\gamma}} < p < \frac{k}{2(k-1)}$. The steady state solution shifts to the middle branch from the left branch of the V-nullcline when p reaches the lower p bound (lower square in Figure 2.9). As p increases the V-nullcline loses its triphasic appearance and becomes monotonic for p-values above the upper p bound (upper square in Figure 2.9).

Figure 2.10 (a) shows the upper and lower p-bounds for different k values. The associated $V^*(p)$ values are shown in Figure 2.10 (b).

2.5.2 Coupled MM Model Cells

As with RHH, there is interesting nontrivial behavior for the coupled system with MM ionics. Figure 2.11 (a) shows the dynamics of the MM model for a normal cell and an ischemic cell with $p = 0.7$ and $k = 6$, while (b) shows the behavior of the two cells from (a) coupled with $\chi\delta = 0.09$ and $m = 0.1$. In this example, neither of the cells are oscillatory when uncoupled, so that the oscillations must result from the coupling between the two cells.

The boundary of the oscillatory regions can be calculated analytically and are shown for several values of m in Figure 2.12. Since the steady state transmembrane potential of the ischemic cell, $V_2^*(p)$, and its degree of ischemia parameter, p, are functionally related, we can view $V_2^*(p)$ as a parameter. We use $V_2^*(p)$ as the parameter in Figure 2.12, but the plots are similar for $\frac{\chi\delta}{m}$ versus p. In Figure 2.12, as m increases for the $k = 20$ column beyond $m = 0.5$, the nonoscillatory (NO) swath is where the self-oscillatory ischemic cell is quieted when coupled to a sufficiently large normal cell. Only for very weak coupling does the ischemic cell oscillate. For $k = 6$, uncoupled cells do not oscillate, but for appropriate coupling, coupled cells oscillate as shown in the $k = 6$ column of Figure 2.12.

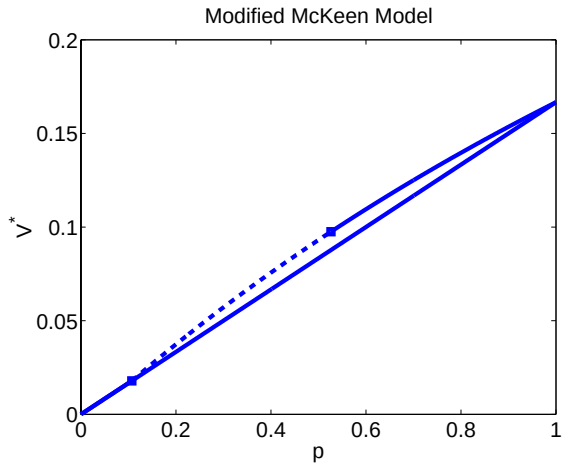

Figure 2.9: Steady state transmembrane potential dependence on p. The upper curve is for $k = 20$, while the lower curve has $k = 6$. The dashed line marks where the steady state is unstable. The beginning and end of the dashed line is marked with squares, which denote the change in stability of the steady state solution. The $k = 20$ curve is qualitatively the same as the RHH model bifurcation curve in Figure 2.3 (b).

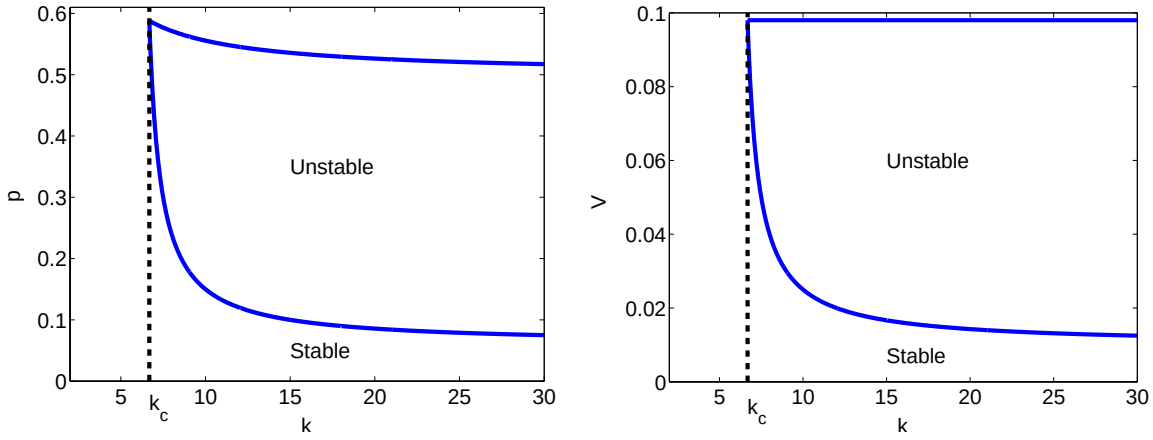

Figure 2.10: Transition curves. (a) Two curves bounding the instability region in k vs. p. (b) Two curves bounding instability region in k vs. V^*. The k-value at which these curves coalesce and disappear is k_c. These two pairs of curves at $k = 20$ are the p and V^*-values in Figure 2.9 at the filled squares.

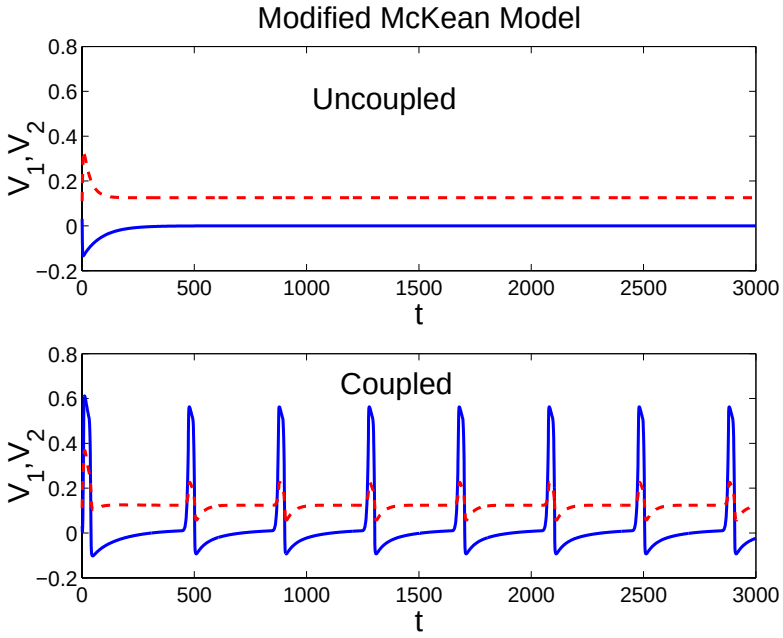

Figure 2.11: Modified McKean model. The upper graph shows the steady states for the system if uncoupled (i.e., $\chi\delta = 0$) with $p = 0.7$ and $k = 6$ in the ischemic cell. The lower graph shows the system coupled with $\chi\delta = 0.09$, $p = 0.7$, $k = 6$ and $m = 0.1$. The ischemic cell remains at its RMP, while it acts as a source of current to force the normal cell into oscillation.

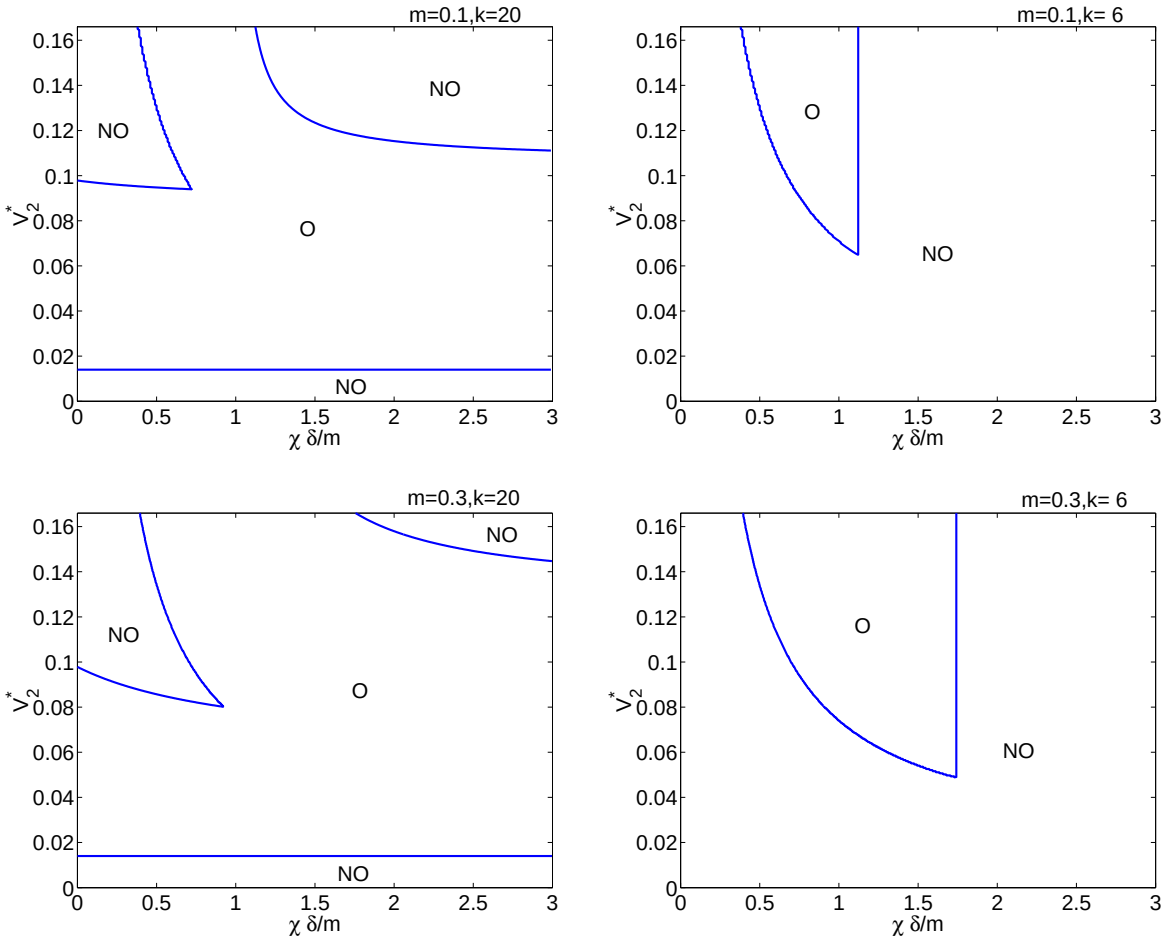

Figure 2.12: Modified McKean Model. Unfolding diagrams for d vs. V_2^* with m and k noted on each subfigure.

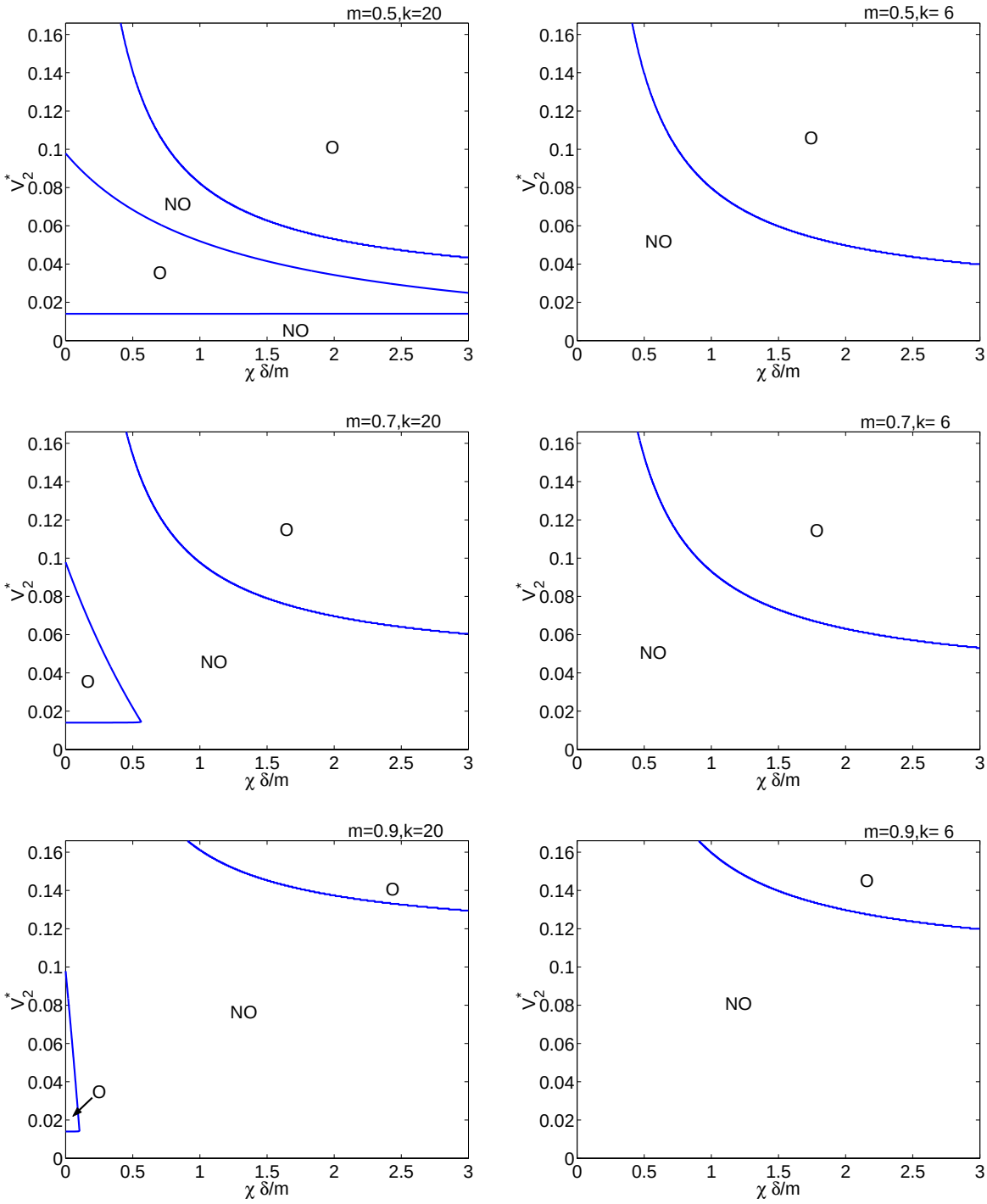

Figure 2.12 continued

2.6 Luo-Rudy I Model Ionics

The state variables in the Luo-Rudy I (LRI) model are the transmembrane potential, gating variables, and intracellular calcium. The $\vec{w} = [m, h, j, d, f, x, Ca_i]$ dynamics are governed by seven differential equations where m, h and j are sodium activating, fast inactivating, and slow inactivating gating variables, respectively; d and f are calcium activating and inactivating gating variables, respectively; x is a potassium inactivating gating variable, and Ca_i is intracellular concentration of calcium.

2.6.1 Single Cell LRI Model

We examine the single cell with LRI dynamics,

$$\begin{aligned} \frac{dV}{dt} &= F(V, w, P), \\ \frac{dw}{dt} &= g(V, w). \end{aligned} \tag{2.6}$$

The equations for the LRI model are found in Appendix A or [20]. We chose this particular physiological model for study because of its explicit dependence on K_0^+ through the potassium Nernst potential and the potassium channel conductance. The single cell steady state diagram for the LRI model is shown in Figure 2.13. The resting transmembrane potential depends monotonically on $p = K_0^+$, and though it becomes more depolarized as p increases, it never loses its stability.

2.6.2 Coupled LRI Model Cells

There is interesting behavior when two LRI model cells are coupled. Figure 2.14 (a) shows the uncoupled dynamics of the LRI model for $p = 60$, while (b) shows the two cells from (a) coupled with $\chi\delta = 0.005$ and $m = 0.1$. In this example, as with the MM model, there is no oscillatory behavior in the ischemic cell so that the oscillation must result from the coupling between the two cells.

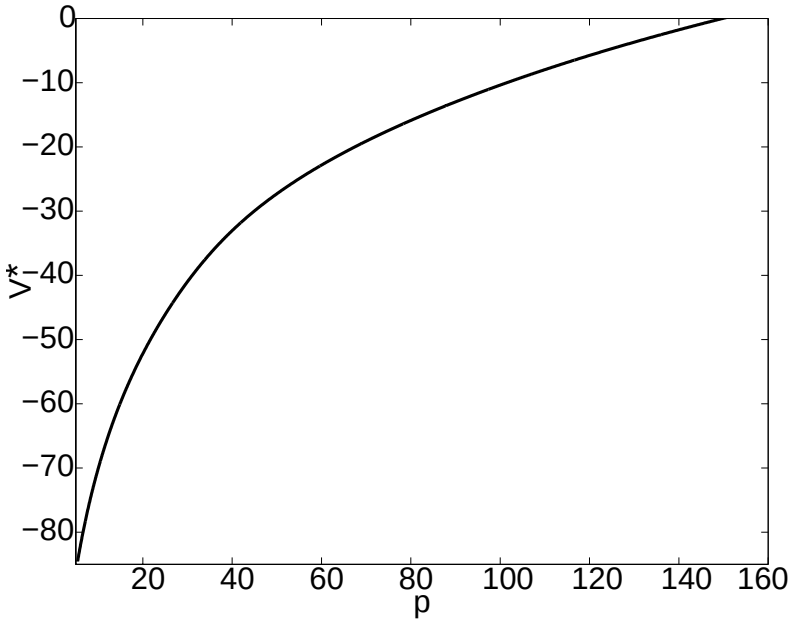

Figure 2.13: Bifurcation diagram which exhibits the steady state transmembrane potential dependence on K_0^+ for the LRI model.

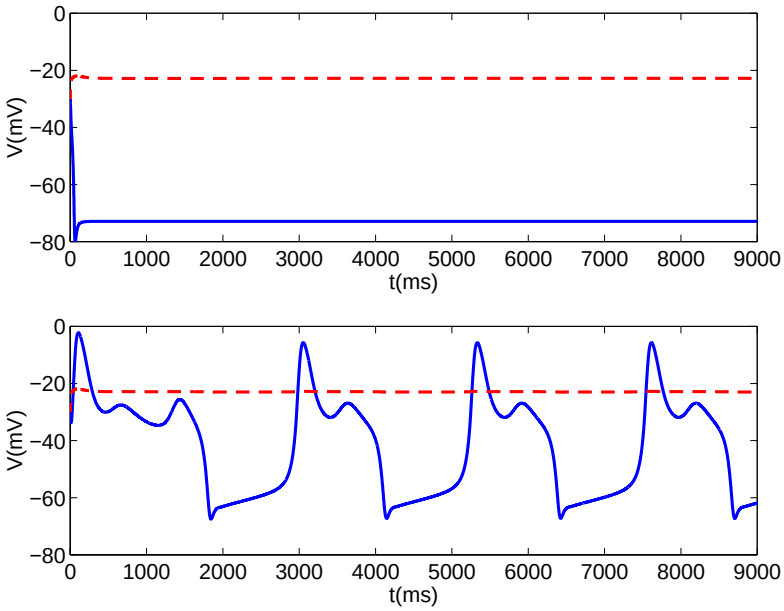

Figure 2.14: Luo-Rudy I Model. The upper graph shows the steady states for the system if uncoupled (i.e., $\chi\delta = 0$) with $K_o^+ = 60$ in the iscehmic region. The lower graph shows the system coupled with $\chi\delta = 0.005$, $K_o^+ = 60$mM and $m = 0.1$. The ischemic region remains at its RMP, while it acts as a source of current to force the normal region into oscillation.

The bifurcation diagrams for the LRI model dynamics are found numerically using Auto97 bifurcation software [6]. As shown in Figure 2.15, the oscillatory region remains largely unchanged when m in increased and even slightly increases before collapsing as $m \to 1$ (not shown).

2.7 Comparison with Experiments

To compare the oscillatory regions found from the LRI model quantitatively with experiments we translate experimental conductance parameters into model parameters. If an average cardiac cell has the dimensions 100 μm $\times$ 20 μm $\times$ 5 μm, then the average surface area for a cell is $5200\mu\text{m}^2$. If it is assumed that the only contact between neighboring cells occurs on the ends, then the intercellular surface area of contact, overestimating the entire intercellular surface to be gap junctional surface area, for typical cell dimensions is approximately 200μ m^2. This gives a χ value, ratio of gap junctional surface area to total membrane surface area, of about 0.04. Peters et al. [25] quantified the surface area covered by gap junctions per cell volume for normal human myocytes as 0.0051 $\mu\text{m}^2/\mu\text{m}^3$. Using the typical cardiac cell dimensions yields the experimentally determined $\chi \approx 0.01$, which is the same order as our previous overestimate.

Tan and Joyner [32] were unable to find oscillatory behavior when coupling a real ventricular cell to a passive model cell with an elevated (depolarized) resting membrane potential. They used a variety of coupling conductances (0nS, 3nS, 5nS) which correspond to $\chi\delta \approx$ (0,0.2,0.35) based on a resting membrane resistivity of $7 \times 10^3 \Omega\text{cm}^2$ and a total membrane area of $10^4\mu\text{m}^2$.

$$\begin{aligned}
\chi\delta &= \frac{\text{gap junction area}}{\text{total surface area}} \times \text{gap junctional conductance/area} \\
&\times \text{ resting membrane resistivity} \\
&= \frac{\text{gap junction conductance} \times \text{resting membrane resistivity}}{\text{total membrane area}}
\end{aligned}$$

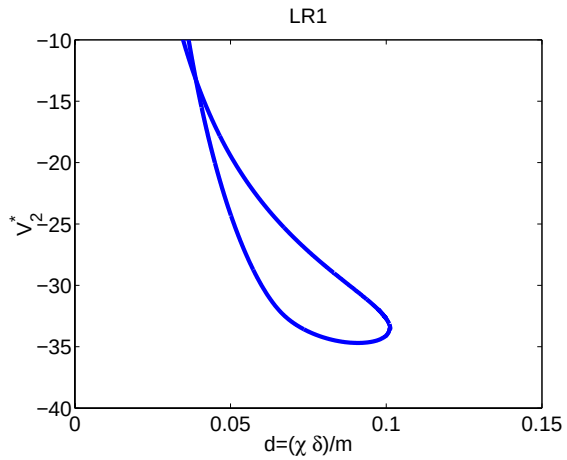

(a)

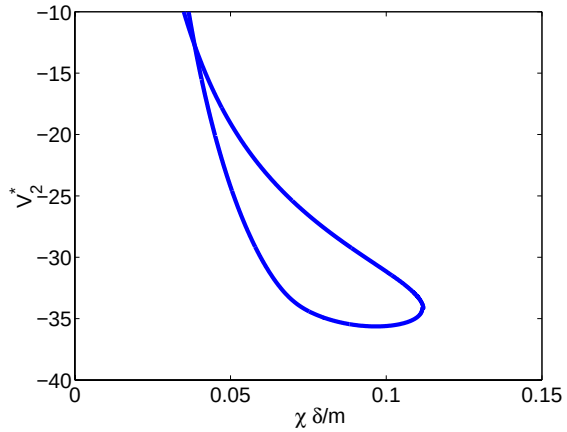

(b)

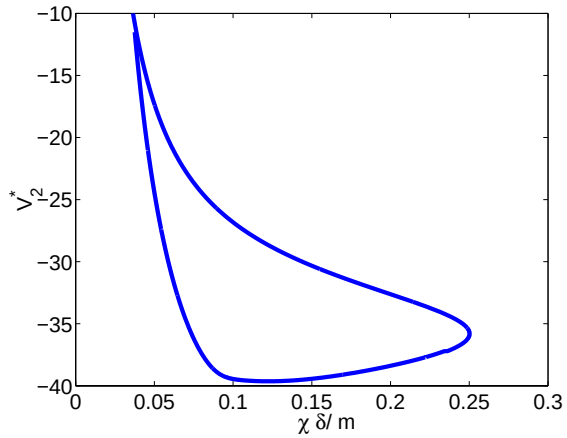

(c)

Figure 2.15: Luo-Rudy I Model. Unfolding diagrams for d vs. V_2^* at fixed m=0.1, m=0.5, m=0.9.

The coupled cells were of similar size which corresponds to $m \approx 0.5$. So the coupling conductances from [32] correspond to $\frac{\chi\delta}{m} \approx (0, 0.4, 0.7)$. The passive model cell RMPs used in [32] were (-20mV,-10,mV,0mV). In Figure 2.15 (b), the range of $\frac{\chi\delta}{m}$ with oscillatory behavior at $V_2^* = -20$mV is about $0.05 < \frac{\chi\delta}{m} < 0.06$ (coupling conductance between 0.36nS and 0.43nS) and nonexistent for $V_2^* = 0$mV or -10mV. Since the range for $V_2^* = -20$mV is small and at small conductances, it is reasonable to conclude that this region was not found in experiments.

The oscillations that are seen from the LRI model in Figure 2.14 are calcium induced action potentials, that is, the calcium current produces the upstroke of the action potential rather than the sodium current. We give an explanation for this in the Discussion. It seems reasonable then that enhancing the calcium handling with drugs as Kumar and Joyner [17] did would elicit calcium induced action potentials. The action of these drugs on the LRI model is not clear, but presumably they would act to expand the region of oscillation in $\frac{\chi\delta}{m}$ versus V_2^* space, due to enhanced excitability of the calcium mechanism. Further discussion of this in relation to the mechanism of the calcium upstroke is in the Discussion.

In the SAN experiment [34], the ability of the self-oscillatory SAN cell to drive a ventricular cell is dependent on both the coupling conductance as well as the size of the self-oscillatory cell. The ischemic cell in the MM model with $k = 20$ is self-oscillatory over a range of levels of ischemia. The parameter $1-m$ is a measure of the relative size of the ischemic cell, and $\chi\delta$ is a measure of the conductance between the ischemic cell and the normal cell. The control experiment with the SAN is correlated to this case.

If we let $p = 0.3$, then for small $1-m$ and $\chi\delta$ the oscillations from the ischemic cell persist but do not drive the normal cell beyond small subthreshold perturbations from its steady state. As $\chi\delta$ increases, there is a critical coupling conductance above which the ischemic cell ceases to oscillate. However, for intermediate $1-m$ ($0.06 < 1-m < 0.58$), as the coupling conductance increases there is again a critical conductance, but in this instance the ischemic cell goes from pacing without driving the normal cell to driving the normal cell into superthreshold action potentials.

Driving of the normal cell often appears in the form of a many to one (i.e., many ischemic action potentials to one normal action potential) response. Continuing to increase the coupling conductance we encounter a second critical conductance at which the ischemic cell pacing and normal cell oscillation are lost. These transitions between different dynamic regions in parameter space are shown in Figure 2.16 (a) and the boundaries of the regions agree qualitatively with the experiment of Wagner et al. [34] (see Figure 1.2). However, it is reasonable to expect a further division of dynamics for larger sizes of oscillator and stronger conductances. This is shown in Figure 2.16 (b).

For $0.28 < 1 - m < 0.58$ we encounter yet another critical conductance for sufficiently large coupling. Above this conductance value, the resting potential of the normal cell is superthreshold and the transmembrane potential of the normal cell is again oscillatory. For $1 - m$ sufficiently large ($1 - m > 0.58$), the critical conductance between pace and no drive and pace and drive region exists, but for conductances beyond that critical value the relative size of the oscillator is sufficient to force the normal cell to oscillate.

2.8 Interpretation of Different Limits for High p-Values

For high enough p-values, the steady state of the uncoupled ischemic cell stabilizes at a high transmembrane potential. We consider the strong coupling and weak coupling limiting cases with one large cell and one small cell for p in this sufficiently high range. Figure 2.17 is a visual representation of the these limits.

For m close to 1 with coupling $\frac{\chi\delta}{1-m} >> 1$ (i.e., the ischemic cell is relatively small and the coupling is strong), the singular limit $1 - m \to 0$ applies to (2.3) so that $V_2 = V_1$ for all time and each cell approaches the steady state of the normal cell, $(V^*(p_0), w^*(p_0))$.

For m close to 1 with coupling $\frac{\chi\delta}{1-m} \approx 1$, then $\frac{\chi\delta}{m} << 1$ so that the normal cell in (2.3) is effectively decoupled from the ischemic cell yielding $V_1 = V^*(p_0)$. Note that $\frac{\chi\delta}{1-m}V_1$ then acts like a fixed forcing term, an applied current, to the ischemic

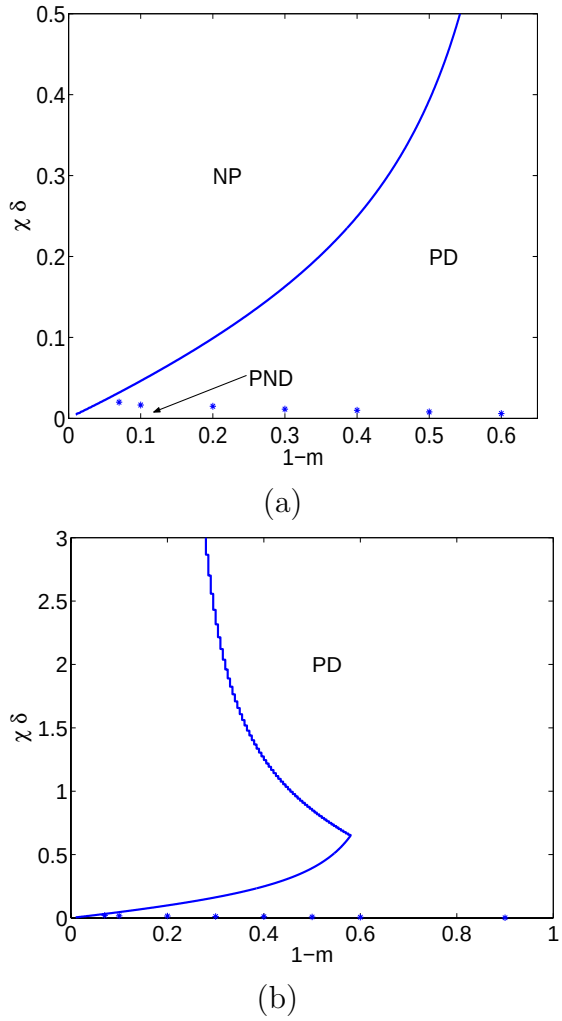

Figure 2.16: Regions of different dynamics of a coupled MM system with self-oscillatory ischemic cell in parameter space, conductance ($\chi\delta$) vs. relative size of ischemic cell ($1-m$). The ischemic cell follows MM dynamics with $p = 0.3$ and $k = 20$. The regions are where the ischemic cell paces but does not drive the normal cell (PND), the ischemic cell paces and drives the normal cell (PD), and the ischemic cell does not pace (NP). The stars are points on the boundary separating the PND and PD regions. (a) A restricted region of $\chi\delta$ vs. $1-m$ which qualitatively agrees with Figure 1.2. (b) An expanded region of $\chi\delta$ vs. $1-m$.

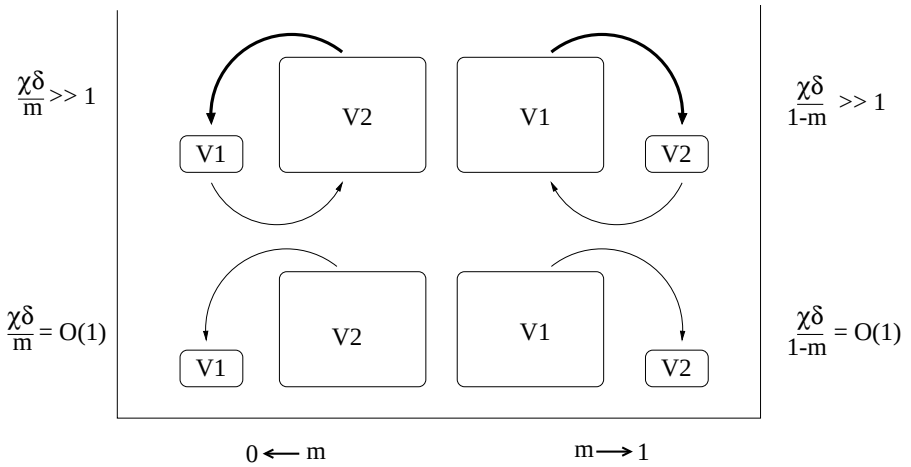

Figure 2.17: Four limits of the coupled equations (2.3). The strong coupling in the top two cell pairs forces the smaller cell to maintain the steady state potential of the larger cell. In the lower two cell pairs the coupling is weak such that the smaller cell has no influence on the larger cell but the larger cell induces a current on the smaller cell. The current is of consequence in the lower left cell pair since the smaller normal cell may be forced to oscillate. The direction and thickness of the arrows represent the direction and relative amplitude of current between each cell in each cell pair.

cell. Regardless of the dynamics of the ischemic cell, in this limit it has no effect on the normal cell.

For m close to 0 and $\frac{\chi\delta}{m} >> 1$ (i.e., the normal region is relatively small and the coupling is strong), the singular limit $m \to 0$ applies to (2.3) so that $V_2 = V_1$ for all time and each cell approaches the steady state of the ischemic cell, $(V^*(p), w^*(p))$.

For m close to 0 with the coupling $\frac{\chi\delta}{m} \approx 1$, $\frac{\chi\delta}{1-m} << 1$ so that in (2.3) the ischemic cell is effectively uncoupled from the normal cell yielding $V_2 = V^*(p)$. In this case $\frac{\chi\delta}{m}V_2$ acts like an applied current to the normal cell. Since in this limit the cells are effectively uncoupled, it is appropriate to examine the phase plane for the normal cell. The applied current, $I_{\text{app}} = \frac{\chi\delta}{m}V^*(p)$, along with the leak current, $-\frac{\chi\delta}{m}V_1$, act on a single cell to shift the V-nullcline in the phase plane as shown in Figure 2.18 for RHH dynamics. The shift in the V-nullcline of the normal cell for appropriate conductance destabilizes the steady state and the solution becomes oscillatory.

This observation leads us to consider a single cell forced by a leak current and a fixed applied current

$$\begin{aligned} \frac{dV}{dt} &= F(V, w, p) - dV + I_{app} \\ \frac{dw}{dt} &= g(V, w) \end{aligned} \tag{2.7}$$

and compare the behavior of this forced single cell to that of the coupled cell system with small $m \approx O(\chi\delta)$.

2.9 Small m Limit Theorem

In this section we state a theorem relating the forced oscillation of a single cell to oscillations of a coupled system.

Theorem 1 *Let $L^1(T^n)$ be the space of periodic functions on R^n of period T with bounded L^1 norm on $[0, T]$. Let $x, y \in L^1(T^n)$ and $H, G : L^1(T^n) \to L^1(T^n)$ be C^1 maps. Let $' \equiv \frac{d}{dt}$.*

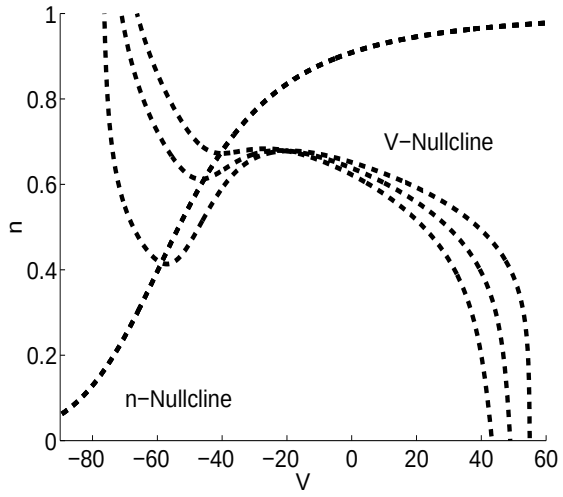

Figure 2.18: Change in normal cell V-nullcline. The lower knee on the V-nullcline shifts up for a fixed $V_2^* = -20$ as $\frac{\chi\delta}{m}$ increases.

Assumption (A1): Suppose

$$y' - H(y) = I - D_1 y$$

has a periodic solution, $Y(t)$, for some constant matrix $D_1 \in R^{n\times n}$ and constant vector $I \in R^n$.

Assumption (A2): Suppose

$$x' - G(x) = 0$$

has the steady state solution, x^*, such that $I = D_1 x^*$.

Then the coupled system

$$\begin{aligned} m_y(y' - H(y)) &= \delta_1(x - y) \\ m_x(x' - G(x)) &= \delta_2(y - x) \end{aligned} \tag{2.8}$$

has a periodic solution for $\frac{m_y}{m_x}$ sufficiently small with m_y and m_x scalars and matrices $\delta_i = m_y D_i$ for $i = 1, 2$.

Proof: To prove the theorem we appeal to the Lyapunov-Schmidt method. We look for periodic solutions $(y, x)^T \in L^1(T^n) \times L^1(T^n)$ to the equation

$$\widehat{F}\left(\begin{pmatrix} y \\ x \end{pmatrix}, \epsilon\right) = \begin{pmatrix} y \\ x \end{pmatrix}' - \begin{pmatrix} H(y) \\ G(x) \end{pmatrix} - \begin{bmatrix} D_1 & -D_1 \\ -\epsilon D_2 & \epsilon D_2 \end{bmatrix} \begin{pmatrix} y \\ x \end{pmatrix} = \begin{pmatrix} 0 \\ 0 \end{pmatrix}$$

with $\epsilon = \frac{m_y}{m_x}$. By assumption $\widehat{F}\left(\begin{pmatrix} Y \\ x^* \end{pmatrix}, 0\right) = 0$. We change variables

$$\begin{pmatrix} y \\ x \end{pmatrix} = \begin{pmatrix} Y \\ x^* \end{pmatrix} + \begin{pmatrix} y_1 \\ x_1 \end{pmatrix}$$

and let $\omega t = \tau$ where $\omega = 1 + \epsilon\omega_1$ to define the new function

$$F\left(\begin{pmatrix} y_1 \\ x_1 \end{pmatrix}, \epsilon\right) = (1 + \epsilon\omega_1) \begin{pmatrix} Y + y_1 \\ x^* + x_1 \end{pmatrix}' - \begin{pmatrix} H(Y + y_1) \\ G(x^* + x_1) \end{pmatrix}$$

$$- \quad \begin{bmatrix} D_1 & -D_1 \\ -\epsilon D_2 & \epsilon D_2 \end{bmatrix} \begin{pmatrix} Y + y_1 \\ x^* + x_1 \end{pmatrix} \tag{2.9}$$

so that

$$F\left(\begin{pmatrix} 0 \\ 0 \end{pmatrix}, 0\right) = 0.$$

Since H, G are C^1 maps, we can write a Taylor series for $(H(Y+y_1), G(x^*+x_1))^T$.

$$\begin{pmatrix} H(Y+y_1) \\ G(x^*+x_1) \end{pmatrix} = \begin{pmatrix} H(Y) \\ G(x^*) \end{pmatrix} + \begin{bmatrix} H'(Y) & 0 \\ 0 & G'(x^*) \end{bmatrix} \begin{pmatrix} y_1 \\ x_1 \end{pmatrix} + R\left(\begin{pmatrix} y_1 \\ x_1 \end{pmatrix}\right)$$

where G' and H' are the Jacobians of G and H, respectively, and $R\left(\begin{pmatrix} y_1 \\ x_1 \end{pmatrix}\right) = o(||(y_1, x_1)^T||)$. Substituting this expansion into (2.9) yields

$$\begin{aligned} F\left(\begin{pmatrix} y_1 \\ x_1 \end{pmatrix}, \epsilon\right) &= \begin{pmatrix} Y \\ x^* \end{pmatrix}' - \begin{pmatrix} H(Y) \\ G(x^*) \end{pmatrix} - \begin{bmatrix} D_1 & -D_1 \\ 0 & 0 \end{bmatrix} \begin{pmatrix} Y \\ x^* \end{pmatrix} \\ &+ \begin{pmatrix} y_1 \\ x_1 \end{pmatrix}' - \begin{bmatrix} H'(Y) + D_1 & -D_1 \\ 0 & G'(x^*) \end{bmatrix} \begin{pmatrix} y_1 \\ x_1 \end{pmatrix} \\ &+ \epsilon\left(\omega_1 \begin{pmatrix} Y + y_1 \\ x^* + x_1 \end{pmatrix}' + \begin{bmatrix} 0 & 0 \\ -D_2 & D_2 \end{bmatrix} \begin{pmatrix} Y + y_1 \\ x^* + x_1 \end{pmatrix}\right) \\ &+ R\left(\begin{pmatrix} y_1 \\ x_1 \end{pmatrix}\right). \end{aligned} \tag{2.10}$$

The first three terms combine to be 0, and defining the linear operator

$$L\begin{pmatrix} y_1 \\ x_1 \end{pmatrix} = \begin{pmatrix} y_1 \\ x_1 \end{pmatrix}' - \begin{bmatrix} H'(Y) + D_1 & -D_1 \\ 0 & G'(x^*) \end{bmatrix} \begin{pmatrix} y_1 \\ x_1 \end{pmatrix}$$

allows us to rewrite (2.10) as

$$\begin{aligned} F\left(\begin{pmatrix} y_1 \\ x_1 \end{pmatrix}, \epsilon\right) &= L\begin{pmatrix} y_1 \\ x_1 \end{pmatrix} \\ &+ \epsilon\left(\omega_1 \begin{pmatrix} Y + y_1 \\ x^* + x_1 \end{pmatrix}' + \begin{bmatrix} 0 & 0 \\ -D_2 & D_2 \end{bmatrix} \begin{pmatrix} Y + y_1 \\ x^* + x_1 \end{pmatrix}\right) \\ &+ R\left(\begin{pmatrix} y_1 \\ x_1 \end{pmatrix}\right). \end{aligned} \tag{2.11}$$

The linear operator L has a one-dimensional nullspace spanned by $(Y', 0)$. This can be seen by taking the time derivative of $\widehat{F}\left(\begin{pmatrix} Y \\ x^* \end{pmatrix}, 0\right)$. We get this nullspace from

the shift invariance of the stable periodic solution. In general, let $(\xi_1, \xi_2)^T \in N(L)$ and $(\xi_{1c}, \xi_{2c})^T \in N_c(L)$, the complement to $N(L)$, so that $(y_1, x_1)^T = (\xi_1, \xi_2)^T + (\xi_{1c}, \xi_{2c})^T$. Substituting into (2.11) we define a new function

$$\begin{aligned} \Phi\left(\begin{pmatrix} \xi_1 \\ \xi_2 \end{pmatrix}, \begin{pmatrix} \xi_{1c} \\ \xi_{2c} \end{pmatrix}, \epsilon\right) &= L\begin{pmatrix} \xi_{1c} \\ \xi_{2c} \end{pmatrix} \\ &+ \epsilon\omega_1 \begin{pmatrix} Y + \xi_1 + \xi_{1c} \\ x^* + \xi_2 + \xi_{2c} \end{pmatrix}' \\ &+ \epsilon \begin{bmatrix} 0 & 0 \\ -D_2 & D_2 \end{bmatrix} \begin{pmatrix} Y + \xi_1 + \xi_{1c} \\ x^* + \xi_2 + \xi_{2c} \end{pmatrix} \\ &+ R\left(\begin{pmatrix} \xi_1 + \xi_{1c} \\ \xi_2 + \xi_{2c} \end{pmatrix}\right). \end{aligned} \tag{2.12}$$

Now using the inner product

$$< (u_1, u_2)^T, (v_1, v_2)^T >= \int_0^T u_1 v_1 + u_2 v_2 \, dt$$

we project Φ onto the nullspace of the adjoint of L, $N(L^*)$, to get $< \Phi, (v_1, v_2)^T > (v_1, v_2)^T$ where $(v_1, v_2)^T \in N(L^*)$. We then subtract it from Φ to get

$$\Phi\left(\begin{pmatrix} \xi_1 \\ \xi_2 \end{pmatrix}, \begin{pmatrix} \xi_{1c} \\ \xi_{2c} \end{pmatrix}, \epsilon\right) - \left\langle \Phi\left(\begin{pmatrix} \xi_1 \\ \xi_2 \end{pmatrix}, \begin{pmatrix} \xi_{1c} \\ \xi_{2c} \end{pmatrix}, \epsilon\right), \begin{pmatrix} v_1 \\ v_2 \end{pmatrix} \right\rangle \begin{pmatrix} v_1 \\ v_2 \end{pmatrix}$$

which lies in the range of L, $R(L)$. However, to leave Φ unchanged by this subtraction we require that $< \Phi, (v_1, v_2)^T >= 0$. Using the definition of Φ in (2.12) we can solve this orthogonality condition for ω_1 to get

$$\omega_1 = \frac{\epsilon \left\langle \begin{bmatrix} 0 & 0 \\ -D_2 & D_2 \end{bmatrix} \begin{pmatrix} Y + \xi_1 + \xi_{1c} \\ x^* + \xi_2 + \xi_{2c} \end{pmatrix}, \begin{pmatrix} v_1 \\ v_2 \end{pmatrix} \right\rangle + \left\langle R\left(\begin{pmatrix} \xi_1 + \xi_{1c} \\ \xi_2 + \xi_{2c} \end{pmatrix}\right), \begin{pmatrix} v_1 \\ v_2 \end{pmatrix} \right\rangle}{\left\langle \begin{pmatrix} Y + \xi_1 + \xi_{1c} \\ x^* + \xi_2 + \xi_{2c} \end{pmatrix}', \begin{pmatrix} v_1 \\ v_2 \end{pmatrix} \right\rangle}.$$

as long the denominator is nonzero. The eigenfunctions of L and the eigenfunctions of L^* form a biorthogonal set [23]. Since $(Y', 0)^T$ is an eigenfunction of L with respect to the zero eigenvalue and $(v_1, v_2)^T$ is an eigenfunction of L^* with respect to the zero eigenvalue, $< (Y', 0)^T, (v_1, v_2)^T >\neq 0$.

To look for solutions that have no additional terms in the nullspace of L (i.e., $(\xi_1, \xi_2)^T = (0, 0)^T$) we define the function

$$\widehat{\Phi}\left(\begin{pmatrix}\xi_{1c}\\ \xi_{2c}\end{pmatrix}, \omega_1, \epsilon\right) =$$

$$\begin{pmatrix} \Phi\left(\begin{pmatrix}0\\0\end{pmatrix}, \begin{pmatrix}\xi_{1c}\\ \xi_{2c}\end{pmatrix}, \epsilon\right) - \left\langle \Phi\left(\begin{pmatrix}0\\0\end{pmatrix}, \begin{pmatrix}\xi_{1c}\\ \xi_{2c}\end{pmatrix}, \epsilon\right), \begin{pmatrix}v_1\\ v_2\end{pmatrix}\right\rangle \begin{pmatrix}v_1\\ v_2\end{pmatrix} \\ \omega_1 - \dfrac{{}^{\epsilon}\left\langle \begin{bmatrix}0 & 0\\ -D_2 & D_2\end{bmatrix}\begin{pmatrix}Y+\xi_{1c}\\ x^*+\xi_{2c}\end{pmatrix}, \begin{pmatrix}v_1\\ v_2\end{pmatrix}\right\rangle + \left\langle {}^{R}\left(\begin{pmatrix}\xi_{1c}\\ \xi_{2c}\end{pmatrix}\right), \begin{pmatrix}v_1\\ v_2\end{pmatrix}\right\rangle}{\left\langle \begin{pmatrix}Y+\xi_{1c}\\ x^*+\xi_{2c}\end{pmatrix}', \begin{pmatrix}v_1\\ v_2\end{pmatrix}\right\rangle} \end{pmatrix}$$

Since,

$$\widehat{\Phi}\left(\begin{pmatrix}0\\0\end{pmatrix}, 0, 0\right) = 0$$

and the derivative

$$\frac{\partial}{\partial(\xi_{1c}, \xi_{2c}, \omega_1)^T}\widehat{\Phi}\left(\begin{pmatrix}0\\0\end{pmatrix}, 0, 0\right)\begin{pmatrix}\begin{pmatrix}\xi_{1c}\\ \xi_{2c}\end{pmatrix}\\ \omega_1\end{pmatrix} = \begin{bmatrix}L & 0\\ 0 & 1\end{bmatrix}\begin{pmatrix}\begin{pmatrix}\xi_{1c}\\ \xi_{2c}\end{pmatrix}\\ \omega_1\end{pmatrix}$$

is invertible, we apply the Implicit Function Theorem to $\widehat{\Phi}$ and conclude that there exists a unique function $h = (h_1, h_2, h_3)^T$ such that

$$\begin{pmatrix}\xi_{1c}\\ \xi_{2c}\\ \omega_1\end{pmatrix} = h(\epsilon)$$

for all ϵ sufficiently small. □

Now we relate the Theorem 1 to the coupled system (2.3). Let $y = (V_1, \mathbf{w}_1)^T$ and $x = (V_2, \mathbf{w}_2)^T$ with $H(y) = (F(y, \mathbf{p}_0), g(y))^T$ and $G(x) = (F(x, \mathbf{p}), g(x))^T$. Also let D_1, D_2, and M each be such that $D_1^{1,1} = d = \frac{\chi\delta}{m}, D_1^{i,j} = 0$ otherwise, $D_2^{1,1} = \frac{\chi\delta}{1-m}, D_2^{i,j} = 0$ otherwise, and $M_{1,1} = 1, M_{i,j} = 0$ otherwise. This implies there is only coupling in the transmembrane potential equation.

Assumption (A1): The system

$$\begin{aligned} \frac{dV_1}{dt} - F(V_1, \mathbf{w}_1, \mathbf{p}_0) &= -dV_1 + I_{\text{app}} \\ \frac{d\mathbf{w}_1}{dt} &= g(V_1, \mathbf{w}_1) \end{aligned} \tag{2.13}$$

exhibits oscillations in transmembrane potential for some d and some I_{app}.

Assumption (A2): The system

$$\begin{aligned} \frac{dV_2}{dt} - F(V_2, \mathbf{w}_2, \mathbf{p}) &= 0 \\ \frac{d\mathbf{w}_2}{dt} &= g(V_2, \mathbf{w}_2) \end{aligned} \tag{2.14}$$

has a steady state $(V_2^*(\mathbf{p}), \mathbf{w}_2^*(\mathbf{p}))$ such that $dV_2^*(\mathbf{p}) = I_{\text{app}}$.

Then the coupled system

$$\begin{aligned} m\left(\frac{dV_1}{dt} - F(V_1, \mathbf{w}_1, \mathbf{p_0})\right) &= \chi\delta(V_2 - V_1) \\ \frac{d\mathbf{w}_1}{dt} &= g(V_1, \mathbf{w}_1) \\ (1-m)\left(\frac{dV_2}{dt} - F(V_2, \mathbf{w}_2, \hat{\mathbf{p}})\right) &= \chi\delta(V_1 - V_2) \\ \frac{d\mathbf{w}_2}{dt} &= g(V_2, \mathbf{w}_2) \end{aligned} \tag{2.15}$$

for $\frac{\chi\delta}{m} = d$ exhibits oscillations in transmembrane potential provided $\frac{m}{1-m}$ is sufficiently small. If $V_2^*(p)$ increases as p increases without bound and $dV_2^*(p_0) \leq I_{\text{app}}$, then there must exist such a p at which $dV_2^*(p) = I_{\text{app}}$.

In words, if applying a constant current and leak current with fixed leak conductance forces a normal cell into large scale oscillations, and if a second cell has a depolarized steady state transmembrane potential in the appropriate range, then the depolarized cell induces large scale oscillations in the normal cell. This occurs for an appropriate range of coupling conductances provided the normal cell is sufficiently small relative to the ischemic cell.

We now wish to verify that the theorem applies to the three models described earlier. To verify the two assumptions, A1 and A2, of Theorem 1, we consider the unfolding diagrams in the parameters I_{app} and d and unfolding diagrams in the parameters $V_2^* = I_{\text{app}}/d$ and d for the three sets of ionics. Figure 2.19 (a) shows that a single cell with RHH dynamics has oscillations for an open region in d versus I_{app} satisfying A1. Figure 2.19 (b) shows where d versus $V_2^* = I_{app}/d$ yields oscillations so that if the RHH steady state of (2.14) is located in the shaded region, A2 is satisfied. From Figure 2.3 we see there is a range of p-values with V_2^*

in the shaded region for which Theorem 1 applies in which oscillations exist in the coupled system (2.15).

Similarly, for LRI dynamics, Figure (2.20) (a) shows an open region in d versus I_{app} where oscillations satisfying A1 occur. Figure (2.20) (b) shows where d versus $V_2^* = I_{app}/d$ yields oscillations so that if the LRI steady state of (2.14) is located in the shaded region, A2 is satisfied. Figure 2.13 shows a range of p-values for which V_2^* is in the shaded region of Figure 2.20 b).

The single cell MM model has oscillations when the applied current, I_{app}, forces the piecewise cubic V-nullcline adjusted by the leak term, $F(V, w, p_0) - dV$, to shift vertically so that the steady state is on the middle branch. In steady state, $w = \frac{1}{\gamma}V^*$, and for V^* to be on the middle branch, it must satisfy

$$0 = V^* - a - \frac{1}{\gamma}V^* - dV^* + I_{\text{app}}$$

for $\frac{a}{2} < V^* < \frac{1+a}{2}$ so that the range of I_{app} which forces V^* on the middle branch and the system to oscillate is (I^-, I^+) where

$$I^- = \frac{a}{2}\left(1 + d + \frac{1}{\gamma}\right), \tag{2.16}$$

$$I^+ = \left(\frac{1}{2} + \frac{a}{2}\right)\left(1 + d + \frac{1}{\gamma}\right) - 1 \tag{2.17}$$

As well, for an eigenvalue of the single system to have positive real part, d must remain below $1 - \epsilon\gamma$. For $1 - \epsilon\gamma < d < 1$, the autocatalytic dynamics in the transmembrane equation are balanced and stabilized by the recovery dynamics, while for $1 < d$ the term $F(V, 0) - dV$ loses its triphasic nature all together and becomes a monotonically decreasing function of V. Figure 2.21 (a) shows the region in d versus I_{app} parameter space where a forced single MM model cell oscillates. This picture gives an indication of approximate independence of the two mechanisms involved in the instability of the coupled MM system.

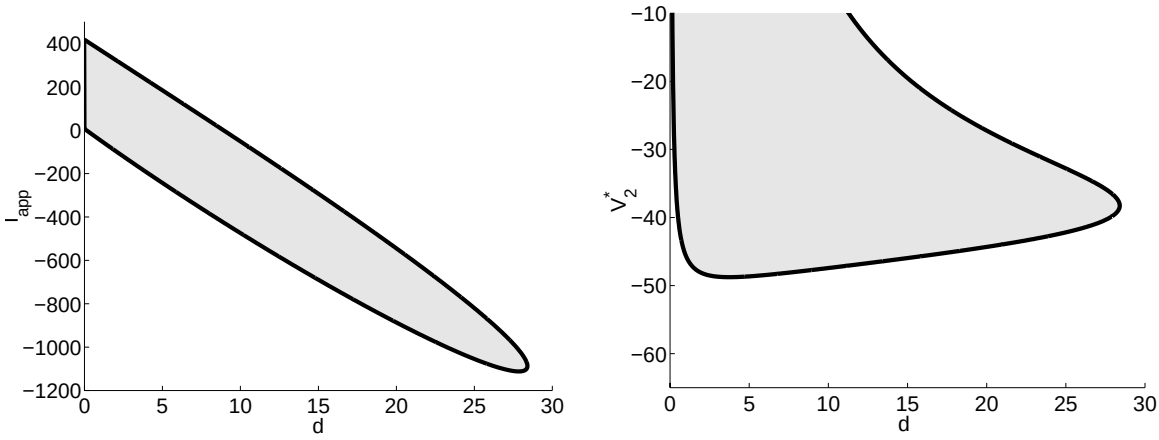

(a) (b)

Figure 2.19: Unfolding diagram for the RHH single cell. (a) The Hopf bifurcation curve for the single RHH cell with changes in applied current, $I_{\mathbf{app}}$, and leak conductance, d. (b) The Hopf bifurcation diagram for the Single RHH cell with changes in fixed potential, V_2^*, and the leak conductance. Subfigure (b) is obtained by plotting d versus $V_2^* = I_{\mathbf{app}}/d$. The shaded regions are parameter regions with oscillatory dynamics.

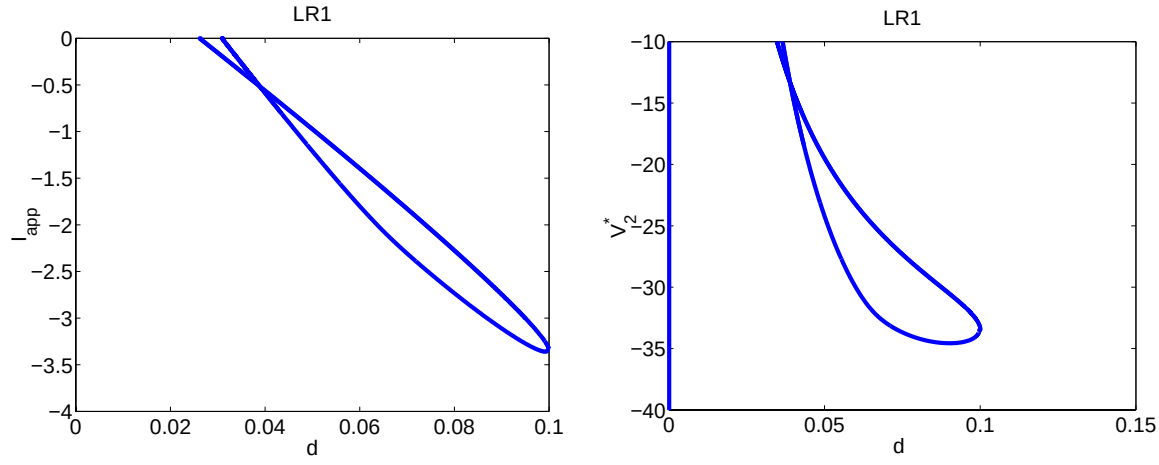

(a) (b)

Figure 2.20: Unfolding diagram for the LRI single cell. (a) d vs. $I_{\mathbf{app}}$ for the LRI model. Inside the closed region the system is oscillatory. (b) d vs. $V_2^* = I_{\mathbf{app}}/d$

One aspect is the movement of the steady state to the middle branch of the vertically shifted V-nullcline by the applied current. The other is the loss of positive slope of the V-nullcline for sufficiently high d-values. Stability of the system is regained for d large enough independent of I_{app}, while the upper and lower limits of applied current for oscillation, I^+ and I^-, respectively depend on d only linearly with small slope. This shows that there is an open region region in d versus I_{app} parameter space which satisfies A1 of Theorem 1.

In Figure 2.21, we let $I_{\text{app}} = dV_2^*$ and treat V_2^* as a variable parameter.

The MM model is oscillatory in the region

$$I^- < dV_2^* < I^+$$

so that the upper bound on V_2^* as a function of d is $\frac{1}{d}I^+$ (which does not affect the oscillatory region for MM model parameters) and the lower bound is $\frac{1}{d}I^-$. We translate these bound into the related p-values using (2.6) with the lower p bound as

$$p_l = \frac{k(1-1/\gamma)I^-/d - ak}{(2-k-ka) - I^-/d(2-2k+2(1/\gamma))}$$

and the upper p bound as

$$p_u = \frac{k(1-1/\gamma)I^+/d - ak}{(2-k-ka) - I^+/d(2-2k+2(1/\gamma))}.$$

2.10 Single to Coupled Bifurcation Diagrams

For sufficiently small m the coupled system should behave similarly to the single cell under appropriate forcing. In Figure 2.22, we compare the single cell bifurcation diagram of Figure 2.19 (b) with the bifurcation diagram for the coupled cells from Figure 2.5 (a). There are two mechanisms by which the coupled cells may become unstable. The first has already been described as a forcing on a normal cell. The second mechanism is from the self-oscillation of the ischemic cell which may occur upon elevation of p. The dashed lines in Figure 2.22 (a), also denoted by the Hopf bifurcation squares in Figure 2.3 (b), are those transmembrane potentials between which the ischemic cell oscillates when uncoupled from the normal cell. The oscillatory regions in Figure 2.22 (a) and (b) are remarkably similar, as expected.

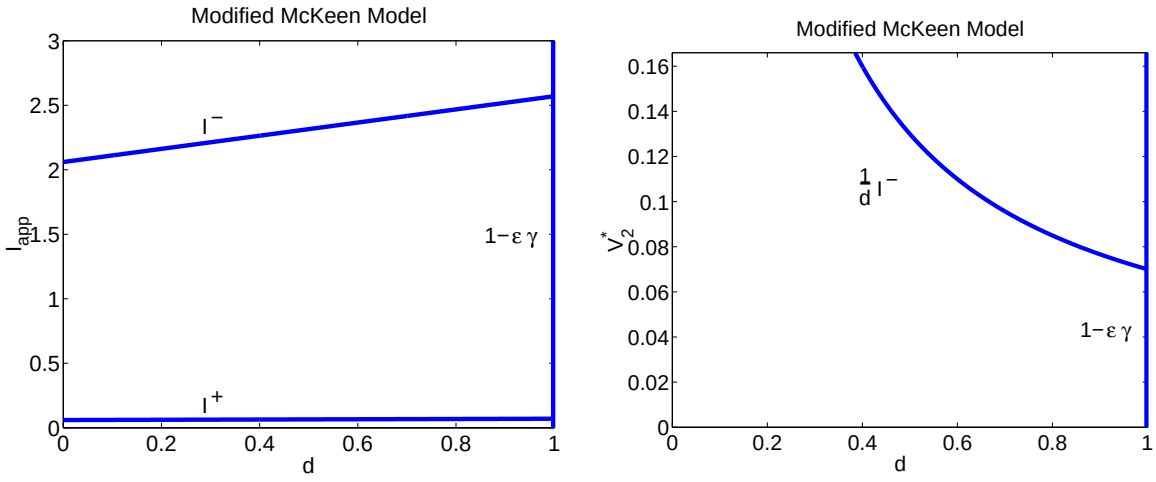

(a) (b)

Figure 2.21: Unfolding diagram for the MM single cell. (a) The region between the upper and lower lines, the $I_{\mathbf{app}}$ axis, and the $d = 1 - \epsilon\gamma$ line is where the dynamics are oscillatory. The bounds are calculated in the text. (b) The dynamics in the parameter region above the curve and left of the $\frac{\chi\delta}{m} = 1 - \epsilon\gamma$ line are oscillatory.

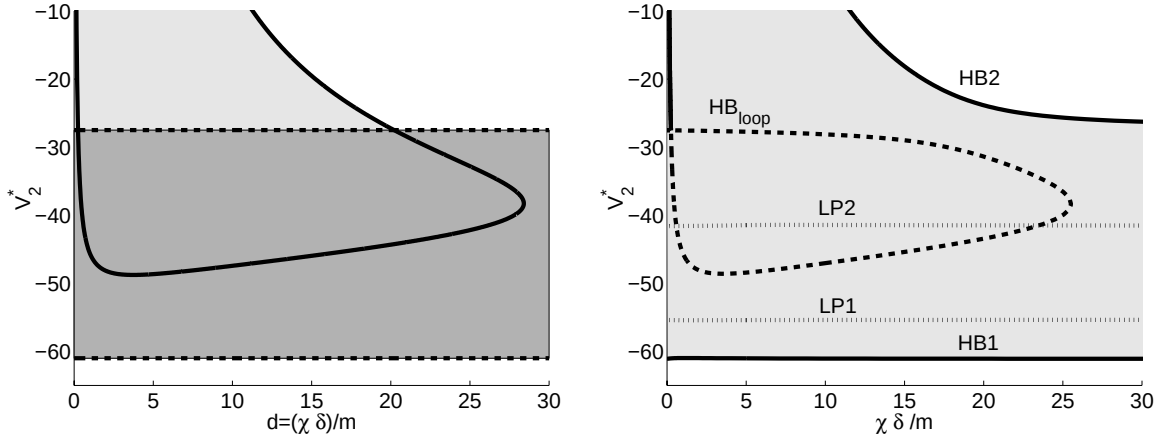

(a) (b)

Figure 2.22: Comparison between the oscillatory region of a single cell and that of the coupled system. (a) The single cell bifurcation diagram as in Figure 2.19 (b) but with dashed lines added. The ischemic cell is self-oscillatory when its rest potential lies between the dashed lines. (See text.) (b) The coupled cell bifurcation diagram as in Figure 2.5 (a).

The MM model with $k = 20$ in Figure 2.23 (a) and (c) exhibits similar behavior to the RHH model. Because of the loss of stability of the steady state in the single system under changes in p, there, again, are two mechanisms for oscillation in the coupled systems. The oscillatory region found from the single system matches well with the coupled systems, only with a slight downward slope of the top line differentiating the two pictures for $\frac{\chi\delta}{m} < 1 - \epsilon\gamma$. In Figure 2.12 we see an extended $\frac{\chi\delta}{m}$-axis. For the MM model with $k = 6$ in Figure 2.23 (b) and (d), we see an excellent correspondence between the theoretical curve and the coupled systems curve for $\frac{\chi\delta}{m} < 1 - \epsilon\gamma$.

It is clear when comparing the two columns of Figure 2.23 which part of the oscillatory region for $k = 6$ (right column) is due to the self-oscillation and which part is due to the coupling of regions at different resting potentials. Since Figure 2.23 (d) has a region in parameter space that yields oscillations, it is clear that an individual cell need not oscillate under increases in p to yield coupled cell oscillations. This implies that the mechanism for coupled cell oscillations for this model and small m relies primarily upon how the individual cell responds to an applied current combined with a leak current rather than its dependence on changes in p.

As shown in Figure 2.24 for the LRI model, there is an almost exact correspondence between the curve derived from the single system in Figure 2.24 (a) and the curve obtained with the coupled systems and small m ($m = 0.1$) in Figure 2.24 (b). These results reaffirm the validity of Theorem 1.

2.11 Discussion

We have shown that excitable cells oscillate for certain ranges of applied and leak currents, but the morphology of the oscillations in the LRI model is distinct from those induced by a periodic current stimulus. This difference in morphology stems from the suppression of the inward sodium current in the fixed applied current situation so that the action potentials are driven only by the inward calcium current.

The fact that the oscillations in the coupled cell LRI model are driven by calcium

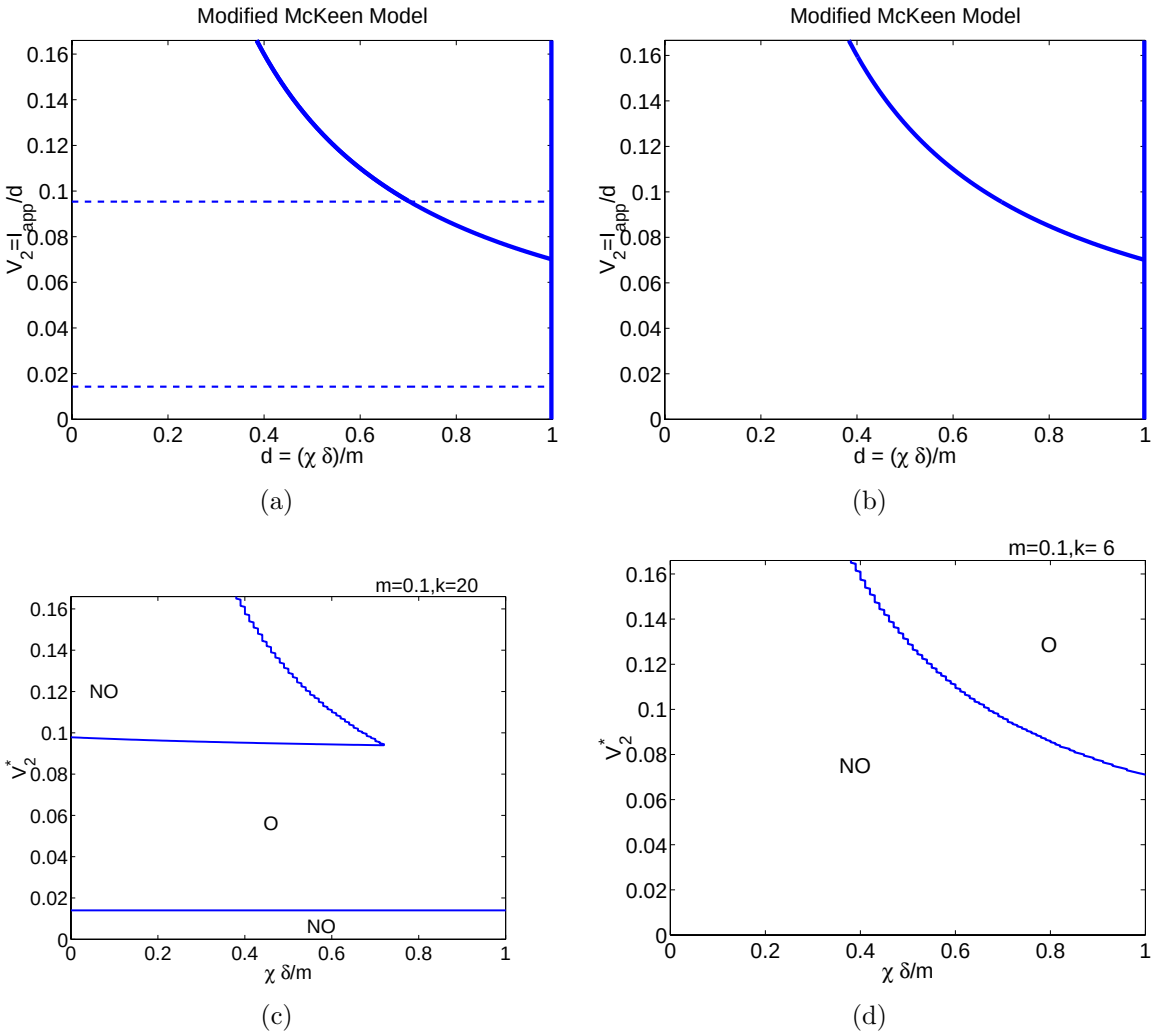

Figure 2.23: Comparison between the region of oscillation based on the applied and leak currents and the coupled systems with $m = 0.1$ in the MM model. (a) k = 20. The solid line is the lower bound on V_2^* from above for oscillations. The upper and lower dashed lines are at the V_2^*-values between which region 2 is self-oscillatory (for all $0 < \frac{\chi\delta}{m} < 1 - \epsilon\gamma$). (b)k = 6. The solid line is the lower bound on p from above for oscillations. (c) The coupled systems with $k = 20$. (d) The coupled systems with $k = 6$.

comes from the steady state gating dependence on the transmembrane potential. In Figure 2.25 the infinity curves for m, h, d and f are plotted. At the normal steady state, the m gate is closed, while the h gate is open. Following a stimulus that suddenly raises the transmembrane potential, the m gate rapidly opens with time constant τ_m while the h gate begins to slowly close with a time constant τ_h. Early in the action potential the h gate closes shutting off the sodium current. As the transmembrane potential begins to rise from the sodium current, the potassium and calcium gates are opened on a slower time scale. The d activation gate of the calcium channel begins to slowly open, while the f inactivation gate closes even more slowly, allowing a calcium current. Gate responses of potassium channels are activated and potassium flows out of the cell in an outward current. The slow change in the balance between the inward calcium current and outward potassium current makes up the rest of the action potential in the LRI model. Finally, the transmembrane potential returns to rest where the gates reset.

However, under the conditions studied here with a normal cell coupled to a cell with elevated resting transmembrane potential, the dynamics of the normal gates are altered. The resting transmembrane potential is slowly raised in the normal cell due to coupling. If the resting transmembrane potential of the normal cell is raised above -55mV, then the sodium current is never triggered, because the h gate is never reset. On the other hand, the calcium curves, d_∞ and f_∞, are shifted and provide a window where both gates are open for a region of V. For the oscillation shown in Figure 2.14, the rest potential of the normal cell is raised to about -55mV closing the h gate while the m gate remains closed, but at the same time the d gate is opened while the f gate is also open, which activates the calcium current. This is the calcium current that causes the autocatalytic increase in V.

In the RHH model the m_∞ and h_∞ curves are as shown in Figure 2.26. Since h_∞ is approximated by $0.85 - n_\infty$, the h_∞ curve does not asymptote to 1 or 0 as Vgets large negative or large positive, respectively. However, it is clear that there is a substantial window where both m and h are activated. This leads to a sufficient sodium current to achieve threshold and allow for an oscillatory action potential.

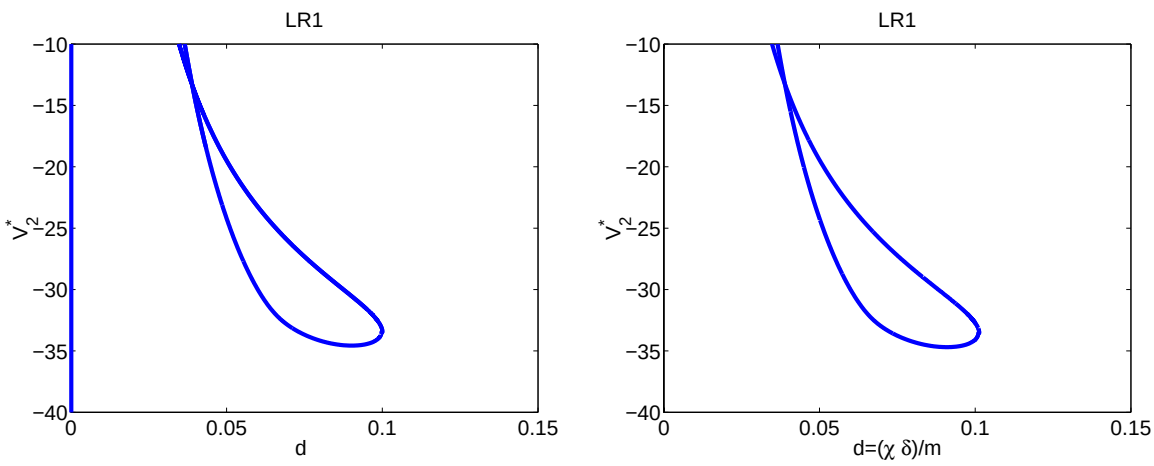

(a) (b)

Figure 2.24: Comparison between the region of oscillation based on the applied and leak currents and the coupled system with $m = 0.1$ in the LRI model. (a) The forced single cell oscillatory region. (b) The coupled system oscillatory region.

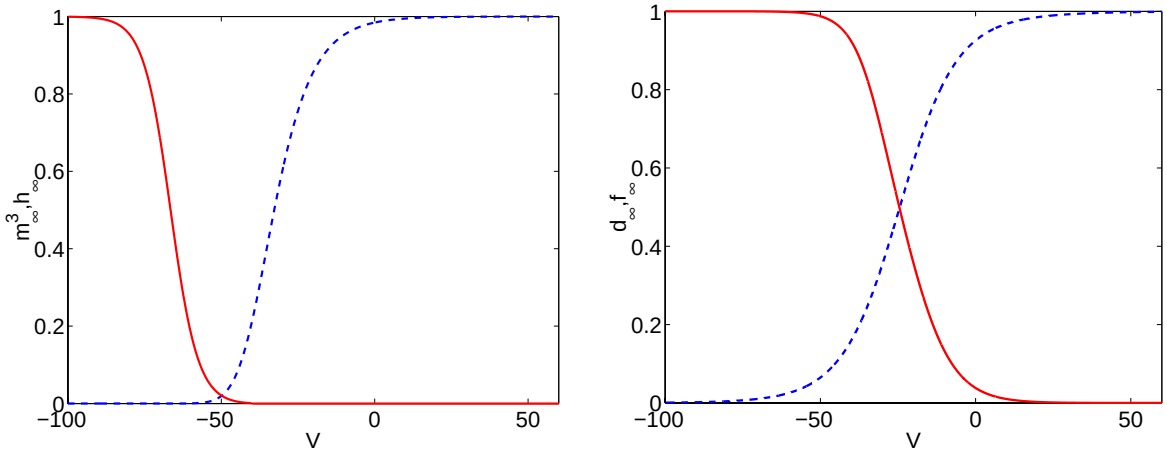

Figure 2.25: Infinity gating curves. (a) h_∞ is the solid curve, while m_∞ is the dashed curve. The j gate has an infinity curve which lies almost exactly on the h_∞ curve. (b) f_∞ is the solid curve, while d_∞ is the dashed curve.

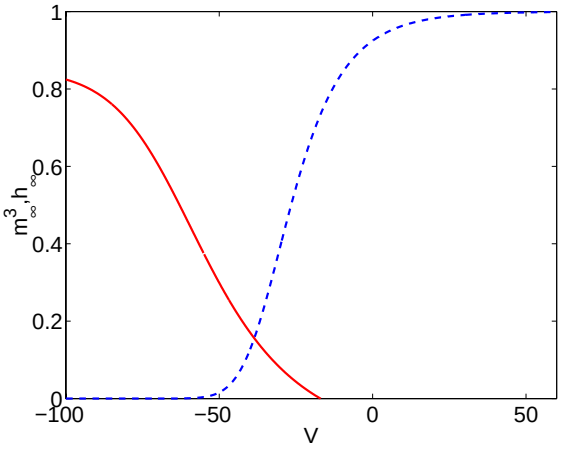

Figure 2.26: The infinity curves for RHH model. h_∞ is the solid curve, while m_∞ is the dashed curve.

The LRI model does not have a sodium based upstroke at high resting membrane potentials, but does allow for calcium to play that role, while the RHH model has sodium upstrokes at higher resting potentials. It is not clear that these represent actual differences between cardiac cells and neural cells or are merely differing features of the models.

The enhancement of the calcium handling in the experiments of Kumar and Joyner [16] may change the position of the gating curves. If the drugs were to shift the calcium window to more negative potentials, the threshold needed to excite a LRI cell through a calcium current would be reduced. If the d_∞ curve were shifted alone to more negative potentials, then not only would the cell be more excitable, but also the calcium current would be larger. There is also the possibility that the sodium gating curves are slightly affected. Even a slight increase in sodium current window size could trigger a sodium upstroke rather than one induced only by calcium or assist calcium in the upstroke. Since the LRI model does not incorporate physiological mechanisms in the gating equations, the effect of the drugs cannot be modeled in this system to verify which if any of the above mechanisms are valid for the coupled system.

2.12 Conclusion

A simple modification to the RHH model recreates several features of ischemic tissue such as elevated transmembrane potential and shorter action potential duration. We couple an ischemic cell following this type of ischemic modification to a normal cell in three separate systems of ionics. We show that in all three systems of ionics there is an open region in degree of ischemia versus coupling conductance parameter space in which the normal cell oscillates. There exist parameter regions in which coupled ischemic and normal cells oscillate, but when these cells are uncoupled, they are individually stable. The ischemic cell while uncoupled maintains an elevated, stable, inexcitable resting potential. The normal cell is stable and excitable. We compare the coupled cell results to experiment and show that the models may assist in locating previously unobserved oscillatory behavior. As well, dynamics previously unreported for model SAN coupled to a normal ventricular cell were located in coupling conductance versus size of oscillator parameter space for an ischemic oscillator coupled to a normal cell.

If an ischemic cell is large relative to a normal cell, there is little feedback from the normal cell to the ischemic cell. The normal cell reacts as a forced single cell with the forcing in the form of an applied constant current and a leak current. This observation leads to the small m limit theorem. This theorem is for general ionic forms though the three sets of ionics we study here satisfy the theorem. Even though the most physiological model yielded oscillatory behavior in certain parameter regions, the nature of the oscillations was interesting. We briefly explain why the upstroke of the LRI action potential was due to calcium when forced by an applied current with a leak current present or while coupled to a depolarized ischemic cell.

CHAPTER 3

ONE-DIMENSIONAL SPATIAL MODEL

3.1 Introduction

Experiments with strips of tissue described in the introductory chapter show oscillations when part of the tissue is exposed to ischemic like conditions while coupled to normal tissue. The experiments show that spontaneous oscillations emerge from the border between ischemic and normal tissue, the border zone. In this chapter we study a one-dimensional spatial model of an ischemic border zone, and model the strip of tissue experiments using piecewise linear modified McKean (MM) dynamics described in Section 2.5. MM dynamics are utilized for analytical calculation. Existence of a steady state solution is shown for the MM dynamics using a phase plane argument, while a super and subsolution argument is used to prove existence and uniqueness of the steady state solution for more general dynamics. Linear stability analysis is performed. Regions in parameter space where the steady state solution is unstable are described in bifurcation diagrams. We give a qualitative comparison of these results with the Picard experiment [26].

3.2 PDE Model

From cable theory [15] we write down a partial differential equation model for an excitable medium in one spatial dimension as

$$P_m\left(C_m\frac{\partial V}{\partial t}+I_{ion}(V,\mathbf{w})\right)=\frac{\partial}{\partial x}\left(\frac{1}{r_i(x)+r_e(x)}\frac{\partial V}{\partial x}\right),$$

with separate equations for the recovery variables, $\mathbf{w}$. P_m is the perimeter of the membrane, C_m is the capacitance of the membrane, both constant, and $r_i(x)$ and $r_e(x)$ are the intercellular and extracellular resistivities, respectively. We take $\frac{r_e(x)}{r_i(x)} << 1$ meaning the extracellular medium provides little resistance relative to

intercellular resistance, so that $\frac{1}{r_i(x)+r_e(x)} \approx \frac{1}{r_i(x)}$, and the only spatial variation in resistance is due to intercellular resistance.

We scale space by the length of the strip of tissue, L, and time by the time constant, $C_m R_m$, where R_m is the membrane resistivity, while rescaling parameters to get a V equation

$$\left(\frac{\partial V}{\partial t} + F(V, \mathbf{w})\right) = \frac{\partial}{\partial x}\left(D(x)\frac{\partial V}{\partial x}\right),$$

where $D(x) = \frac{R_m}{P_m L^2 r_i(x)}$ is a nondimensional conductance coefficient, and $F(V, \mathbf{w}) = I_{ion}/R_m$. The degree of ischemia parameter $\mathbf{P}(x)$ is incorporated in the reaction kinetics as a vector of spatially dependent parameters

$$\left(\frac{\partial V}{\partial t} + F(V, \mathbf{w}, \mathbf{P}(x))\right) = \frac{\partial}{\partial x}\left(D(x)\frac{\partial V}{\partial x}\right).$$

Since the strips of tissue in experiments are finite and current does not flow out of the ends of the tissue, we take no flux boundary conditions.

$$D(0)V_x(0) = 0 = D(1)V_x(1).$$

To represent the effectively discontinuous jump between the ischemic chamber and normal chamber in experiments, we take the degree of ischemia parameter $\mathbf{P}(x)$ and the conductivity coefficient $D(x)$ to be piecewise constant

$$D(x) = \begin{cases} D_1 & 0 < x < m, \\ D_2 & m < x < 1, \end{cases}$$

$$\mathbf{P}(x) = \begin{cases} \mathbf{p}_0 & 0 < x < m, \\ \mathbf{p} & m < x < 1, \end{cases}$$

where $D_1, D_2, \mathbf{p}_0$ and $\mathbf{p}$ are constant and m denotes the position of the border between ischemic and normal regions and is the percentage of normal tissue in the domain (i.e., $m \to 1$ means all tissue is normal, while $m \to 0$ means all tissue is ischemic.)

In the interest of using phase plane analysis to show existence of steady solutions to the one-dimensional spatial model, we use a particularly simple two state model of FitzHugh-Nagumo type [8, 9].

$$\begin{aligned} \frac{\partial V}{\partial t} &= (D(x)V_x)_x + f(V, P(x)) - w, \\ \frac{\partial w}{\partial t} &= \epsilon(V - \gamma w), \end{aligned} \tag{3.1}$$

where $f(V, P(x))$ is a general cubic-like function of V with dependence on the scalar parameter $\mathbf{P} = P$ similar to that described in Section 2.4 or 2.5 (i.e., increasing resting potential as p increases eventually leading to inexcitability). Since (3.1) is not defined at $x = m$, we require that a solution of (3.1) also satisfy $\lim_{x\to m^-} V = \lim_{x\to m^+} V$ and $\lim_{x\to m^-} D(x)V_x = \lim_{x\to m^-} D(x)V_x$ so that the transmembrane potential and flux are continuous at $x - m$.

We suppose that

$$f(0, p_0) = f(a, p_0) = f(1, p_0) = 0 \ ; \ 0 < a < \frac{1}{2}$$

$$f(V, p_0) < 0 \ ; \ 0 < V < a$$

$$f(V, p_0) > 0 \ ; \ a < V < 1$$

$$f'(0, p_0) \neq 0 \neq f'(1, p_0)$$

$$\int_0^1 f(V, p_0) dV > 0$$

which guarantees excitability for nonischemic conditions [19]. In addition, we assume that the dependence of f upon P satisfies

$$f(V^*, 1) = 0 \text{ for some } V^* > a \tag{3.2}$$

$$f'(V, 1) < 0 \text{ for all } V \tag{3.3}$$

$$\frac{df(V, P)}{dP} \geq 0 \text{ for all } V \tag{3.4}$$

The first condition (3.2) guarantees a zero of f as P increases. The second condition forces f to have a negative slope for all V for p sufficiently large. The final condition ensures that at each point V, f is an increasing function of P. For example, $f(V, P) = (1 - P)V(V - a)(1 - V) + P(1 - V)$ with $V^* = 1$, the MM

model (2.6) with $V^* = 1$, and the RHH model (2.4) all satisfy the stated conditions. Finally, we let γ be such that $-f(V,p) + \frac{1}{\gamma}V$ is strictly increasing and has a unique zero.

3.3 Steady State Behavior

The steady state solution $(V(x), w(x))$ to (3.1) satisfies the equations,

$$\begin{aligned} 0 &= (D(x)V_x)_x + f(V, P(x)) - w, \\ 0 &= V - \gamma w, \end{aligned}$$

with boundary conditions $D(0)V_x(0) = D(1)V_x(1) = 0$. We write this as a second order ordinary differential equation in V

$$0 = (D(x)V_x)_x + f(V, P(x)) - \frac{1}{\gamma}V, \tag{3.5}$$

which we rewrite as a system of first order equations in space and study in the phase plane as

$$\begin{aligned} D(x)V_x &= U, \\ U_x &= (-f(V, P(x)) + \frac{1}{\gamma}V), \end{aligned} \tag{3.6}$$

with $D(x)$ and $P(x)$ piecewise constant. Since $-f(V,p)+\frac{1}{\gamma}V$ is strictly increasing it has a unique zero at $V = \phi(P(x))$. Figure 3.1 shows the phase plane for $P(x) = p_0$.

The first order system (3.6) then has a unique equilibrium at $(V, U) = (\phi(P(x)), 0)$. The stability of the equilibrium is found by linearizing about the equilibrium and solving the characteristic equation for the eigenvalues, which are

$$\lambda_{1,2} = \pm\frac{1}{\sqrt{D}}\sqrt{-f'(\phi(P), P) + \frac{1}{\gamma}}.$$

Since $-f(V,P) + \frac{1}{\gamma}V$ is strictly increasing in V, $-f'(V,P) + \frac{1}{\gamma}$ is positive for all V. Thus, the equilibrium is a saddle point with a stable and an unstable manifold. These manifolds are calculated explicitly as solutions to (3.5). Multiplying each side of (3.5) by DV_x and integrating yields

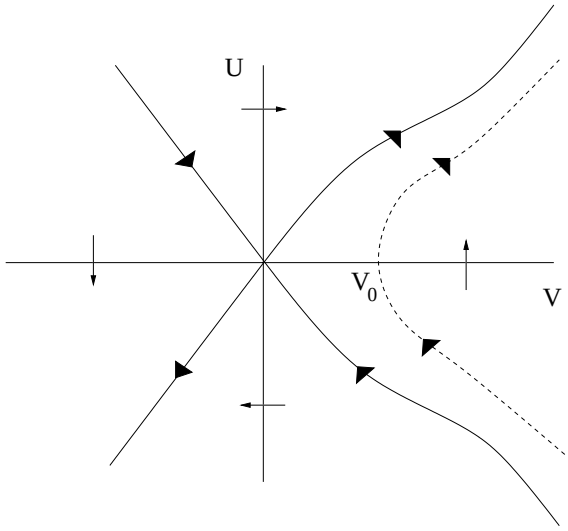

Figure 3.1: Phase plane for the system (3.6) with $P(x) = p_0$ and $\phi(p_0) = 0$. V_0 denotes the intersection of the V-axis by the steady state solution trajectory with $V(0) = V_0$.

$$\begin{aligned} DV_x &= \pm\sqrt{2D}\sqrt{\int(-f(V,P)V_x + \frac{1}{\gamma}VV_x)\,dx} \\ &= \pm\sqrt{2D}\sqrt{\int_K^V(-f(s,p) + \frac{1}{\gamma}s)\,ds} \end{aligned}$$

The constant, K, is chosen depending upon which solution is desired. For the stable (unstable) manifold, as $x \to -\infty (x \to \infty)$ with $P = p_0$, DV_x should go to 0 and V should go to $\phi(p_0)$, so $K = \phi(p_0)$. Solutions crossing the V-axis at $V = V_0$ are represented by $K = V_0$. These trajectories may be thought of as the solution to the boundary value problem (3.5) with boundary conditions $DV_x(0) = 0$ and $V(0) = V_0$. However, there is no way to satisfy $DV_x(1) = 0$ and $DV_x(0) = 0$ with such a trajectory.

With piecewise constant $P(x)$ and $D(x)$, $\phi(P(x))$ has two values depending on the point in space, so there are two steady states of the system (3.6)

$$(\phi(P(x)), 0) = \begin{cases} (\phi(p_0), 0) & x < m \\ (\phi(p), 0) & x > m. \end{cases}$$

Without loss of generality we let $\phi(p_0) = 0$ and $\phi(p) = \overline{V}$ (see Figure 3.2).

Define $\Gamma_L(x, V_0^L)$ as the trajectory in phase space following dynamics for $0 < x < m$ with $V(0) = V_0^L$ and $U(0) = 0$.

Similarly, let $\Gamma_R(x, V_0^R)$ be the trajectory in phase space following dynamics for $m < x < 1$ with $V(1) = V_0^R$ and $U(1) = 0$. Notice that $\Gamma_L(x, V_0^L)$ is a monotonically increasing function in the (V, U)-plane, and $\Gamma_L(x, V_0^R)$ is a monotonically decreasing function in the (V, U)-plane for $U > 0$ and $V \in [0, \overline{V}]$ (see Figure 3.2). There exists a solution to (3.5) with no flux boundary conditions if for some $0 < V_0^L < V_0^R < \overline{V}$, $\Gamma_L(m, V_0^L) = \Gamma_R(1 - m, V_0^R)$. Consider $\Gamma_L(m, V_0^L)$ as a curve parameterized by $V_0^L \in [0, \overline{V}]$. Then

(a) $\Gamma_L(m, V_0^L)$ is continuous in V_0^L.

(b) On $\Gamma_L(m, 0)$, $V \equiv 0$ and $U \equiv 0$.

(c) The V component of $\Gamma(m, V_0^L)$ is increasing for increasing V_0^L.

Property (a) holds because each component of $\Gamma_L(m, V_0^L)$ depends continuously on V_0^L (V-component depends continuously on initial conditions). Property (b) holds because (0,0) is a fixed point of (3.6). Property (c) holds because (3.6) is autonomous on $0 < x < m$.

We also consider $\Gamma_R(1 - m, V_0^R)$ as a curve parameterized by $V_0^R \in [0, \overline{V}]$. Then

(a) $\Gamma_R(1 - m, V_0^R)$ is continuous in V_0^R.

(b) On $\Gamma_R(1 - m, 1)$, $V \equiv \overline{V}$ and $U \equiv 0$.

(c) The V component of $\Gamma(1 - m, V_0^R)$ is decreasing for decreasing V_0^R.

The U-component of each of $\Gamma_L(m, V_0^L)$ and $\Gamma_R(1 - m, V_0^R)$ as it depends on V_0^L and V_0^R, respectively, is bounded below by 0. The U-component of $\Gamma_L(m, V_0^L)$ is bounded above by the unstable manifold coming from (0,0) for $U > 0$, and the U-component of $\Gamma_R(1-m, V_0^R)$ is bounded above by the stable manifold coming into $(\bar{V}, 0)$ for $U > 0$. This means that $\Gamma_L(m, V_0^L)$ and $\Gamma_R(1-m, V_0^R)$ are forced to cross at least once in the (V, U) plane. This yields the desired solution to (3.5). In Figure 3.2, a caricature of the curves $\Gamma_L(m, V_0^L)$ and $\Gamma_R(1 - m, V_0^R)$ parameterized by V_0^L

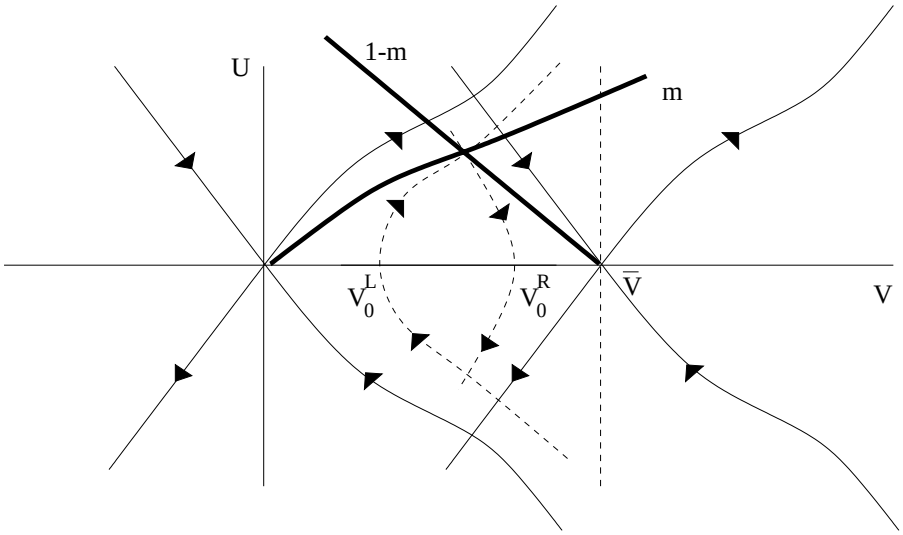

Figure 3.2: Phase plane for the system (3.6) for the piecewise constant $P(x)$ and $D(x)$. The vertical dashed line, $V = \overline{V}$, is the U-nullcline for $x > m$, the U-axis is the U-nullcline for $x < m$, and the V-axis is the V-nullcline for all of x. The solid curves intersecting at the origin and at $(V, U) = (\bar{V}, 0)$ are the stable and unstable manifolds of the unique steady state for $x < m$ and $x > m$, respectively. The dashed curve originating at V_0^L and ending at V_0^R represents a solution to (3.5).

and V_0^R are shown and denoted by thick lines and m and $1 - m$, respectively. The solution trajectory is the dashed curve above the V-axis. An m amount of space is traversed by the left trajectory followed by an $1 - m$ amount of space traversed by the right trajectory. At the corner where $\Gamma_L(m, V_0^L)$ and $\Gamma_R(1 - m, V_0^R)$ intersect, $x = m$. At $x = m$, both V and $U = D(x)V_x$ are continuous, as required, though not differentiable. Uniqueness is guaranteed with monotonicity of the m and $1 - m$ curves, but monotonicity of the m and $1 - m$ curves is not guaranteed for a general cubic like f. In the following section, a super and subsolution technique is used to show existence and uniqueness.

3.4 Existence and Uniqueness of the Steady State Solution

To establish the existence and uniqueness of the solution to (3.5) with no flux boundary conditions, we first consider the general equation defining $' \equiv \frac{\partial}{\partial x}$.

$$0 \;=\; (D(x)u')' + g(u,x) \tag{3.7}$$

with boundary conditions

$$u'|_{x=0}^{x=1} = 0$$

where $g : R \times [0,1] \to R$ is Lipschitz continuous in u with a unique zero $u = z(x)$ and is piecewise continuous and bounded in x and $D(x)$ is discontinuous.

Since g is potentially discontinuous in x, we consider the weak formulation of (3.7) and seek a weak solution $u \in H^1([0,1])$ to

$$\int_0^1 Du'v'\,dx \;=\; \int_0^1 g(u,x)v\,dx \tag{3.8}$$

where this equation holds for all $v \in H^1([0,1])$. Weak supersolutions $\overline{u}$ and subsolutions $\underline{u}$ of (3.7) satisfy the differential inequalities

$$\int_0^1 D\overline{u}'v'\,dx \;\geq\; \int_0^1 g(\overline{u},x)v\,dx \tag{3.9}$$

$$\int_0^1 D\underline{u}'v'\,dx \;\leq\; \int_0^1 g(\underline{u},x)v\,dx \tag{3.10}$$

where these inequalities hold for all $v \in H^1([0,1])$ and $v \geq 0$. For example, $\overline{u} = z(1)$ and $\underline{u} = z(0)$ are super and subsolutions of (3.7), respectively.

Theorem 1 *Suppose there exist weak super and subsolutions to (3.7) such that*

$$\underline{u} \leq \overline{u} \text{ a.e. in } [0,1].$$

Then there exists a weak solution $u(x)$ to (3.7) such that

$$\underline{u} \leq u \leq \overline{u} \text{ a.e. in } [0,1]$$

Proof: We proceed following Evans [7]. Fix λ so large that $g(u,x)+\lambda u$ is nondecreasing in u. This is possible since the slope of g is bounded. Write $u_0 = \underline{u}$, and then given $u_k (k = 0,1,2,...)$ inductively define $u_{k+1} \in H^1([0,1])$ to be the unique weak solution of the linear boundary value problem

$$Lu_{k+1} = -(Du')' + \lambda u_{k+1} \quad = \quad g(u_k, x) + \lambda u_k \tag{3.11}$$

with boundary conditions

$$u'|_{x=0,1} \quad = \quad 0 \tag{3.12}$$

The unique weak solution for $Lu = f(x)$ with $u'|_{x=0,1}$ is

$$u(x) = \int_0^x \frac{u_2(x)u_1(\xi)}{D(\xi)W(\xi)} f(\xi)\, d\xi + \int_x^1 \frac{u_1(x)u_2(\xi)}{D(\xi)W(\xi)} f(\xi)\, d\xi$$

where u_1 solves the homogeneous equation $Lu = 0$ and $u'|_{x=0} = 0$ and u_2 solves the homogeneous equation $Lu = 0$ and $u'|_{x=1} = 0$. $W(\xi) = u_1'(\xi)u_2(\xi) - u_1(\xi)u_2'(\xi)$ is the Wronskian.

We claim:

$$\underline{u} = u_0 \le u_1 \le u_2 \le ... \le u_k \le ...$$

For $k = 0$, from (3.11)

$$\int_0^1 Du_1'v' + \lambda u_1 v\, dx = \int_0^1 g(u_0, x)v + \lambda u_0 v\, dx.$$

Subtracting this from (3.10) and recalling that $u_0 = \underline{u}$ yields

$$\int_0^1 D(u_0 - u_1)'v' + \lambda(u_0 - u_1)v\, dx \le \int_0^1 (g(u_0,x) - g(u_0,x))v\, dx = 0.$$

Let $v = (u_0 - u_1)^+ \in H^1([0,1])$ and $v \ge 0$ where $u^+ = \begin{cases} u & u \ge 0 \\ 0 & u \le 0 \end{cases}$. Then

$$\int_0^1 D(u_0 - u_1)'[(u_0 - u_1)^+]' + \lambda(u_0 - u_1)(u_0 - u_1)^+\, dx \le 0$$

and over the part of $[0,1]$ where $\{u_0 \ge u_1\}$ we get

$$\int_{\{u_0 \ge u_1\}} D[(u_0 - u_1)']^2 + \lambda(u_0 - u_1)^2\, dx \le 0$$

so that $u_0 \le u_1$ a.e. in [0,1].

Now assume inductively

$$u_{k-1} \leq u_k \text{ a.e. in } [0,1].$$

From (3.11) we find

$$\int_0^1 Du'_{k+1}v' + \lambda u_{k+1}v \, dx = \int_0^1 g(u_k, x)v + \lambda u_k v \, dx \tag{3.13}$$

and

$$\int_0^1 Du'_k v' + \lambda u_k v \, dx = \int_0^1 g(u_{k-1}, x)v + \lambda u_{k-1} v \, dx. \tag{3.14}$$

Subtract (3.13) from (3.14), and set $v = (u_k - u_{k+1})^+$. We deduce

$$\begin{aligned} &\int_{\{u_k \geq u_{k+1}\}} D[(u_k - u_{k+1})']^2 + \lambda(u_k - u_{k+1})^2 \, dx \\ = &\int_0^1 [(g(u_{k-1}, x) + \lambda u_{k-1}) - (g(u_k, x) + \lambda u_k)](u_k - u_{k+1})^+ \, dx \leq 0, \end{aligned}$$

the last inequality holding because $u_{k_1} \leq u_k$ and $g(u, x) + \lambda u$ is nondecreasing. Therefore, $u_k \leq u_{k+1}$ a.e. in [0,1] proving the claim.

Now we show that u_k is bounded above by $\overline{u}$ a.e. in [0,1] for $k = 0, 1, 2, ...$ By assumption $\underline{u} = u_0 \leq \overline{u}$. Assume $u_k \leq \overline{u}$ a.e. in [0,1] for some k. Subtracting (3.9) from (3.13) and taking $v = (u_{k+1} - \overline{u})^+$, we get

$$\begin{aligned} &\int_{\{u_{k+1} \geq \overline{u}\}} D[(u_{k+1} - \overline{u})']^2 + \lambda(u_{k+1} - \overline{u})^2 \, dx \\ \leq &\int_0^1 [(g(u_k, x) + \lambda u_k) - (g(\overline{u}, x) + \lambda \overline{u})](u_{k+1} - \overline{u})^+ \, dx \leq 0. \end{aligned}$$

Thus, $u_{k+1} \leq \overline{u}$ a.e. in [0,1].

Now we have an increasing sequence bounded below by $\underline{u}$ and above by $\overline{u}$ a.e. in [0,1], so that

$$u(x) = \lim_{k \to \infty} u_k(x)$$

exists for a.e. x. Furthermore we have $u_k \to u$ in $L^2([0,1])$ as guaranteed by the Dominated Convergence Theorem. Since we have

$$||g(u_k, x)||_{L^2([0,1])} \leq C(||u_k||_{L^2([0,1])} + 1)$$

from the bounded slope of g with respect to u, we get from the weak formulation of the linear boundary value problem (3.11) that $||u_k||_{H^1([0,1])} < \infty$ for each k

including the supremum so that the sequence u_k weakly converges in $H^1([0,1])$ to $u(x) \in H^1([0,1])$

We verify that u is a weak solution to (3.7). Fix $v \in H^1([0,1])$. Then taking the limit $k \to \infty$ of (3.13) we find

$$\int_0^1 Du'v' + \lambda uv \, dx \;\; = \;\; \int_0^1 g(u,x)v + \lambda uv \, dx.$$

Canceling the terms with λ confirms that

$$\int_0^1 Du'v' \, dx \;\; = \;\; \int_0^1 g(u,x)v \, dx,$$

as desired.

Since $H^1([0,1]) \subset C([0,1])$ [22], $u(x) \in C([0,1])$. We also verify that the flux $D(x)u'$ is continuous by integration by parts while considering a discontinuity in D at x_0. Multiplying (3.7) by a test function $v \in H^1([0,1])$ and integrating by parts on each side of x_0 yields

$$D(x)u'(x)|_{x=x_0^-}^{x=x_0^+} + \int_0^1 Du'v' \, dx = \int_0^1 g(u,x)v \, dx$$

Since u is a weak solution of (3.7), $D(x)u'(x)|_{x=x_0^-}^{x=x_0^+} = 0$, so that $D(x)u'$ is continuous at x_0. It is worth noting that outside of discontinuities in g and D, the solution $u(x)$ is a classical solution (i.e., $u \in C^2([0,1])$). This shows the equivalence between the weak solution described here and the solution found in Section (3.3), so that the phase plane solution in indeed unique.

3.5 Explicit Calculation of the Steady State Solution

Recall that the function $f(V, P(x)$ defined in Section 2.5 for the modified McKean (MM) model is

$$f(V,P) = \begin{cases} -V + P & V \leq \frac{a}{2} + \frac{P}{k} \\ \sigma V + \eta & \frac{a}{2} + \frac{P}{k} \leq V \leq \frac{1+a}{2} \\ -V + 1 & \frac{1+a}{2} \leq V \end{cases}$$

where

$$\sigma = \frac{2Pk - 2P - k}{2P - k},$$

and

$$\eta = \frac{2P + ak - aPk - Pk}{2P - k}.$$

To find a solution of (3.5) on $0 < x < 1$ we construct a solution $V_L(x)$ on $0 < x < m$ and $V_R(x)$ on $m < x < 1$ and then require continuity of V and U.

As discussed in Section 3.3 and shown in Figure 3.2, there exists a unique steady state for each region in space $0 < x < m$ and $m < x < 1$, $\phi = 0$ and $\phi = \bar{V}$, respectively. Solutions corresponding to $0 < x < m$, $V_L(x)$, are matched smoothly to solutions of $m < x < 1$, $V_R(x)$. Toward this end each solution is calculated separately leaving open $V_L(0) = V_0$ and $V_R(1) = V_f$ conditions to be found while achieving continuity of the solution and continuity of the flux.

Define ξ_1 and ξ_2 by $V_L(\xi_1) = \frac{a}{2}$ and $V_R(\xi_2) = \frac{a}{2} + \frac{p}{k}$. If they exist, $\xi_1 \leq \xi_2$. From the definition of $f(V, P(x))$, $\phi(P)$ never exceeds $\frac{(1+a)}{2}$, so we need not consider that branch of the dynamics when calculating the steady state solutions.

The steady state solutions are classified into four cases:

- Case I: $0 < \xi_1 < \xi_2 < 1$; $(V_0 < \frac{a}{2}, V_f > \frac{a}{2} + \frac{p}{k})$
- Case II: $0 < \xi_2 < 1$; $(V_0 > \frac{a}{2}, V_f > \frac{a}{2} + \frac{p}{k})$
- Case III: $0 < \xi_1 < 1$; $(V_0 < \frac{a}{2}, V_f < \frac{a}{2} + \frac{p}{k})$
- Case IV: no ξ_1, ξ_2; $(V_0 < \frac{a}{2}, V_f < \frac{a}{2} + \frac{p}{k})$

The steady states are further classified into subcases depending on the interval in which m is located (i.e., Case I, Subcase I: $0 < m < \xi_1$). The results of the steady state calculations are found in Appendix C. An example of a steady state is shown in Figure 3.3. With the steady states calculated, we linearize the full partial differential system (3.1) about them and determine their linear stability.

3.6 Stability of the Steady State Solution

The question now is the linear stability of the steady state solution, $(V^*, w^*) = (\phi(x), \frac{1}{\gamma}\phi(x))$ of (3.1), found in the previous section. We linearize the system (3.1)

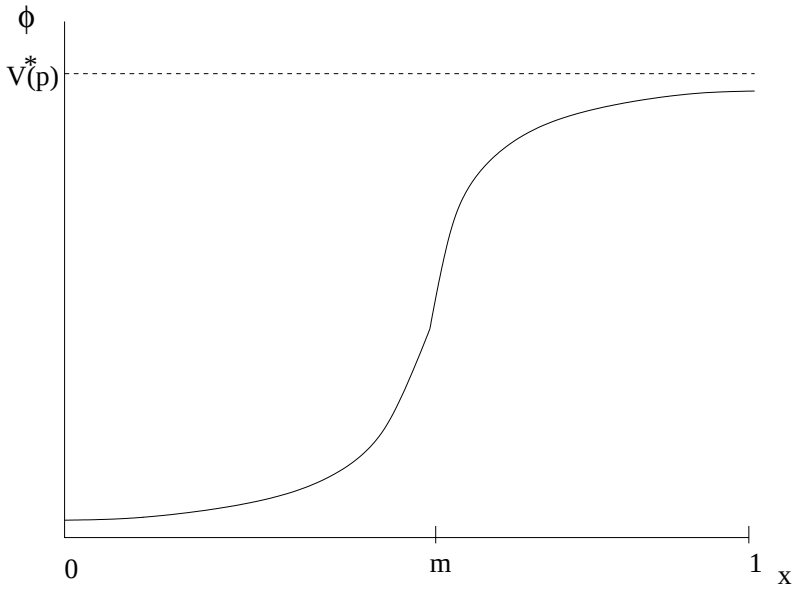

Figure 3.3: An example of a steady state solution to (3.1) with MM dynamics. The dashed line $\phi = V^*(p)$ is the steady state if $m = 0$, while the $\phi = 0$ line is the steady state for $m = 1$. The solid curve is the steady state with $m = 0.5$. The solution is not differentiable at $x = m$.

about $(\phi(x), \frac{1}{\gamma}\phi(x))$. We perturb the steady state solution with a small amplitude function $(\delta\widehat{V}(x,t), \delta\widehat{W}(x,t))$, where delta is small,

$$V(x,t) = \phi(x) + \delta\widehat{V}(x,t),$$

$$W(x,t) = \frac{1}{\gamma}\phi(x) + \delta\widehat{W}(x,t)$$

and substitute into (3.1) to get

$$\begin{aligned}
\delta\widehat{V}_t(x,t) &= (D\phi_x(x))_x + (D\delta\widehat{V}_x(x,t))_x + f(\phi(x) + \delta\widehat{V}(x,t), p) - \\
&\quad \frac{1}{\gamma}\phi(x) - \delta\widehat{W}(x,t) \\
\delta\widehat{W}_t(x,t) &= \epsilon(\phi(x) + \delta\widehat{V}(x,t) - \gamma(\frac{1}{\gamma}\phi(x) + \delta\widehat{W}(x,t)))
\end{aligned}$$

Linearizing the nonlinearity and using that $\phi(x)$ solves the steady state problem, the linearized system reduces to

$$\begin{aligned} \widehat{V}_t(x,t) &= (D\widehat{V}_x)_x(x,t) + f'(\phi(x),p)\widehat{V}(x,t) - \widehat{W}(x,t) \\ \widehat{W}_t(x,t) &= \epsilon(\widehat{V}(x,t) - \gamma\widehat{W}(x,t)) \end{aligned} \tag{3.15}$$

yielding equations for the perturbation functions.

Now we look for an eigenvalue problem of the linearized system (3.15) by substituting the form $\widehat{V}(x,t) = e^{\lambda t}v(x)$ and $\widehat{W}(x,t) = e^{\lambda t}w(x)$. Notice that $Re(\lambda) < 0$ are associated with perturbations of the steady state solution which decay, so that if the $Re(\lambda) < 0$ for all λ, the steady state solution is stable. Those that have $Re(\lambda) > 0$ are associated with perturbations of the steady state solution which grow, so that if $Re(\lambda) > 0$ for any λ, the steady state solution is unstable.

Substituting in $\widehat{V}(x,t) = e^{\lambda t}v(x)$ and $\widehat{W}(x,t) = e^{\lambda t}w(x)$ into (3.15) returns the ordinary differential system of equations in space

$$\begin{aligned} \lambda v &= (Dv_x)_x + f'(\phi(x),p)v - w \\ \lambda w &= \epsilon(v - \gamma w) \end{aligned}$$

so

$$w = \frac{\epsilon v}{\lambda + \epsilon\gamma}$$

and

$$(Dv_x)_x + \left[f'(\phi(x),p) - \lambda - \frac{\epsilon}{\lambda + \epsilon\gamma}\right] v = 0 \tag{3.16}$$

with the boundary conditions $v'(0) = v'(1) = 0$. The eigenpairs $(\lambda, v(x))$ satisfying (3.16) are sought. Notice that (3.16) is a Sturm-Liouville problem of the form

$$(Dv_x)_x + [\psi(x) + \mu]v = 0 \tag{3.17}$$

where the potential function is $\psi(x) = f'(\phi(x),p)$ and eigenvalues are given by μ where

$$\mu = \left(-\lambda - \frac{\epsilon}{\lambda + \epsilon\gamma} \right).$$

A similar analysis has been done for a semi-infinite domain and FitzHugh-Nagumo nonlinearity in [27],[28].

In this section we state general properties of eigenvalues of Sturm-Liouville problems of the form (3.17) [33]. Since the sign of the eigenvalues are important, bounds on eigenvalues based on the potential function are proven.

Properties of Sturm-Liouville Eigenvalues:
The eigenvalues of (3.17) with boundary conditions $v_x(0) = v_x(1) = 0$ are real, discrete and form an ordering such that

$$\mu_0 < \mu_1 < \mu_2, ...$$

and

$$\lim_{n\to\infty} \mu_n = \infty.$$

We narrow the region where the eigenvalues of interest exist based on the sign of $\psi(x)$ with the following lemma.

Lemma 1 *Since $D(x) > 0$, if $\psi(x) \leq 0$, then $\mu \geq 0$. Furthermore, $\mu = 0$ only if $\psi(x) \equiv 0$ and $v_x \equiv 0$*

Proof:
Write (3.17) as

$$(Dv_x)_x + \psi(x)v = -\mu v.$$

Multiply both sides by v and integrate over [0,1] integrating the second order term by parts to get

$$-\int_0^1 Dv_x^2 \, dx + \int_0^1 \psi(x)v^2 \, dx \;\; = \;\; -\mu \int_0^1 v^2 \, dx. \tag{3.18}$$

Everything on the left side is less than or equal to 0 so that $\mu \geq 0$. Notice $\mu = 0$ only if $\psi(x) \equiv 0$ and $v_x \equiv 0$ so that the eigenfunction must be a constant. □

The following lemma is useful in bounding the eigenvalues below even if the potential function is only bounded above by a positive constant.

Lemma 2 *If $\psi(x) \leq M$ for some constant $M > 0$, then $\mu \geq -M$.*

Proof:

From (3.18) in the above proof, we write

$$-\int_0^1 Dv_x^2\,dx + \int_0^1 \psi(x)v^2\,dx = -\mu\int_0^1 v^2\,dx$$

from which we get

$$-\int_0^1 Dv_x^2\,dx + M\int_0^1 v^2\,dx \geq -\mu\int_0^1 v^2\,dx$$

and

$$\mu \geq -M + \frac{\int_0^1 Dv_x^2\,dx}{\int_0^1 v^2\,dx} \geq -M.\square$$

The relationship between μ and λ is basic to understanding the stability of the steady state solution in (3.1). The eigenvalues of the Sturm-Liouville problem, μ, have the properties described in the previous section, while the sign of $Re(\lambda)$ determines whether perturbations to the steady state solution of (3.1) grow ($Re(\lambda) > 0$) or decay (($Re(\lambda) < 0$). The following calculation and graphs in Figures 3.4 and 3.5 describe the transformation between the two parameters.

$$\mu = -\lambda - \frac{\epsilon}{\lambda + \epsilon\gamma} \tag{3.19}$$

so that

$$\lambda = \frac{-(\mu + \epsilon\gamma) \pm \sqrt{(\mu - \epsilon\gamma)^2 - 4\epsilon}}{2}.$$

Notice that λ is real provided

$$\mu > 2\sqrt{\epsilon} + \epsilon\gamma$$

or

$$\mu < -2\sqrt{\epsilon} + \epsilon\gamma.$$

If the above inequalities are not satisfied, then at $\mu = -\epsilon\gamma$, $Re(\lambda) = 0$. This crossing of the μ-axis with λ imaginary always occurs (rather than occurring only when λ is real) because $\gamma > \frac{1}{\sqrt{\epsilon}}$.

The asymptotic $Re(\lambda)$ values are $-\mu, -\epsilon\gamma$. For large negative μ ($\mu < -1/\gamma$), $Re(\lambda)$ has one negative and one positive value, but for $\mu > -\epsilon\gamma$, both values of $Re(\lambda)$ are negative. Therefore, $Re(\lambda) < 0$ for all λ if and only if $\mu > -\epsilon\gamma$ for each μ. If there exists a $\mu < -\epsilon\gamma$, then the steady state of the system (3.1) with MM dynamics is unstable. Similarly, if there does not exist a $\mu < -\epsilon\gamma$, then the steady state of the system (3.1) with MM dynamics is stable. From the Sturm-Liouville theory it is sufficient to show the smallest μ is greater than (or less than) $-\epsilon\gamma$ to ensure stability (or instability) of the steady state.

We calculate the eigenfunctions and eigenvalues much like the steady state functions. The same four cases and their subcases apply. The eigenvalues are solved for from characteristic equations which come out of the matching. The calculations utilize Lemma 1 and Lemma 2 and the results are found in Appendix D.

In Figures 3.6 and 3.7, we show several regions of instability corresponding to different m-values in the p vs. D_2 parameter plane. The boundaries in these figures represents curves in parameter space where the $Re(\lambda) = 0$ or equivalently where the lowest Sturm-Liouville eigenvalue $\mu_0 = -\epsilon\gamma$. In Figure 3.6, $k = 6$, and so the ischemic model dynamics are not self-oscillatory under increases in p. Only for p sufficiently high and coupling in the ischemic region sufficiently close to that of the normal region is the full system unstable and then only for an intermediate range of m-values. However, in Figure 3.7 the ischemic model dynamics are self-oscillatory under increases in p. This leads to a much larger region of instability and regions which exist for a much broader range of m-values. For m small, the region of instability due to the self-oscillatory nature of the ischemic dynamics is the band of p-values between 0.22 and 0.58 for all D_2-values. As m increases, the region of instability grows beyond the self-oscillatory band. Comparing the regions in Figures 3.6 and 3.7, we can separate the instability regions into their mechanisms

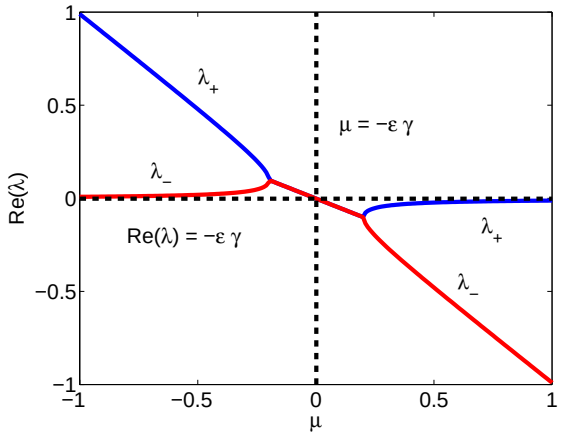

Figure 3.4: Plot of the $Re(\lambda)$ as a function of μ from (3.19). $\epsilon = 0.01$, $\gamma = 0.2$

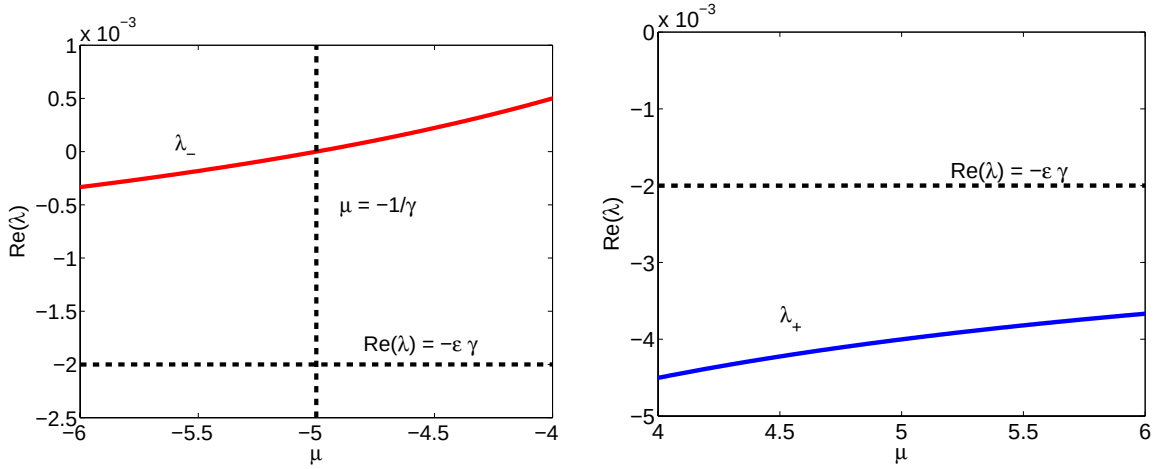

(a) (b)

Figure 3.5: Plot of the $Re(\lambda)$ as a function of μ from (3.19) for $|\mu|$ larger than Figure (3.4). In a) λ_- crosses 0 at $\mu = -1/\gamma$ and asymptotes to $Re(\lambda) = -\epsilon\gamma$. In b) λ_+ asymptotes to $Re(\lambda) = -\epsilon\gamma$ and remains below 0. $\epsilon = 0.01$, $\gamma = 0.2$

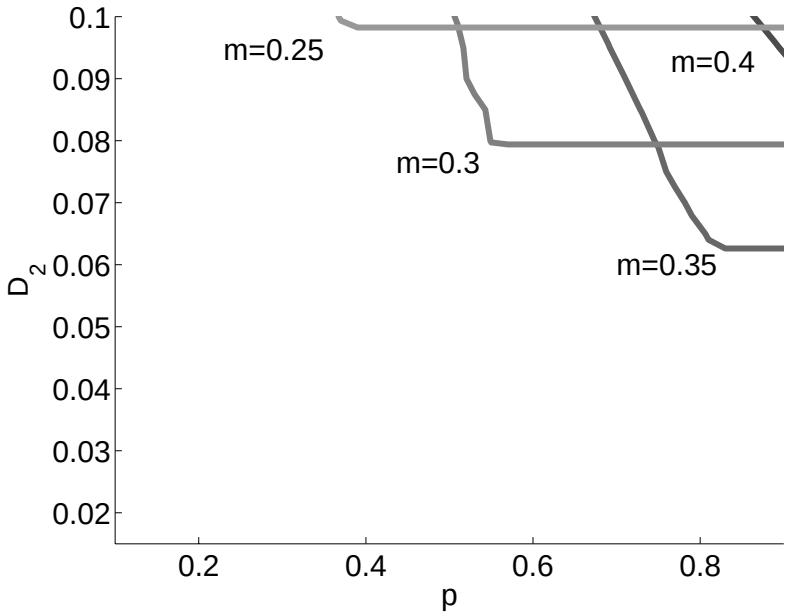

Figure 3.6: Instability regions of the in p and D_2 for several values of m and for $k = 6$ with $D_1 = 0.1$. Instability regions exist in the upper right corner of the figure.

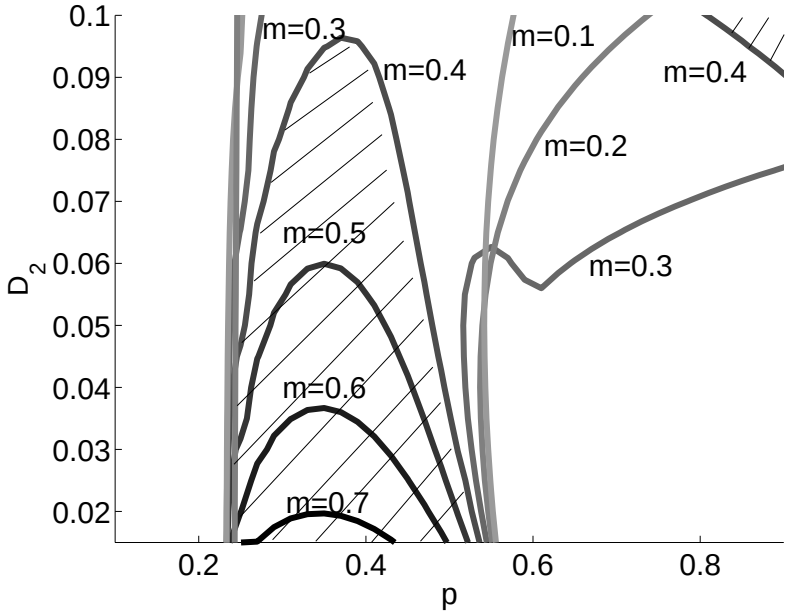

Figure 3.7: Instability regions of the in p and D_2 for multiple values of m and for $k = 8$ with $D_1 = 0.1$. The shaded region is the region of instability for $m = 0.4$

of instability. One mechanism is the self-oscillatory ischemic region driving oscillations, and the other mechanism is oscillations due to the coupling of two otherwise stable, quiescent regions. As m continues to increase, the instability region decreases. For m sufficiently large and the ischemic coupling strong enough the normally self-oscillatory dynamics in the band of p-values stabilizes. Only with very weak coupling for m large does the ischemic region oscillate.

3.7 Results

In Figure 3.8 a spatial plot, a phase plot, and a time plot are shown for parameter choices yielding an unstable steady state solution to (3.1). The spatial plot is a snapshot in time, t_0, of an oscillatory solution. That this solution is quite close to the steady state solution is observed in the phase plot as the thick line lying almost exactly along the dashed w-nullcline. The star and the circle represent $V(1, t_0)$ and $V(0, t_0)$, respectively, while the asterisk represents $V(m, t_0)$. The two loops in the phase plot are the trajectories parameterized by time in phase space of the two spatial endpoints. The thin lines on the phase plot represent the nullclines of the uncoupled (ODE in time) systems. The upper curve is with $p = 0.8$, while the lower one is $p = 0$. The loops in the phase portrait do not follow what would be the ODE dynamics due to the coupling. In fact, each of the two ODE dynamics separately would not be oscillatory. The lower V-nullcline and w-nullcline intersection indicates stability with excitability, while the upper V-nullcline and w-nullcline intersection indicates stability with inexcitability. So uncoupled, these two regions would be stable, but coupled together, oscillations ensue. The time plot in the bottom of Figure 3.8 shows this oscillation for transmembrane potential at $x = 0, m$, and 1.

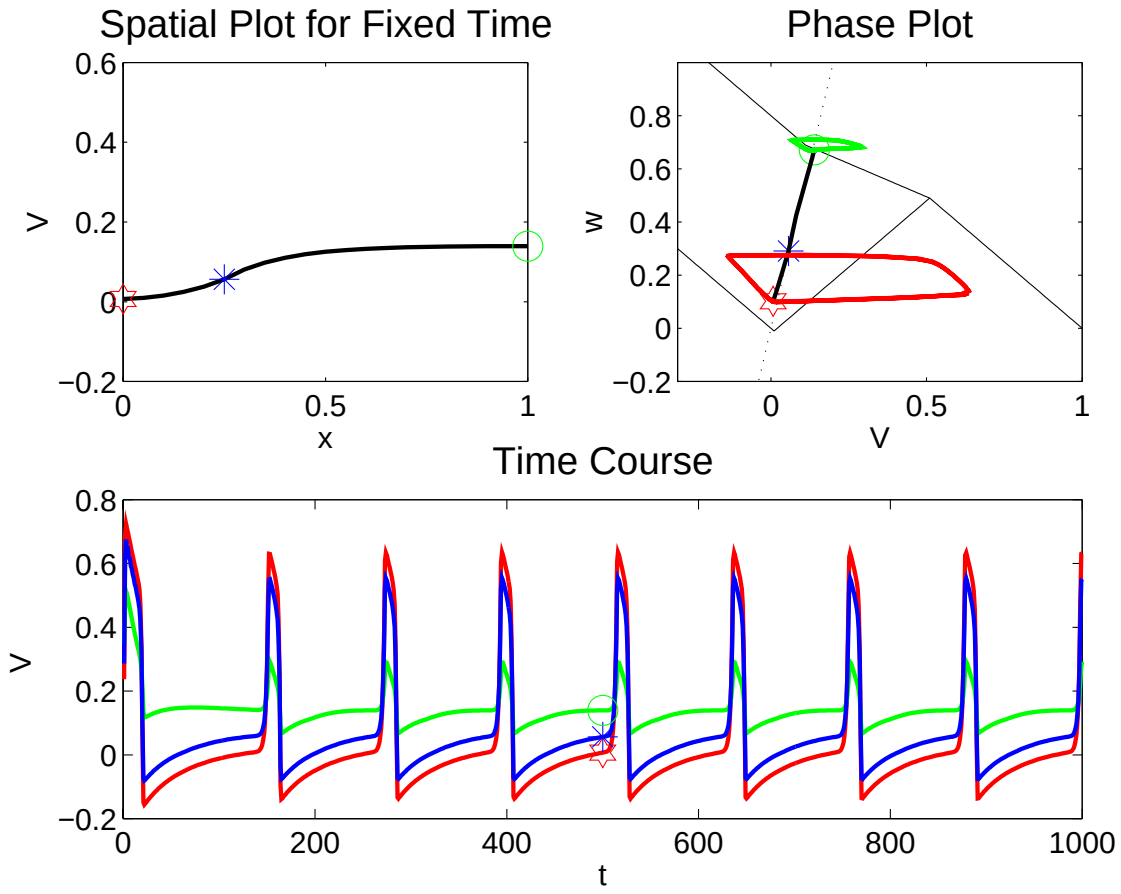

Figure 3.8: Spatial plot, phase plot, and time plot for parameter choices yielding an unstable steady state solution to (3.1) ($p = 0.8, k = 8, D_1 = 0.1, D_2 = 0.1, m = 0.3$). The spatial plot shows the transmembrane potential at a point in time. The closed loops in the phase plot are parameterizations of time at the end of the normal tissue ($x = 0 - \star$) and the end of the ischemic tissue ($x = 1 - \circ$). The curve lying almost exactly on $V = \frac{1}{\gamma}$, the w-nullcline, is a parameterization of space for the fixed time. Notice where the $x = m$ - * sits on that curve. The time plot shows the oscillation at the three points $x = 0, m, 1$. The position of the symbols in time correlates with the position in time in the other two plots.

3.8 Comparison with Picard Experiment

In the Picard experiment, electrodes were placed at either end of the cardiac strip, one in the ischemic region and one in the normal region. A recording of a spontaneous rhythm is shown in Figure 3.9 with measurements from each end along with the time plots from Figure 3.8 of the two spatial endpoints. The baseline transmembrane potential of the ischemic region in both the experimental and model plots is raised. The amplitude of the spontaneous action potentials that occur within the ischemic region of both the experimental and model plots is greatly reduced. The frequencies for the experimental and model plots are comparable, but this is coincidental and not mechanistic. The model seems to exhibit a slow depolarizing rise in transmembrane potential while there apparently is none in the experimental plot.

3.9 Short Strip Limit

It is useful to study an approximation of experimental relevance. In the limit that the coupling coefficient is large, possibly due to the length of tissue preparation being short (but still reasonable to model as a continuum), the following approximation is relevant.

Claim 1 *Let* $z : R \to R^n$, $y : [a,b] \times R \to R^n$, *and* $F : R^n \times [a,b] \to R^n$ *be such that*

$$\frac{dz}{dt} = \int_a^b F(z,x)\, dx$$

has periodic solutions, then

$$\frac{\partial y}{\partial t} = \frac{1}{\epsilon} D \frac{\partial^2 y}{\partial x^2} + F(y,x) \tag{3.20}$$

with boundary conditions $\frac{\partial y}{\partial x}|_{x=a} = \frac{\partial y}{\partial x}|_{x=b} = 0$ *has oscillatory solutions for* $\epsilon << 1$ *and* $D \in R^n \times R^n$.

We explore this claim using a perturbation argument. Since ϵ is small, we write a perturbation expansion in powers of ϵ. $y(x,t)$ has the representation in powers of ϵ

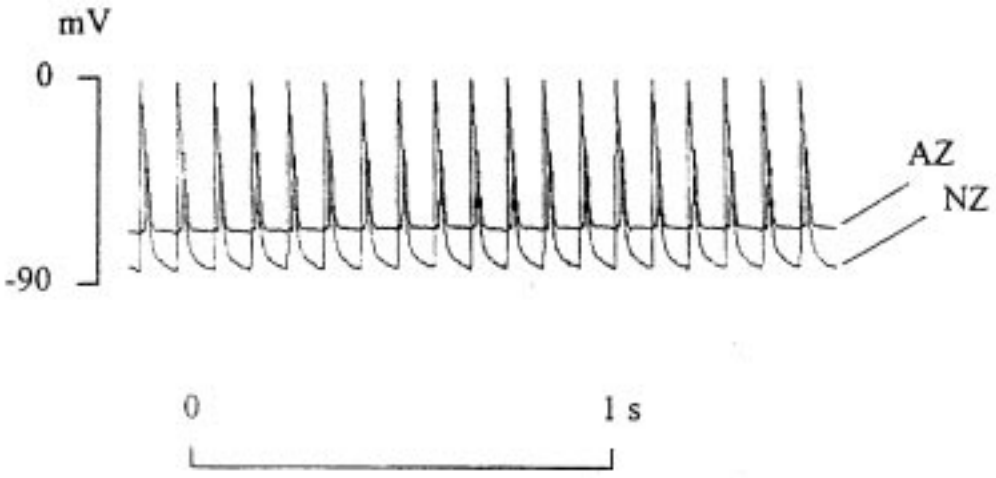

(a)

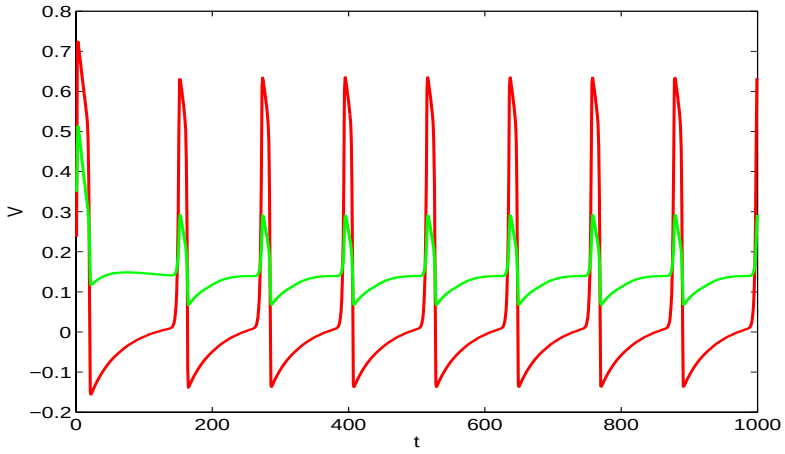

(b)

Figure 3.9: Qualitative comparison between (a) a typical recording of spontaneous oscillations in the Picard experiment and (b) the one-dimensional spatial model using MM dynamics. In both the experiment and the model, the ischemic zone (AZ) produces short action potentials returning to an elevated baseline, while the normal zone (NZ) has normal action potentials returning to a normal baseline. This particular recording was made in the presence of 1μM bimakalim which tended to increase the occurrence of spontaneous rhythms. The frequency of the oscillation is about 10Hz in the experiment.

$$y(x,t) = y_0(x,t) + \epsilon y_1(x,t) + \epsilon^2 y_2(x,t) + ... \tag{3.21}$$

We multiply (3.20) by ϵ so that the lowest order term is order 1.

$$\epsilon \frac{\partial y}{\partial t} = D\frac{\partial^2 y}{\partial x^2} + \epsilon F(y,x)$$

Substituting in the expansion of y from (3.21) we get the first order ordinary differential equation in space

$$D\frac{\partial^2 y_0}{\partial x^2} = 0$$

with boundary conditions $\frac{\partial y_0}{\partial x}|_{x=a} = \frac{\partial y_0}{\partial x}|_{x=b} = 0$, which has the undetermined solution $y_0(x,t) = y_0(t)$. The order ϵ equation is

$$D\frac{\partial^2 y_1}{\partial x^2} = \frac{\partial y_0}{\partial t} - F(y_0 + \epsilon y_1 + ..., x)$$

with boundary conditions $\frac{\partial y_1}{\partial x}|_{x=a} = \frac{\partial y_1}{\partial x}|_{x=b} = 0$. We expand F about the $y_0(t)$ solution to get the equation

$$D\frac{\partial^2 y_1}{\partial x^2} = \frac{\partial y_0}{\partial t} - F(y_0, x) - \epsilon F'(y_0, x)y_1 - ...$$

where F' is the Jacobian of F. Dropping the higher order terms yields

$$D\frac{\partial^2 y_1}{\partial x^2} = \frac{\partial y_0}{\partial t} - F(y_0, x), \tag{3.22}$$

and to guarantee a solution, y_1, exists, by the Fredholm Alternative Theorem [14] the right hand side of the equation must be orthogonal to the nullspace of the adjoint of the $D\frac{\partial^2}{\partial x^2}$ operator subject to boundary conditions. Since this operator is self-adjoint including the boundary conditions, we know $y_0(t)$ spans this nullspace. So for a solution, y_1, to exist the following equation must be satisfied

$$\int_a^b \left(\frac{\partial y_0}{\partial t} - F(y_0, x) \right) y_0 \, dx \;\; = \;\; 0,$$

so that

$$\frac{\partial y_0}{\partial t} \;\; = \;\; \int_a^b F(y_0, x) \, dx. \tag{3.23}$$

This is an equation for the first order solution to the partial differential equation (3.20). From the assumptions, this equation has a periodic solution.

By substituting (3.23) into (3.22), we see that the ϵ order solution of (3.20) solves

$$D \frac{\partial^2 y_1}{\partial x^2} = \int_a^b F(y_0, x) \, dx - F(y_0, x)$$

where the right hand side is the deviation in x from the average behavior of the reaction term.

For example, let $y = (V, w)^T$ and consider the system (3.1) with a constant D large and MM dynamics for f. The integral over [0,1] of the function representing MM dynamics is

$$\int_0^1 F(y, P(x)) = \int_0^m F(y, p_0) \, dx + \int_m^1 F(y, p) \, dx = mF(y, p_0) + (1-m)F(y, p).$$

This is a homotopy between the ischemic and normal dynamics with m the homotopy parameter. The dynamics for the order one solution come from choosing an m which fixes the homotopy parameter. The first order solution $y_0 = (V_0, w_0)^T$ then satisfies the ODE in time

$$\begin{pmatrix} V_0 \\ w_0 \end{pmatrix}_t \;\; = \;\; \begin{pmatrix} mf(V_0, p_0) + (1-m)f(V_0, p) - w_0) \\ \epsilon(V_0 - w_0) \end{pmatrix} \tag{3.24}$$

and

$$mf(V, 0) + (1-m)f(V, p) =$$

$$\begin{cases} -V + (1-m)p & V \leq \frac{a}{2} \\ (-1+2m)V - am + (1-m)p & \frac{a}{2} \leq V \leq \frac{a}{2} + \frac{p}{k} \\ (m + (1-m)\sigma)V - am + (1-m)\eta & \frac{a}{2} + \frac{p}{k} \leq V \leq \frac{1+a}{2} \\ -V + 1 & \frac{1+a}{2} \leq V \end{cases}$$

where

$$\sigma = \frac{2pk - 2p - k}{2p - k},$$

and

$$\eta = \frac{2p + ak - apk - pk}{2p - k}.$$

Figure 3.10 shows the nullclines of (3.24) for $m = 0$,0.7, and 1 and for $p = 0.8$ and $k = 6$. The steady state when $m = 0.7$ is unstable yielding oscillatory solutions to (3.24), while a fully ischemic dynamic ($m = 0$) or a fully normal dynamic ($m = 1$) has a stable steady state.

The mechanism of this oscillation is different here than in Theorem 1. Here the time dependent first order solution oscillates because of average reaction dynamics. In Theorem 1, the coupled cell oscillation is due to an applied current with appropriate leak from the ischemic cell driving the normal cell.

3.10 Conclusion

Using a modified McKean piecewise linear model of cardiac transmembrane ionics, a model strip of tissue oscillates when part of the tissue has an increased degree of ischemia. Parameter regions in relative size of ischemic tissue, conductance through ischemic tissue, and degree of ischemia are found where these oscillations exist. Mathematically these regions relate to instability of the steady state solution. The existence of a steady state solution is shown graphically in a phase plane for a general two-variable model. We state and prove a theorem using super and subsolutions shows existence and uniqueness of steady solutions following dynamics with more general inhomogeneities beyond that used for the MM model. For certain parameter regions where the model strip of tissue oscillates, if the tissue is cut at the membrane dividing ischemic and normal regions, each region would be independently stable. The normal region would recover to its stable, uniform, excitable rest state, while the ischemic region would return to its stable uniform, inexcitable rest state.

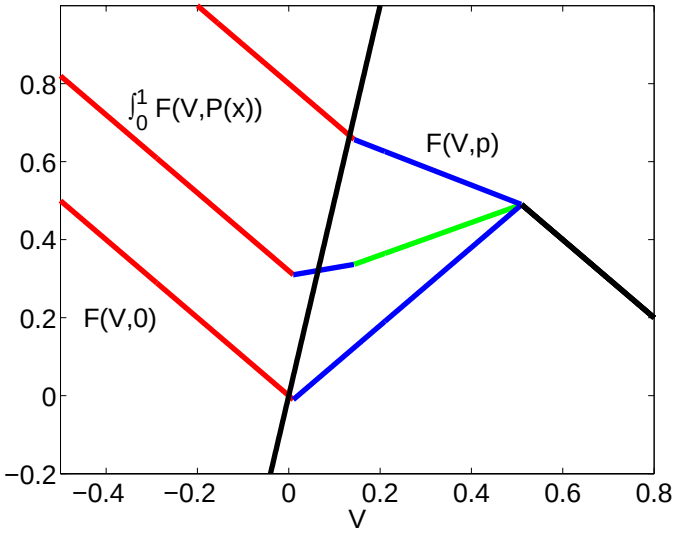

Figure 3.10: Nullclines for the first order problem (3.23) with m=0,0.6,and 1 and $p = 0.8$ and $k = 6$.

The appearance of oscillations initiating at the border between normal and ischemic tissue is explained by referring to the phase plot in Figure 3.8. The transmembrane potential for $x < m$ is pulled up so that the values of V at x closest to m are the most superthreshold. There is a balance between the superthreshold points exciting and their being restrained by coupling with points following ischemic dynamics. The direction of force of each of these regions of points is also dependent on the state of recovery of the respective system.

We compare the MM model results with the Picard experiment. There are regions of model parameters that allow for oscillatory behavior, and these oscillations have qualitative similarities to the experimental result. The action potential amplitude in the ischemic part of the tissue is greatly reduced from normal tissue levels. The baseline membrane potential is elevated or depolarized from the normal tissue levels. The fact that a two-variable system captures these features leads us to believe that the mechanism of oscillations occurring from elevated resting potentials and decoupling in ischemic tissue coupled to normal tissue is generic and robust.

APPENDIX A

LOU-RUDY I MODEL

The equations and parameters for the Luo-Rudy Model used in Chapter 2.

Parameter Name	Symbol	Value
Intracellular Potassium	K_i	145mM
Extracellular Sodium	Na_o	140mM
Intracellular Sodium	Na_i	18mM
% of Sodium Potassium	PR_{NaK}	0.01833
Ideal Gas Constant	R	8.315J $\text{mol}^{-1}\cdot\text{K}^{-1}$
Temperature	T	310K
Faraday's Constant	F	96.49 $\times 10^3$ C$\cdot$ mol^{-1}

Variable Name	Symbol
Transmembrane potential	V
Sodium Activation Gating Variable	m
Sodium Fast Inactivation Gating Variable	h
Sodium Slow Inactivation Gating Variable	j
Calcium Activation Gating Variable	d
Calcium Inactivation Gating Variable	f
Potassium Activation Gating Variable	x
Intracellular Calcium	Ca_i

Nernst Potential	Symbol	Value
Sodium	V_{Na}	54.4mV
Calcium	V_{Si}	$7.77 - 13.0287\log(Ca_i)$
Potassium	V_K	$\frac{RT}{F}\log((K_o + PR_{NaK}Na_o)/(K_i + PR_{NaK}Na_i))$
Potassium	V_{K1}	$\frac{RT}{F}\log(K_o/K_i)$
Potassium	V_{Kp}	V_{K1}
Background	V_b	-59.87

	Probabilities for Gating Variables
For V<-40	
	$a_h = 0.135\exp((80+V)/(-6.8))$
	$a_j = (-1.2714\times10^5\exp(0.2444V) -$
	$\quad 3.474\times10^{-5}\exp(-0.04391V))\cdot$
	$\quad (V+37.78)/(1+\exp(0.311(V+79.23)))$
	$b_h = 3.56\exp(0.079V)+3.1\times10^5\exp(0.35V)$
	$b_j = 0.1212\exp(-0.01052V)/(1+\exp(-0.1378(V+40.14)))$
For V $\geq$ 40	
	$a_h = 0$
	$a_j = 0$
	$b_h = 1/(0.13(1+\exp((V+10.66)/(-11.1))))$
	$b_j = 0.3\exp(-2.535\times10^{-7}V)/(1+\exp(-0.1(V+32)))$
For all V	
	$a_m = 0.32(V+47.13)/(1-\exp(-0.1(V+47.13)))$
	$b_m = 0.08\exp(-V/11)$
	$a_d = 0.095\exp(-0.01(V-5))/(1+\exp(-0.072(V-5)))$
	$b_d = 0.07\exp(-0.017(V+44))/(1+\exp(0.05(V+44)))$
	$a_f = 0.012\exp(-0.008(V+28))/(1+\exp(0.15(V+28)))$
	$b_f = 0.0065\exp(-0.02(V+30))/(1+\exp(-0.2(V+30)))$
For V>-100	
	$x_i = 2.837(\exp(0.04(V+77))-1)/$
	$\quad ((V+77)\exp(0.04(V+35)))$
For $V \leq$ -100	
	$x_i = 1$
	$a_x = 0.0005\exp(0.083(V+50))/(1+\exp(0.057(V+50)))$
	$b_x = 0.0013\exp(-0.06(V+20))/(1+\exp(-0.04(V+20)))$
	$a_{k1} = 1.02/(1+\exp(0.2385(V-V_{K1}-59.215)))$
	$b_{k1} = (0.49124\exp(0.08032(V-V_{K1}+5.476))+$
	$\quad \exp(0.06175(V-V_{K1}-594.31)))/$
	$\quad (1+\exp(-0.5143(V-V_{K1}+4.753)))$
Kp conductance	$K_p = 1/(1+\exp((7.488-V)/5.98))$

Channel Conductance	Symbol and Value
Sodium	$g_{Na} = 23m^3hj$
Calcium	$g_{Si} = 0.09df$
Potassium	$g_K = 0.282\sqrt{K_o/5.4}xx_i$
Potassium	$g_{K1} = 0.6047\sqrt{K_o/5.4}\frac{a_{k1}}{a_{k1}+b_{k1}}$
Potassium	$g_{Kp} = 0.0183K_p$
Background	$g_b = 0.03921$

Membrane Capacitance
$C_m = 1$

Currents	Symbol and Value
Sodium	$I_{Na} = g_{Na}(V - V_{Na})$
Calcium	$I_{Si} = g_{Si}(V - V_{Si})$
Potassium	$I_K = g_K(V - V_K)$
Potassium	$I_{K1} = g_{K1}(V - V_{K1})$
Potassium	$I_{Kp} = g_{Kp}(V - V_{Kp})$
Background	$I_b = g_b(V - V_b)$

Equations

$$\begin{aligned}
\frac{dV}{dt} &= -1/C_m(I_{Na} + I_{Si} + I_K + I_{K1} + I_{Kp} + I_b) \\
\frac{dy}{dt} &= \frac{y_\infty - y}{\tau_y} \\
\frac{dCa_i}{dt} &= -10^{-4} I_{Si} + 0.07(10^{-4} - Ca_i)
\end{aligned}$$

for $y \in \{m, h, j, d, f, x\}$ and $y_\infty = a_y/(a_y + b_y), \tau_y = 1/(a_y + b_y)$.

APPENDIX B

RHH MODEL BIFURCATION STUDY

Some of the bifurcation structure of the coupled cell system with RHH ionics has already been discussed within the main text (see Section 2.4). However, there are multiple co-dimension 2 bifurcations and a co-dimension 3 bifurcation, which are not particularly germane to understanding the stability boundary in parameter space but are nonetheless mathematically interesting.

As discussed in Chapter 2, we take a pair of cells and couple them as below

$$\begin{aligned} m\left(\frac{dV_1}{dt} - F(V_1, \mathbf{w}_1, \mathbf{p_0})\right) &= \chi\delta(V_2 - V_1) \\ \frac{d\mathbf{w}_1}{dt} &= g(V_1, \mathbf{w}_1) \\ (1-m)\left(\frac{dV_2}{dt} - F(V_2, \mathbf{w}_2, \hat{\mathbf{p}})\right) &= \chi\delta(V_1 - V_2) \\ \frac{d\mathbf{w}_2}{dt} &= g(V_2, \mathbf{w}_2) \end{aligned} \tag{B.1}$$

Understanding the behavior of the above system under various values of the relative mass, m, the degree of ischemia, $\hat{\mathbf{p}} = p$, and the coupling $\chi\delta$ is of interest. We choose the RHH model for its explicit dependence on extracellular potassium which we take to be the ischemic parameter. The ionic and recovery dynamics are

$$F(V, n, p) = -[\bar{g}_{Na} m_\infty^3 (0.85 - n)(V - V_{Na}) + \bar{g}_K n^4 (V - V_K(p)) + g_L(V - V_L)]$$

$$g(V, n) = \frac{n_\infty(V) - n}{\tau_n(V)}$$

We consider the three bifurcation parameters m, p, and $\chi\delta$, though at times we will use m, p, and $\frac{\chi\delta}{m}$ for bifurcation diagrams. We refer to the p-value of a given bifurcation point B as p_B.

Following the steady state in p for all $\frac{\chi\delta}{m}$ and m creates an S-shaped curve with an interval of p where there exist three steady states or branches (see Figure 2.3). There are two limit point bifurcations, LP_1 and LP_2, at p_{LP_1} and p_{LP_2} each associated with a bend in the steady state curve. At each limit point a real eigenvalue becomes zero. These are interpreted as a saddle equilibrium and a node equilibrium coming together at a saddle-node bifurcation, and they occur such that the middle branch of steady states is hyperbolic.

A second type of bifurcation occurs along the steady state curve, as well. A Hopf bifurcation, at which a complex pair of eigenvalues have zero real part, nonzero imaginary part, appears at least twice and up to four times. The solid and dashed lines of Figure 2.5 exhibit the position of the Hopf points in $\frac{\chi\delta}{m}$ versus p parameter space for a given m.

B.1 Subcritical Hopf Bifurcation

For sufficiently small m ($m < 0.86$) and all d when p increases to p_{HB_1} a Hopf bifurcation occurs (the HB_1 curve in the $\frac{\chi\delta}{m}$ versus p plane - see Figure 2.5). This Hopf bifurcation is subcritical leading to an unstable periodic solution emanating from the Hopf bifurcation for $p < p_{HB_1}$. For m small, the HB_1 curve is essentially constant in p for all $\frac{\chi\delta}{m}$. As m increases, the HB_1 curve appears like a saturating function in $\frac{\chi\delta}{m}$ with positive slope for small $\frac{\chi\delta}{m}$ and flattening for larger $\frac{\chi\delta}{m}$. For m larger than 0.86, the HB_1 curve ends in a co-dim 3 bifurcation at finite values of p and $\frac{\chi\delta}{m}$, which is discussed later.

B.2 Supercritical Hopf Bifurcation

Similarly, for m sufficiently small and all d as p decreases from potentially large values where the system maintains only a stable steady state, a super critical Hopf bifurcation occurs (the HB_2 curve in the $\frac{\chi\delta}{m}$ versus p plane). A stable periodic solution emanates from the steady state at this p-value. The HB_2 curve blows up in p as $\frac{\chi\delta}{m} \to 0$ and, at least for small m, asymptotes to an m dependent p-value for large $\frac{\chi\delta}{m}$. This curve shifts to larger p and $\frac{\chi\delta}{m}$ values as m increases so that the important aspect of the HB_2 curve is the remaining stable periodic solution

emanating from it.

B.3 Secondary Hopfs - Hopf Loop

In the $\frac{\chi\delta}{m}$ versus p plane as $\frac{\chi\delta}{m}$ decreases a looping Hopf curve appears in a Hopf-Hopf (HH_2) (two pairs of complex eigenvalues each pair with zero real part and nonzero imaginary part) co-dim 2 bifurcation. This bifurcation occurs on the upper branch of the steady state diagram. As $\frac{\chi\delta}{m}$ decreases slightly further, the lower (in p) of the Hopfs, a supercritical Hopf (HB_L), "goes around the corner" of the steady state diagram corresponding to a Fold-Hopf (FH_2) (a pair of complex eigenvalues with zero real part and nonzero imaginary part occurring with a real zero eigenvalue) co-dim 2 bifurcation and appears in the $\frac{\chi\delta}{m}$ versus p plane as a tangency between the HB_{loop} curve and the LP_1 curve. Continuing to decrease $\frac{\chi\delta}{m}$ following the lower part of the HB_{loop} the lower Hopf comes back around the corner and through another Hopf-Fold co-dim 2 bifurcation (FH_1), which is a second tangency between the HB_{loop} curve and the LP_1 curve in $\frac{\chi\delta}{m}$ versus p space. Decreasing $\frac{\chi\delta}{m}$ still further the the lower Hopf curve intersects with the upper Hopf curve, a subcritical Hopf (HB_U), leading to a second Hopf-Hopf (HH_1) co-dim 2 bifurcation. This crossing changes the stability of the steady state on the upper branch. Previously the interval of p between the two Hopf points on the HB_{loop} at any $\frac{\chi\delta}{m}$ value had been unstable, but for $\frac{\chi\delta}{m}$ below (HH_1) the interval becomes stable. The HB_L exists for $0 < \frac{\chi\delta}{m}$ and finite p, while $HB_U \to \infty$ in p as $\frac{\chi\delta}{m} \to 0$.

B.4 Periodic Solutions Related to the Hopf points

With four periodic solutions, two stable and two unstable, connected to the preceding Hopf points, it is important to understand for which parameter values they exist and how they may interact with each other and other steady states.

For small $\frac{\chi\delta}{m}$ there exist four Hopf bifurcation points in p. As p increases we encounter HB_1, HB_L, HB_U, and HB_2. They alternate between sub and supercritical bifurcations. HB_1 has an unstable periodic orbit that ends in a homoclinic orbit, HC_1, at p_{HC_1}. The stable orbit emanating from HB_L also ends in a homoclinic orbit, HC_L, at p_{HC_L}. The unstable periodic orbit from HB_U and the stable orbit

from HB_2 are connected at a limit point of the amplitude solution, LP_A, at $p_{LP_A} < p_{HB_U} < p_{HB_2}$. There is a p-interval of bistability of (p_{LP_A}, p_{HB_U}) since both a stable orbit and stable steady state (and an unstable orbit) exist on this interval. Similarly, for the other pair of Hopf bifurcations, if $p_{HC_L} < p_{HB_1}$ then there exists a p-interval of bistability of (p_{HC_L}, p_{HB_1}).

As $\frac{\chi\delta}{m}$ increases, HB_U decreases until meeting with HB_L at the bifurcation HH_2. At this point the super-critical HB_L joins with the sub-critical HB_U. When HB_L and HB_U reorient themselves in the HB_{loop} their periodic orbits, now both unstable, connect and become of little consequence for the determination of stability in parameter space.

B.5 Co-dimension 3 Bifurcation

As m increases the HB_1 curve increases in slope more quickly than the LP_2 curve above it in the $\frac{\chi\delta}{m}$ versus p plane. At about $m = 0.86$ the HB_1 curve and LP_2 curve become tangent ($p = 58, \frac{\chi\delta}{m} = 0.6$) in a Bogdonov-Takens-Fold (three real zeros) co-dim 3 bifurcation (the imaginary part of the Hopf eigenvalues become 0). This point of tangency then splits in $\frac{\chi\delta}{m}$ and p plane as m increases and becomes two Bogdonov-Takens bifurcations (BT_1,BT_2)(two real zeros) leaving only the limit point curve LP_2 between them.

As m continues to increase BT_2 increases along the LP_2 curve creating a loop in the HB_2 curve. In this loop there is another Hopf-Hopf bifurcation and a Hopf-Fold bifurcation (see Figure 2.5 (c)).

APPENDIX C

ANALYTICAL SOLUTION TO MM PDE

$f(V,p)$ is the piecewise linear function. For convenience $p = p(x)$.

$$f(V,p) = \begin{cases} -V + p & V \leq \frac{a}{2} + \frac{p}{k} \\ \sigma V + \eta & \frac{a}{2} + \frac{p}{k} \leq V \leq \frac{1+a}{2} \\ -V + 1 & \frac{1+a}{2} \leq V \end{cases}$$

where

$$\sigma = \frac{2pk - 2p - k}{2p - k}$$

and

$$\eta = \frac{2p + ak - apk - pk}{2p - k}$$

The form of this function is based on the reduced Hodgkin-Huxley model under changes in extracellular potassium. p denotes the level of "ischemia" while k affects the position of the minimum between $V = a/2$ and $w = V - a$ for a given p level which controls excitability and stability in the ODE sense.

This formulation follows the same idea as the standard cubic nonlinearity, but yields an analytically tractable problem. However, it is not possible to calculate such quantities as the direction of Hopf bifurcation due to the lack of continuity in the derivative of f with respect to u.

As exhibited in Figure(3.2), there exists a unique steady state for each p-value (0 or $\bar{p}$) for its respective space. Solutions corresponding to the $p = 0$ case, $V_L(x)$, will be matched continuously with continuous flux to solutions of the $p = \bar{p}$ case, $V_R(x)$. Toward this end each solution will be calculated separately leaving open $V_L(0) = V_0$ and $V_R(1) = V_f$ conditions to be solved for during matching.

Let $V_L(\xi_1) = \frac{a}{2}$ and $V_R(\xi_2) = \frac{a}{2} + \frac{p}{k}$. Notice that $\xi_1 \leq \xi_2$. It is clear from the definition of $f(V, p(x))$ that the steady state will never exceed $V = \frac{(1+a)}{2}$ so we will not bother to calculate steady state solutions in this regime.

Also let

$$\beta_i = \sqrt{\frac{\frac{1}{\gamma}+1}{D_i}}, \rho = \sqrt{\frac{\frac{1}{\gamma}-1}{D_1}}, \alpha = \sqrt{\frac{\frac{1}{\gamma}-\sigma}{D_2}}.$$

for $i = 1, 2$ representing the normal and ischemic regions, respectively.

Case[I]$(0 < \xi_1 < \xi_2 < 1$**,**$V_0 < \frac{a}{2}, V_f > \frac{a}{2} + \frac{p}{k})$

$$V_L(x) = \begin{cases} V_0 \cosh(\beta_1 x), & 0 \le x \le \xi_1 \\ A_L \cosh(\rho(x-\xi_1)) + B_L \sinh(\rho(x-\xi_1)) - \frac{a}{\frac{1}{\gamma}-1}, & \xi_1 \le x \le 1 \end{cases}$$

$$V_R(x) = \begin{cases} A_R \cosh(\beta_2(\xi_2 - x)) + B_R \sinh(\beta_2(\xi_2 - x)) + \frac{\bar{p}}{\frac{1}{\gamma}+1}, & 0 \le x \le \xi_2 \\ \left(V_f - \frac{\eta}{\frac{1}{\gamma}-\sigma}\right) \cosh(\alpha(1-x)) + \frac{\eta}{\frac{1}{\gamma}-\sigma}, & \xi_2 \le x \le 1 \end{cases}$$

where

$$\begin{aligned} A_L &= \tfrac{a}{2} + \tfrac{a}{\frac{1}{\gamma}-1} \\ B_L &= \tfrac{\beta_1}{\rho} V_0 \sqrt{\left(\tfrac{a}{2V_0}\right)^2 - 1} \\ A_R &= \tfrac{a}{2} + \tfrac{p}{k} - \tfrac{\bar{p}}{\frac{1}{\gamma}+1} \\ B_R &= \tfrac{\alpha}{\beta_2} \left(V_f - \tfrac{\eta}{\frac{1}{\gamma}-\sigma}\right) \sqrt{\left(\tfrac{\frac{a}{2}+\frac{p}{k}-\frac{\eta}{\frac{1}{\gamma}-\sigma}}{V_f - \frac{\eta}{\frac{1}{\gamma}-\sigma}}\right)^2 - 1} \end{aligned}$$

So

$$\xi_1 = \frac{1}{\beta_1} \cosh^{-1}\left(\frac{a}{2V_0}\right)$$

and

$$\xi_2 = 1 - \frac{1}{\alpha} \cosh^{-1}\left(\frac{\frac{a}{2} + \frac{p}{k} - \frac{\eta}{\frac{1}{\gamma}-\sigma}}{V_f - \frac{\eta}{\frac{1}{\gamma}-\sigma}}\right)$$

or B_L and B_R may be written in terms of ξ_1 and ξ_2 which is useful for the nonlinear solves.

$$\begin{aligned} B_L &= \tfrac{\beta_1}{\rho} \tfrac{a}{2} \tanh(\beta_1 \xi_1) \\ B_R &= \tfrac{\alpha}{\beta_2} \left(\tfrac{a}{2} + \tfrac{p}{k} - \tfrac{\eta}{\frac{1}{\gamma}-\sigma}\right) \tanh(\alpha(1-\xi_2)) \end{aligned}$$

And

$$V_0 = \frac{a}{2} \text{sech}(\beta_1 \xi_1),$$

$$V_f = \left(\frac{a}{2} + \frac{p}{k} - \frac{\eta}{\frac{1}{\gamma}-\sigma}\right) \text{sech}(\alpha(1-\xi_2)) + \frac{\eta}{\frac{1}{\gamma}-\sigma}$$

Subcase[I]($m < \xi_1$) The matching yields ξ_2 as an implicit function of m

$$\begin{aligned} 0 \;=\; & A_R[\sinh(\beta_1 m)\cosh(\beta_2(\xi_2-m))+ \\ & \tfrac{D_2\beta_2}{D_1\beta_1}\cosh(\beta_1 m)\sinh(\beta_2(\xi_2-m))]+ \\ & B_R[\sinh(\beta_1 m)\sinh(\beta_2(\xi_2-m))+ \\ & \tfrac{D_2\beta_2}{D_1\beta_1}\cosh(\beta_1 m)\cosh(\beta_2(\xi_2-m))]+ \\ & \sinh(\beta_1 m)\tfrac{p}{\frac{1}{\gamma}+1} \end{aligned}$$

and V_0 as a function of ξ_2 and m

$$\begin{aligned} V_0 \;=\; & A_R[\cosh(\beta_1 m)\cosh(\beta_2(\xi_2-m))+ \\ & \tfrac{D_2\beta_2}{D_1\beta_1}\sinh(\beta_1 m)\sinh(\beta_2(\xi_2-m))]+ \\ & B_R[\cosh(\beta_1 m)\sinh(\beta_2(\xi_2-m))+ \\ & \tfrac{D_2\beta_2}{D_1\beta_1}\sinh(\beta_1 m)\cosh(\beta_2(\xi_2-m))]+ \\ & \cosh(\beta_1 m)\tfrac{p}{\frac{1}{\gamma}+1} \end{aligned}$$

Subcase[II]($\xi_1 < m < \xi_2$) The matching yields ξ_1 and ξ_2 as implicit functions of m

$$\begin{aligned} A_L \;=\; & A_R[\cosh(\rho(m-\xi_1))\cosh(\beta_2(\xi_2-m))+ \\ & \tfrac{D_2\beta_2}{D_1\rho}\sinh(\rho(m-\xi_1))\sinh(\beta_2(\xi_2-m))]+ \\ & B_R[\cosh(\rho(m-\xi_1))\sinh(\beta_2(\xi_2-m))+ \\ & \tfrac{D_2\beta_2}{D_1\rho}\sinh(\rho(m-\xi_1))\cosh(\beta_2(\xi_2-m))]+ \\ & \cosh(\rho(m-\xi_1))[\tfrac{a}{\frac{1}{\gamma}-1}+\tfrac{\bar{p}}{\frac{1}{\gamma}+1}] \end{aligned}$$

$$\begin{aligned} B_L \;=\; & -\{A_R[\sinh(\rho(m-\xi_1))\cosh(\beta_2(\xi_2-m))+ \\ & \tfrac{D_2\beta_2}{D_1\rho}\cosh(\rho(m-\xi_1))\sinh(\beta_2(\xi_2-m))]+ \\ & B_R[\sinh(\rho(m-\xi_1))\sinh(\beta_2(\xi_2-m))+ \\ & \tfrac{D_2\beta_2}{D_1\rho}\cosh(\rho(m-\xi_1))\cosh(\beta_2(\xi_2-m))]+ \\ & \sinh(\rho(m-\xi_1))[\tfrac{a}{\frac{1}{\gamma}-1}+\tfrac{\bar{p}}{\frac{1}{\gamma}+1}]\} \end{aligned}$$

Subcase[III]($\xi_2 < m$) The matching yields V_0 as an implicit function of m

$$\begin{aligned} 0 \;=\; & A_L[\cosh(\rho(m-\xi_1))\sinh(\alpha(1-m))+ \\ & \tfrac{D_1\rho}{D_2\alpha}\sinh(\rho(m-\xi_1))\cosh(\alpha(1-m))]+ \\ & B_L[\sinh(\rho(m-\xi_1))\sinh(\alpha(1-m))+ \\ & \tfrac{D_1\rho}{D_2\alpha}\cosh(\rho(m-\xi_1))\cosh(\alpha(1-m))]- \\ & \sinh(\alpha(1-m))[\tfrac{a}{\frac{1}{\gamma}-1}+\tfrac{\eta}{\frac{1}{\gamma}-\sigma}] \end{aligned}$$

and V_f as a function of ξ_1 and m

$$\begin{aligned} V_f \;=\; & A_L[\cosh(\rho(m-\xi_1))\cosh(\alpha(1-m))+ \\ & \tfrac{D_1\rho}{D_2\alpha}\sinh(\rho(m-\xi_1))\sinh(\alpha(1-m))]+ \\ & B_L[\sinh(\rho(m-\xi_1))\cosh(\alpha(1-m))+ \\ & \tfrac{D_1\rho}{D_2\alpha}\cosh(\rho(m-\xi_1))\sinh(\alpha(1-m))]- \\ & \cosh(\alpha(1-m))[\tfrac{a}{\frac{1}{\gamma}-1}+\tfrac{\eta}{\frac{1}{\gamma}-\sigma}]+\tfrac{\eta}{\frac{1}{\gamma}-\sigma}. \end{aligned}$$

Case[II]$(0 < \xi_2 < 1, V_0 > \frac{a}{2}, V_f > \frac{a}{2} + \frac{p}{k})$

$$V_L(x) = \left(V_0 + \frac{a}{\frac{1}{\gamma} - 1}\right)\cosh(\rho x) - \frac{a}{\frac{1}{\gamma} - 1}$$

$$V_R(x) = \begin{cases} A_R \cosh(\beta_2(\xi_2 - x)) + B_R \sinh(\beta_2(\xi_2 - x)) + \frac{\bar{p}}{\frac{1}{\gamma}+1}, & 0 \le x \le \xi_2 \\ \left(V_f - \frac{\eta}{\frac{1}{\gamma}-\sigma}\right)\cosh(\alpha(1-x)) + \frac{\eta}{\frac{1}{\gamma}-\sigma}, & \xi_2 \le x \le 1 \end{cases}$$

Subcase[I]$(m < \xi_2)$ The matching yields ξ_2 as an implicit function of m

$$\begin{aligned} 0 \;=\; & A_R[\sinh(\rho m)\cosh(\beta_2(\xi_2 - m)) + \\ & \tfrac{D_2\beta_2}{D_1\rho}\cosh(\rho m)\sinh(\beta_2(\xi_2 - m))] + \\ & B_R[\sinh(\rho m)\sinh(\beta_2(\xi_2 - m)) + \\ & \tfrac{D_2\beta_2}{D_1\rho}\cosh(\rho m)\cosh(\beta_2(\xi_2 - m))] + \\ & \sinh(\rho m)[\tfrac{a}{\frac{1}{\gamma}-1} + \tfrac{\bar{p}}{\frac{1}{\gamma}+1}] \end{aligned}$$

and V_0 as a function of ξ_2 and m

$$\begin{aligned} V_0 \;=\; & A_R[\cosh(\rho m)\cosh(\beta_2(\xi_2 - m)) + \\ & \tfrac{D_2\beta_2}{D_1\rho}\sinh(\rho m)\sinh(\beta_2(\xi_2 - m))] + \\ & B_R[\cosh(\rho m)\sinh(\beta_2(\xi_2 - m)) + \\ & \tfrac{D_2\beta_2}{D_1\rho}\sinh(\rho m)\cosh(\beta_2(\xi_2 - m))] + \\ & \cosh(\rho m)[\tfrac{a}{\frac{1}{\gamma}-1} + \tfrac{\bar{p}}{\frac{1}{\gamma}+1}] - \tfrac{a}{\frac{1}{\gamma}-1}. \end{aligned}$$

Subcase[II]$(\xi_2 < m)$ The matching yields V_f and V_0 as functions of m

$$V_f = -\frac{\sinh(\rho m)[\frac{a}{\frac{1}{\gamma}-1} + \frac{\eta}{\frac{1}{\gamma}-\sigma}]}{\sinh(\rho m)\cosh(\alpha(1-m)) + \frac{D_2\alpha}{D_1\rho}\cosh(\rho m)\sinh(\alpha(1-m))} + \frac{\eta}{\frac{1}{\gamma} - \sigma}$$

$$V_0 = \frac{\sinh(\alpha(1-m))[\frac{a}{\frac{1}{\gamma}-1} + \frac{\eta}{\frac{1}{\gamma}-\sigma}]}{\frac{D_1\rho}{D_2\alpha}\sinh(\rho m)\cosh(\alpha(1-m)) + \cosh(\rho m)\sinh(\alpha(1-m))} - \frac{a}{\frac{1}{\gamma} - 1}$$

Case[III]$(0 < \xi_1 < 1, V_0 < \frac{a}{2}, V_f < \frac{a}{2} + \frac{p}{k})$

$$V_L(x) = \begin{cases} V_0 \cosh(\beta_1 x), & 0 \le x \le \xi_1 \\ A_L \cosh(\rho(x-\xi_1)) + B_L \sinh(\rho(x-\xi_1)) - \frac{a}{\frac{1}{\gamma}-1}, & \xi_1 \le x \le 1 \end{cases}$$

$$V_R(x) = \left(V_f - \frac{p}{\frac{1}{\gamma}+1} \right) \cosh(\beta_2(1-x)) + \frac{p}{\frac{1}{\gamma}+1}$$

Subcase[I]$(m < \xi_1)$ The matching yields V_f and V_0 as functions of m

$$V_f = -\frac{\sinh(\beta_1 m)\frac{p}{\frac{1}{\gamma}+1}}{\sinh(\beta_1 m)\cosh(\beta_2(1-m)) + \frac{D_2\beta_2}{D_1\beta_1}\cosh(\beta_1 m)\sinh(\beta_2(1-m))} + \frac{p}{\frac{1}{\gamma}+1}$$

$$V_0 = \frac{\sinh(\beta_2(1-m))\frac{p}{\frac{1}{\gamma}+1}}{\frac{D_1\beta_1}{D_2\beta_2}\sinh(\beta_1 m)\cosh(\beta_2(1-m)) + \cosh(\beta_1 m)\sinh(\beta_2(1-m))}$$

Subcase[II]$(\xi_1 < m)$ The matching yields ξ_1 as an implicit function of m

$$\begin{aligned} 0 = \; & A_L[\sinh(\beta_2(1-m))\cosh(\rho(m-\xi_1)) + \\ & \tfrac{D_1\rho}{D_2\beta_2}\cosh(\beta_2(1-m))\sinh(\rho(m-\xi_1))] + \\ & B_L[\sinh(\beta_2(1-m))\sinh(\rho(m-\xi_1)) + \\ & \tfrac{D_1\rho}{D_2\beta_2}\cosh(\beta_2(1-m))\cosh(\rho(m-\xi_1))] - \\ & \sinh(\beta_2(1-m))[\tfrac{a}{\frac{1}{\gamma}-1} + \tfrac{\bar{p}}{\frac{1}{\gamma}+1}] \end{aligned}$$

and V_f as a function of ξ_1 and m

$$\begin{aligned} V_f = \; & A_L[\cosh(\beta_2(1-m))\cosh(\rho(m-\xi_1)) + \\ & \tfrac{D_1\rho}{D_2\beta_2}\sinh(\beta_2(1-m))\sinh(\rho(m-\xi_1))] + \\ & B_L[\cosh(\beta_2(1-m))\sinh(\rho(m-\xi_1)) + \\ & \tfrac{D_1\rho}{D_2\beta_2}\sinh(\beta_2(1-m))\cosh(\rho(m-\xi_1))] - \\ & \cosh(\beta_2(1-m))[\tfrac{a}{\frac{1}{\gamma}-1} + \tfrac{\bar{p}}{\frac{1}{\gamma}+1}] + \tfrac{\bar{p}}{\frac{1}{\gamma}+1}. \end{aligned}$$

Case[IV]($0 < 1$ - no ξ_1 or ξ_2 interior)

$$V_L(x) = \left(V_0 + \frac{a}{\frac{1}{\gamma} - 1} \right) \cosh(\rho x) - \frac{a}{\frac{1}{\gamma} - 1}$$

$$V_R(x) = \left(V_f - \frac{\bar{p}}{\frac{1}{\gamma} + 1} \right) \cosh(\beta_2(1-x)) + \frac{\bar{p}}{\frac{1}{\gamma} + 1}$$

The matching yields V_f and V_0 as functions of m

$$V_0 = \frac{\sinh(\beta_2(1-m))[\frac{a}{\frac{1}{\gamma}-1} + \frac{\bar{p}}{\frac{1}{\gamma}+1}]}{\sinh(\beta_2(1-m))\cosh(\rho m) + \frac{D_1\rho}{D_2\beta_2}\cosh(\beta_2(1-m))\sinh(\rho m)} - \frac{a}{\frac{1}{\gamma} - 1}$$

$$V_f = -\frac{\sinh(\rho m)[\frac{a}{\frac{1}{\gamma}-1} + \frac{\bar{p}}{\frac{1}{\gamma}+1}]}{\frac{D_2\beta_2}{D_1\rho}\sinh(\beta_2(1-m))\cosh(\rho m) + \cosh(\beta_2(1-m))\sinh(\rho m)} + \frac{p}{\frac{1}{\gamma} + 1}$$

APPENDIX D

MM PDE EIGENFUNCTIONS AND EIGENVALUES

The potential function for each of the 8 cases and subcases described in the steady state derivations (Appendix C) is described as

$C1S1 \quad \psi(x) = \begin{cases} -1 & 0 < x < m \\ -1 & m < x < \xi_2 \\ \sigma & \xi_2 < x < 1 \end{cases}$	$C1S2 \quad \psi(x) = \begin{cases} -1 & 0 < x < \xi_1 \\ 1 & \xi_1 < x < m \\ -1 & m < x < \xi_2 \\ \sigma & \xi_2 < x < 1 \end{cases}$
$C1S3 \quad \psi(x) = \begin{cases} -1 & 0 < x < \xi_1 \\ 1 & \xi_1 < x < m \\ \sigma & m < x < 1 \end{cases}$	$C2S1 \quad \psi(x) = \begin{cases} 1 & 0 < x < m \\ -1 & m < x < \xi_2 \\ \sigma & \xi_2 < x < 1 \end{cases}$
$C2S2 \quad \psi(x) = \begin{cases} 1 & 0 < x < m \\ \sigma & m < x < 1 \end{cases}$	$C3S1 \quad \psi(x) = \begin{cases} -1 & 0 < x < m \\ -1 & m < x < 1 \end{cases}$
$C3S2 \quad \psi(x) = \begin{cases} -1 & 0 < x < \xi_1 \\ 1 & \xi_1 < x < m \\ -1 & m < x < 1 \end{cases}$	$C4 \quad \psi(x) = \begin{cases} 1 & 0 < x < m \\ -1 & m < x < 1 \end{cases}$

From Lemma (1) it is clear that any steady state solution that falls into the C3S1 category is stable. It is also clear from Lemma (2) and the above table that $-1 < \mu$. So the main question is whether or not in each case there exists a μ such that $-1 < \mu < -\epsilon\gamma$.

As an example consider the C1S2 category. We determine a characteristic function which is solved numerically but which may be considered numerically or

graphically.

If $\underline{-1 < \mu < -\sigma}$, then the eigenfunctions associated with such eigenvalues taking into account the boundary conditions and letting

$$\alpha_{ipm} = \sqrt{\frac{1-\mu}{D_i}}, \alpha_{pp} = \sqrt{\frac{1+\mu}{D_1}}, \alpha_{\sigma m} = \sqrt{\frac{-\sigma-\mu}{D_2}} \alpha_{\sigma p} = \sqrt{\frac{\sigma+\mu}{D_2}}$$

is of the form

$$v(x) = \begin{cases} A_1 \cosh(\alpha_{1pm} x) & 0 < x < \xi_1 \\ A_2 \cos(\alpha_{pp}(x-\xi_1)) + B_2 \sin(\alpha_{pp}(x-\xi_1)) & \xi_1 < x < m \\ A_3 \cosh(\alpha_{2pm}(\xi_2 - x)) + B_3 \sinh(\alpha_{2pm}(\xi_2 - x)) & m < x < \xi_2 \\ A_4 \cosh(\alpha_{\sigma m}(1-x)) & \xi_2 < x < 1 \end{cases}$$

A_2 and B_2, and A_3 and B_3 are found in terms of A_1 and A_4, respectively, from matching across $x = \xi_1$ and $x = \xi_2$ again respectively. From continuously matching v and the flux, Dv_x, at $x = m$, we get two equations which are linear in A_1 and A_4 and are written as

$$\begin{bmatrix} M_{11} & M_{12} \\ D_1 M_{21} & D_2 M_{22} \end{bmatrix} \begin{bmatrix} A_1 \\ A_4 \end{bmatrix} = \begin{bmatrix} 0 \\ 0 \end{bmatrix}$$

where

$$\begin{aligned} M_{11} = & \ \tfrac{\alpha_{1pm}}{\alpha_{pp}} \sinh(\alpha_{1pm}\xi_1) \sin(\alpha_{pp}(m-\xi_1)) \\ & + \cosh(\alpha_{1pm}\xi_1) \cos(\alpha_{pp}(m-\xi_1)) \\ M_{12} = & \ -\tfrac{\alpha_{\sigma m}}{\alpha_{2pm}} \sinh(\alpha_{\sigma m}(1-\xi_2)) \sinh(\alpha_{2pm}(\xi_2 - m)) \\ & - \cosh(\alpha_{\sigma m}(1-\xi_2)) \cosh(\alpha_{2pm}(\xi_2 - m)) \\ M_{21} = & \ \alpha_{1pm} \sinh(\alpha_{1pm}\xi_1) \cos(\alpha_{pp}(m-\xi_1)) \\ & - \alpha_{pp} \cosh(\alpha_{1pm}\xi_1) \sin(\alpha_{pp}(m-\xi_1)) \\ M_{22} = & \ \alpha_{\sigma m} \sinh(\alpha_{\sigma m}(1-\xi_2)) \cosh(\alpha_{2pm}(\xi_2 - m)) \\ & + \alpha_{2pm} \cosh(\alpha_{\sigma m}(1-\xi_2)) \sinh(\alpha_{2pm}(\xi_2 - m)) \end{aligned}$$

Solving the characteristic equation $F(\mu) = D_1 M_{11} M_{22} - D_2 M_{21} M_{12} = 0$ for μ yields the eigenvalues of the Sturm-Liouville problem in the domain $\underline{-1 < \mu < -\sigma}$.

Now if $\underline{-\sigma < \mu < -\epsilon\gamma}$, the associated eigenfunctions are

$$v(x) = \begin{cases} A_1 \cosh(\alpha_{1pm} x) & 0 < x < \xi_1 \\ A_2 \cos(\alpha_{pp}(x-\xi_1)) + B_2 \sin(\alpha_{pp}(x-\xi_1)) & \xi_1 < x < m \\ A_3 \cosh(\alpha_{2pm}(\xi_2 - x)) + B_3 \sinh(\alpha_{2pm}(\xi_2 - x)) & m < x < \xi_2 \\ A_4 \cos(\alpha_{\sigma p} x) & \xi_2 < x < 1 \end{cases}.$$

The elements of the characteristic equation are

$$
\begin{aligned}
M_{11} = &\ \tfrac{\alpha_{1pm}}{\alpha_{pp}} \sinh(\alpha_{1pm}\xi_1)\sin(\alpha_{pp}(m-\xi_1)) \\
&+ \cosh(\alpha_{1pm}\xi_1)\cos(\alpha_{pp}(m-\xi_1)) \\
M_{12} = &\ \tfrac{\alpha_{\sigma p}}{\alpha_{2pm}} \sin(\alpha_{\sigma p}(1-\xi_2))\sinh(\alpha_{2pm}(\xi_2-m)) \\
&- \cos(\alpha_{\sigma p}(1-\xi_2))\cosh(\alpha_{2pm}(\xi_2-m)) \\
M_{21} = &\ -\alpha_{pp}\cosh(\alpha_{1pm}\xi_1)\sin(\alpha_{pp}(m-\xi_1)) \\
&+\alpha_{1pm}\sinh(\alpha_{1pm}\xi_1)\cos(\alpha_{pp}(m-\xi_1)) \\
M_{22} = &\ \alpha_{2pm}\cos(\alpha_{\sigma p}(1-\xi_2))\sinh(\alpha_{2pm}(\xi_2-m)) \\
&-\alpha_{\sigma p}\sin(\alpha_{\sigma p}(1-\xi_2))\cosh(\alpha_{2pm}(\xi_2-m))
\end{aligned}
$$

C3S2

$\underline{-1 < \mu < -\epsilon\gamma}$

$$
v(x) = \begin{cases} A_1\cosh(\alpha_{1pm}x) & 0 < x < \xi_1 \\ A_2\cos(\alpha_{pp}(x-\xi_1)) + B_2\sin(\alpha_{pp}(x-\xi_1)) & \xi_1 < x < m \\ A_3\cosh(\alpha_{2pm}(1-x)) & m < x < 1 \end{cases} .
$$

$$
\begin{aligned}
M_{11} = &\ \tfrac{\alpha_{1pm}}{\alpha_{pp}} \sinh(\alpha_{1pm}\xi_1)\sin(\alpha_{pp}(m-\xi_1)) \\
&+ \cosh(\alpha_{1pm}\xi_1)\cos(\alpha_{pp}(m-\xi_1)) \\
M_{12} = &\ -\cosh(\alpha_{2pm}(1-m)) \\
M_{21} = &\ \alpha_{1pm}\sinh(\alpha_{1pm}\xi_1)\cos(\alpha_{pp}(m-\xi_1)) \\
&-\alpha_{pp}\cosh(\alpha_{1pm}\xi_1)\sin(\alpha_{pp}(m-\xi_1)) \\
M_{22} = &\ \alpha_{2pm}\sinh(\alpha_{2pm}(1-m))
\end{aligned}
$$

C4

$\underline{-1 < \mu < -\epsilon\gamma}$

$$
v(x) = \begin{cases} A_1\cos(\alpha_{pp}x) & 0 < x < m \\ A_2\cosh(\alpha_{2pm}(1-x)) & m < x < 1 \end{cases} .
$$

$$
\begin{aligned}
M_{11} = &\ \cos(\alpha_{pp}m) \\
M_{12} = &\ -\cosh(\alpha_{2pm}(1-m)) \\
M_{21} = &\ \alpha_{pp}\sin(\alpha_{pp}m) \\
M_{22} = &\ -\alpha_{2pm}\sinh(\alpha_{2pm}(1-m))
\end{aligned}
$$

C2S2

$\underline{-1 < \mu < -\sigma}$

$$v(x) = \begin{cases} A_1 \cos(\alpha_{pp} x) & 0 < x < m \\ A_2 \cosh(\alpha_{\sigma m}(1-x)) & m < x < 1 \end{cases} .$$

$$\begin{aligned} M_{11} &= \cos(\alpha_{pp} m) \\ M_{12} &= -\cosh(\alpha_{\sigma m}(1-m)) \\ M_{21} &= \alpha_{pp} \sin(\alpha_{pp} m) \\ M_{22} &= -\alpha_{\sigma m} \sinh(\alpha_{\sigma m}(1-m)) \end{aligned}$$

$\underline{-\sigma < \mu < -\epsilon\gamma}$

$$v(x) = \begin{cases} A_1 \cos(\alpha_{pp} x) & 0 < x < m \\ A_2 \cos(\alpha_{\sigma p}(1-x)) & m < x < 1 \end{cases} .$$

$$\begin{aligned} M_{11} &= \cos(\alpha_{pp} m) \\ M_{12} &= -\cos(\alpha_{\sigma p}(1-m)) \\ M_{21} &= \alpha_{pp} \sin(\alpha_{pp} m) \\ M_{22} &= \alpha_{\sigma m} \sin(\alpha_{\sigma m}(1-m)) \end{aligned}$$

C2S1

$\underline{-1 < \mu < -\sigma}$

$$v(x) = \begin{cases} A_1 \cos(\alpha_{pp} x) & 0 < x < m \\ A_2 \cosh(\alpha_{2pm}(\xi_2 - x)) + B_2 \sinh(\alpha_{2pm}(\xi_2 - x)) & m < x < \xi_2 \\ A_3 \cosh(\alpha_{\sigma m}(1-x)) & \xi_2 < x < 1 \end{cases} .$$

$$\begin{aligned} M_{11} &= -\cos(\alpha_{pp} m) \\ M_{12} &= \tfrac{\alpha_{\sigma m}}{\alpha_{2pm}} \sinh(\alpha_{\sigma m}(1-\xi_2)) \sinh(\alpha_{2pm}(\xi_2 - m)) \\ &\quad + \cosh(\alpha_{\sigma m}(1-\xi_2)) \cosh(\alpha_{2pm}(\xi_2 - m)) \\ M_{21} &= -\alpha_{pp} \sin(\alpha_{pp} m) \\ M_{22} &= \alpha_{2pm} \cosh(\alpha_{\sigma m}(1-\xi_2)) \sinh(\alpha_{2pm}(\xi_2 - m)) \\ &\quad + \alpha_{\sigma m} \sinh(\alpha_{\sigma m}(1-\xi_2)) \cosh(\alpha_{2pm}(\xi_2 - m)) \end{aligned}$$

$\underline{-\sigma < \mu < -\epsilon\gamma}$

$$v(x) = \begin{cases} A_1 \cos(\alpha_{pp} x) & 0 < x < m \\ A_2 \cosh(\alpha_{2pm}(\xi_2 - x)) + B_2 \sinh(\alpha_{2pm}(\xi_2 - x)) & m < x < \xi_2 \\ A_3 \cos(\alpha_{\sigma p}(1-x)) & \xi_2 < x < 1 \end{cases} .$$

$$\begin{aligned} M_{11} &= -\cos(\alpha_{pp} m) \\ M_{12} &= -\tfrac{\alpha_{\sigma p}}{\alpha_{2pm}} \sin(\alpha_{\sigma p}(1-\xi_2) \sinh(\alpha_{2pm}(\xi_2 - m)) \\ &\quad + \cos(\alpha_{\sigma p}(1-\xi_2) \cosh(\alpha_{2pm}(\xi_2 - m)) \\ M_{21} &= -\alpha_{pp} \sin(\alpha_{pp} m) \\ M_{22} &= \alpha_{2pm} \cos(\alpha_{\sigma p}(1-\xi_2) \sinh(\alpha_{2pm}(\xi_2 - m)) \\ &\quad - \alpha_{\sigma p} \sin(\alpha_{\sigma p}(1-\xi_2) \cosh(\alpha_{2pm}(\xi_2 - m)) \end{aligned}$$

C1S1

$\underline{-1 < \mu < -\sigma}$

$$v(x) = \begin{cases} A_1 \cosh(\alpha_{1pm} x) & 0 < x < m \\ A_2 \cosh(\alpha_{2pm}(\xi_2 - x)) + B_2 \sinh(\alpha_{2pm}(\xi_2 - x)) & m < x < \xi_2 \\ A_3 \cosh(\alpha_{\sigma m}(1-x)) & \xi_2 < x < 1 \end{cases} .$$

$$\begin{aligned} M_{11} = & \cosh(\alpha_{1pm} m) \\ M_{12} = & -\tfrac{\alpha_{\sigma m}}{\alpha_{2pm}} \sinh(\alpha_{\sigma m}(1-\xi_2)) \sinh(\alpha_{2pm}(\xi_2 - m)) \\ & - \cosh(\alpha_{\sigma m}(1-\xi_2)) \cosh(\alpha_{2pm}(\xi_2 - m)) \\ M_{21} = & \alpha_{1pm} \sinh(\alpha_{1pm} m) \\ M_{22} = & \tfrac{\alpha_{\sigma m}}{\alpha_{2pm}} \sinh(\alpha_{\sigma m}(1-\xi_2)) \cosh(\alpha_{2pm}(\xi_2 - m)) \\ & + \cosh(\alpha_{\sigma m}(1-\xi_2)) \sinh(\alpha_{2pm}(\xi_2 - m)) \end{aligned}$$

Notice that the characteristic function is the sum of hyperbolic functions with positive coefficients and so is never zero.

$\underline{-\sigma < \mu < -\epsilon\gamma}$

$$v(x) = \begin{cases} A_1 \cosh(\alpha_{1pm} x) & 0 < x < m \\ A_1 \cosh(\alpha_{2pm} x) & m < x < \xi_2 \\ A_2 \cos(\alpha_{\sigma p}(1-x)) & \xi_2 < x < 1 \end{cases} .$$

$$\begin{aligned} M_{11} = & \cosh(\alpha_{1pm} m) \\ M_{12} = & \tfrac{\alpha_{\sigma p}}{\alpha_{2pm}} \sin(\alpha_{\sigma p}(1-\xi_2)) \sinh(\alpha_{2pm}(\xi_2 - m)) \\ & - \cos(\alpha_{\sigma p}(1-\xi_2)) \cosh(\alpha_{2pm}(\xi_2 - m)) \\ M_{21} = & \alpha_{1pm} \sinh(\alpha_{1pm} m) \\ M_{22} = & \alpha_{2pm} \cos(\alpha_{\sigma p}(1-\xi_2)) \sinh(\alpha_{2pm}(\xi_2 - m)) \\ & -\alpha_{\sigma p} \sin(\alpha_{\sigma p}(1-\xi_2)) \cosh(\alpha_{2pm}(\xi_2 - m)) \end{aligned}$$

C1S3

$\underline{-1 < \mu < -\sigma}$

$$v(x) = \begin{cases} A_1 \cosh(\alpha_{1pm} x) & 0 < x < \xi_1 \\ A_2 \cos(\alpha_{pp}(x - \xi_1)) + B_2 \sin(\alpha_{pp}(x - \xi_1)) & \xi_1 < x < m \\ A_3 \cosh(\alpha_{\sigma m}(1-x)) & m < x < 1 \end{cases} .$$

$$\begin{aligned} M_{11} = & \tfrac{\alpha_{1pm}}{\alpha_{pp}} \sinh(\alpha_{1pm} \xi_1) \sin(\alpha_{pp}(m - \xi_1)) \\ & + \cosh(\alpha_{1pm} \xi_1) \cos(\alpha_{pp}(m - \xi_1)) \\ M_{12} = & -\cosh(\alpha_{\sigma m}(1-m)) \\ M_{21} = & -\alpha_{pp} \cosh(\alpha_{1pm} \xi_1) \sin(\alpha_{pp}(m - \xi_1)) \\ & +\alpha_{1pm} \sinh(\alpha_{1pm} \xi_1) \cos(\alpha_{pp}(m - \xi_1)) \\ M_{22} = & -\alpha_{\sigma m} \sinh(\alpha_{\sigma m}(1-m)) \end{aligned}$$

$\underline{-\sigma < \mu < -\epsilon\gamma}$

$$v(x) = \begin{cases} A_1 \cosh(\alpha_{1pm} x) & 0 < x < \xi_1 \\ A_2 \cos(\alpha_{pp}(x - \xi_1)) + B_2 \sin(\alpha_{pp}(x - \xi_1)) & \xi_1 < x < m \\ A_3 \cos(\alpha_{\sigma p}(1 - x)) & m < x < 1 \end{cases} .$$

$$\begin{aligned} M_{11} = \; & \tfrac{\alpha_{1pm}}{\alpha_{pp}} \sinh(\alpha_{1pm}\xi_1) \sin(\alpha_{pp}(m - \xi_1)) \\ & + \cosh(\alpha_{1pm}\xi_1) \cos(\alpha_{pp}(m - \xi_1)) \\ M_{12} = \; & - \cos(\alpha_{\sigma p}(1 - m)) \\ M_{21} = \; & \alpha_{pp} \cosh(\alpha_{1pm}\xi_1) \sin(\alpha_{pp}(m - \xi_1)) \\ & + \alpha_{1pm} \sinh(\alpha_{1pm}\xi_1) \cos(\alpha_{pp}(m - \xi_1)) \\ M_{22} = \; & - \alpha_{\sigma p} \sin(\alpha_{\sigma p}(1 - m)) \end{aligned}$$

REFERENCES

[1] M. Beardslee, D. Lerner, P. Tadros, J. Laing, E. Beyer, K. Yamada, A. Kléber, R. Schuessler, and J. Saffitz, *Dephosphorylation and intracellular redistribution of ventricular connexion43 during electrical uncoupling induced by ischemia*, Circulation Research, 87 (2000), pp. 656–662.

[2] E. Carmeliet, *Cardiac ionic currents and acute ischemia: From channels to arrhythmias*, Physiological Reviews, 79 (1999), pp. 917–1017.

[3] W. Cascio, T. Johnson, and L. Gettes, *Electrophysiologic cahnges in ischemic ventricular myocardium: I. influence of ionic, metabolic, and energetic changes*, J. Cardiovasc. Electrophysiol., 6 (1995), pp. 1039–1062.

[4] F. Ch'en, R. Vaughan-Jones, K. Clarke, and D. Noble, *Modelling myocardial ischemia and reperfusion*, Progress in Biophysics and Molecular Biology, 69 (1998), pp. 515–538.

[5] P. Daleau, *Lysophosphatidylcholine, a metabolite which accumulates early in myocardium during ischemia, reduces gap junctional coupling in cardiac cells*, J. Mol. Cell Cardiol., 31 (1999), pp. 1391–1401.

[6] E. Doedel, A. Champneys, T. Fairgrieve, Y. Kuznetsov, B. Sandstede, and X. Wang, *AUTO97: Continuation and Bifurcation Software for Ordinary Differential Equations*, 1998.

[7] L. Evans, *Partial Differential Equations*, vol. 19 of Graduate Studies in Mathematics, American Mathematical Society, 1998.

[8] R. FitzHugh, *Thresholds and plateaus in the hodgkin-huxley nerve equations*, J. Gen. Physiol., 43 (1960), p. 867. @.

[9] ——, *Impulses and physiological states in theoretical models of nerve membrane*, Biophysical Journal, 1 (1961), pp. 445–466.

[10] A. Harris and A. Rojas, *The initiation of vantricular fibrillation due to coronary occlusion*, Exp. Med. Surg., 1 (1943), pp. 105–122.

[11] A. Hodgkin and A. Huxley, *A quantitative description of membrane current and its application to conduction and excitation in nerve*, J. Physiol., 117 (1952), pp. 500–544.

[12] M. Janse and A. Wit, *Electrophysiological mechanisms of ventricular arrhythmias resulting from myocardial ischemia and infarction*, Physiological Reviews, 69 (1989), pp. 1049–1169.

[13] B. Katzung, L. Hondeghem, and A. Grant, *Cardiac ventricular automaticity induced by current of injury*, Pfluger's Arch, 360 (1975), pp. 193–197.

[14] J. Keener, *Principles of Applied Mathematics: Transformation and Approximation*, Addison-Wesley, 1st ed., 1988.

[15] J. Keener and J. Sneyd, *Mathematical Physiology*, Interdisciplinary Applied Mathematics, Springer, 1998.

[16] R. Kumar and R. Joyner, *An experimental model of the production of early after depolarizations by injury current from an ischemic region*, Pflugers Arch, 428 (1994), pp. 425–432.

[17] R. Kumar, R. Wilders, R. Joyner, H. Jongsma, E. Verheijck, D. Golod, A. van Ginneken, and W. Goolsby, *Experimental model for an ectopic focus coupled to ventricular cells*, Circulation, 94 (1996), pp. 833–841.

[18] J. Kupersmith, Z.-Y. Li, and C. Maldonado, *Marked action potential porlongation as a source of injury current leading to border zone arrhythmogenesis*, Am Heart J, 127 (1994), pp. 1543–53.

[19] T. Lewis, *The Effects of Nonexcitable Regions on Signal Propagation in Excitable Media: Propagation Failure and Reflection*, PhD thesis, University of Utah, 1998.

[20] C.-H. Luo and Y. Rudy, *A model of the ventricular cardiac action potential; depolarization repolarization and their interaction*, Circ. Res., 68 (1991), pp. 1501–1526.

[21] H. McKean, Jr., *Nagumo's equation*, Advances in Mathematics, (1970), pp. 209–223.

[22] R. McOwen, *Partial Differential Equations: Methods and Applications*, Prentice-Hall, 1996.

[23] P. Morse and H. Feshbach, *Methods of Theoretical Physics*, McGraw Hill, 1999.

[24] B. Muller-Borer, T. Johnson, L. Gettes, and W. Cascio, *Failure of impulse propagation in a mathematically simulated ischemic border zone: Influence of direction of propagation and cell-to-cell electrical coupling*, J. Cardiovasc. Electrophysiol., 6 (1995), pp. 1101–1112.

[25] N. Peters, C. Green, P. Poole-Wilson, and N. Severs, *Reduced content of connexin43 gap junctions in ventricular myocardium from hypertrophied and ischemic human hearts*, Circulation, 88 (1993), pp. 864–875.

[26] S. Picard, R. Rouet, P. Ducouret, P. Puddu, F. Flais, A. Criniti, F. Monti, and J.-L. Gérard, *K_{atp} channels and 'border zone' arrhythmias: Role of the repolarization dispersion between normal and ischaemic ventricular regions*, British Journal of Pharmacology, 127 (1999), pp. 1687–1695.

[27] J. Rinzel, *Repetitive activity and hopf bifurcation under point-stimulation for a simple fitzhugh-nagumo nerve conduction model*, J. Math. Biology, 5 (1978), pp. 363–382.

[28] J. Rinzel and J. Keener, *Hopf bifurcation to repetitive activity in nerve*, SIAM J. Appl. Math., 43 (1983), pp. 907–922.

[29] R. Rouet, M. Adamantidis, E. Honore, and B. Dupuis, *In vitro abnormal repetitive responses in guinea pig ventricular myocardium exposed to combined hypoxia, hyperkalemia and acidosis*, J. of Appl. Cardiol, 4 (1989), pp. 19–29.

[30] R. Rouet, S. Picard, C. Libersa, M. Ghadanfar, C. Alabaster, and J.-L. Gérard, *Electrophysiological effects of dofetilide in an in vitro model of "border zone" between normal and ischemic/reperfused myocardium*, Circulation, 101 (2000), pp. 86–93.

[31] R. Tan and R. Joyner, *Electrotonic influences on action potentials from isolated ventricular cells*, Circ. Res., 67 (1990), pp. 1071–1081.

[32] R. Tan, T. Osaka, and R. Joyner, *Experimental model of effects on normal tissue of injury current from ischemic region*, Circ. Res., 69 (1991), pp. 965–974.

[33] G. Tolstov, *Fourier Series*, Dover Publications Inc., 1962.

[34] M. Wagner, D. Golod, R. Wilders, E. Verheijck, R. Joyner, R. Kumar, H. Jongsma, A. van Ginneken, and W. N. Goolsby, *Modulation of propagation from an ectopic focus by electrical load and by extracellular potassium*, Am. J. Physiology, 272 (1997), pp. H1759–H1769.

[35] K. Yamada, J. McHowat, G.-X. Yan, K. Donahue, J. Peirick, A. Kléber, and P. Corr, *Cellular uncoupling induced by accumulation of lon-chain acylcarnitine during ischemia*, Circ. Res., 74 (1994), pp. 83–95.